LIGHT-CHARGED-PARTICLE EMISSION IN keV NEUTRON INDUCED FISSION OF ^{235}U

A Thesis Submitted
in Partial Fulfilment of the Requirements
for the Degree of

DOCTOR OF PHILOSOPHY

By

SHIV CHARAN LAL SHARMA

to the

DEPARTMENT OF PHYSICS

INDIAN INSTITUTE OF TECHNOLOGY KANPUR
OCTOBER, 1980

PHY-1980-D-SMA-LIG

CERTIFICATE

Certified that the work presented in this thesis entitled "Light-Charged-Particle Emission in keV Neutron Induced Fission of ^{235}U" by Mr. Shiv Charan Lal Sharma, has been done under my supervision and that it has not been submitted elsewhere for a degree.

G. K. Mehta
Professor
Department of Physics
Indian Institute of Technology Kanpur

October 1980.

ACKNOWLEDGEMENTS

Shiv Charan Lal Sharma

CONTENTS

LIST OF TABLES

LIST OF FIGURES

Figure   Caption   Page

TO

MY PARENTS

AND

SHOBHANA

40°, 50°, 62° and $70\ ^{\circ}C$. The temperature dependence of bulk-etch rate is used to obtain the activation energy of bulk-etching which helps in determining the bulk-etch rate at any temperature. The detector is found to have isotropic bulk-etching and therefore suitable for rear-etching technique. The rear-etching technique is described and used to check the technique by determining alpha particle energy spectrum from ^{227}Ac and long-range alpha-particle energy spectrum from spontaneous fission of ^{252}Cf.

The yield and energy distributions of long-range alpha-particles (LRA) emitted in the keV neutron induced fission of ^{235}U are studied using rear-etching technique. The LRA yields from neutron induced fission of ^{235}U at neutron energies: thermal, 125 ± 12, 155 ± 11, 185 ± 10, 210 ± 9, 240 ± 9, 365 ± 40 and 480 ± 40 keV are, thus, determined. In these measurements also, the yield showed a structure around $E_n = 200$ keV with higher yield in the neutron energy region from 120 keV to 250 keV. It is found that in this region the yield is about 50 % higher than that of thermal neutrons. At neutron energies above $E_n = 250$ keV, the LRA yield slowly decreases towards the value for thermal neutrons. These results are presented and discussed in the Chapter IV.

The fifth and the final chapter of the thesis contains the summary of all the results along with the conclusions.

CHAPTER I

INTRODUCTION

1.1 Fission Process

The breaking-up of a heavy nucleus into two or more parts is known as fission. These parts are called fission fragments. The phenomenon was discovered by Hahn and Strassman in 1939 [1]. Meitner and Frisch [2], in the same year, calculated the large energy release ($\sim$200 MeV) as the outcome of this process which was experimentally confirmed by Frisch [3] who observed very large pulses produced by the fission fragments in the ionization chamber. Spontaneous and induced fissions are the two categories of fission. The particle or photon induced fission is a complex nuclear reaction via compound nucleus formation. The compound nucleus formed in induced fission, is in an excited state with the excitation energy distributed among a large number of degrees

of freedom such as the collective nuclear rotations, vibrations and the single particle excitations. The dissipation of the available energy can take place through particle emission, γ-emission or fission. The fission occurs only if a sufficient amount of excitation energy becomes concentrated in the potential energy of deformation which enables the nucleus to pass through the saddle point. The saddle point corresponds to the shape at which the potential energy of deformation is maximum.* From saddle point to scission point the repulsive Coulomb forces dominate over the attractive nuclear forces (analogous to the attractive surface tension force in the liquid drops) and at the scission point the nucleus splits into two or more parts. At the scission point nuclear interaction ceases to play part among the nascent fragments.

Being a complex nuclear reaction via compound nucleus formation, fission process can be considered in three phases. Prior to the saddle point the nucleus undergoes several oscillations until one of them brings it to the scission through the saddle point where nucleus breaks up into two or more parts. The estimated time, nucleus takes, from saddle point to scission point is about 10^{-21} Sec. The motion from saddle to scission is very complex and it has not yet been fully understood. The motion of the fission fragments after scission point is solely governed by Coulomb forces.

* Lowest maximum for multidimensional deformation.

Most often, the nucleus splits into two unequal parts termed as binary fission. In about every 500 binary fissions, the normal fission fragments are accompanied by a light-charged-particle. This mode of fission is known as the light-charged-particle accompanied fission (in short LCP accompanied fission). When a nucleus breaks up into three heavy fragments, it is called ternary fission [4]. Ternary fission is less probable than LCP accompanied fission. A fourth very rarely occuring mode of fission is that in which two heavy fission fragments are accompanied by two light-charged-particles (mostly these particles are alpha particles) [5,6]. The last mode of fission is known as the quaternary fission.

The most studied mode of fission is binary fission. The important aspects of binary fission studies are the fission fragment mass distribution, charge distribution, kinetic energy distribution, prompt neutron emission and prompt gamma ray emission. At lower excitation energies, the mass distribution for actinide nuclei ($A > 229$) is asymmetric having heavy fragments peak at mass number around 140 for all these fissioning nuclei [7]. The light fragments peak shifts with the compound nucleus mass number. At higher excitation energies, the mass division becomes more symmetric, which can be understood in terms of the " washing out" of the shell effects at higher excitation energies. The fissioning nucleus at high excitation energy sees only a liquid drop

type of barrier which predicts symmetric mass division as the most probable mode of fission.

The charge distribution is another important characteristic of binary fission. Recent measurements [8] have shown that the charge-to-mass ratio for the light fragment is more than that for the heavy fragments. This indicates that the lighter fragment receives larger fraction of the available charge.

The largest fraction of the released energy in the fission process goes into the kinetic energy of the fragments resulting mainly due to the Coulomb repulsion between the nascent fission fragments. The total kinetic energy of the fragments increases slowly with Z^2/A. The excitation energy dependence of the total kinetic energy has been studied extensively [9] and it has been established that the dependence of total kinetic energy on the compound nucleus excitation energy is very weak which suggests that a large fraction of the excitation energy goes into the fragments excitation and not into kinetic energy. This indicates that the extent of stretching of the neck (the Coulomb potential energy at scission) remains more or less the same as the compound nucleus excitation energy increases.

The dissipation of the excitation energy of the fragments takes place by prompt neutron emission and prompt gamma emission. The principal sources, which contribute to

the fragment excitation energy, are the intrinsic excitation energy, the deformation energy of the fragments at the scission and the Coulomb excitation of one fragment due to the other during separation.   Since most of the excitation energy of the fragments gets dissipated by prompt neutron emission, the prompt neutron studies provide information about the deformation and excitation energies of the fragments at the scission. One of the quantities of interest is the average number of neutrons per fission which increases with the mass number and excitation energy of the compound nucleus [10].   For low-energy fission of actinide nuclei, the neutron yield versus fission fragment mass show a saw-tooth behaviour which vanishes at higher excitation energies.   The majority of prompt neutrons are emitted from the fully accelerated fission fragments (emitted in time $\leq 4 \times 10^{-14}$ Sec. after scission) [7].   About 10 % of the neutrons are emitted at the scission point [11,12].

A considerable amount of the fragment excitation energy is dissipated by means of prompt gamma ray emission.   About 8 MeV energy per fission event [13] goes into the prompt gamma ray emission through about 8-10 photons per fission event.

The forward peaked angular distribution of prompt gamma rays relative to fragment direction could be understood in terms of the fragment angular momentum.   These gammas differ from gamma rays associated with the neutron capture in the sense that they carry away large angular momentum

($\sim 10\,\hbar$ to $12\,\hbar$) from the fragments and hence they contribute
a lot in understanding the deexcitation mechanism of the
fission fragments.

Lastly, the study of the fission fragment angular
distribution is important to understand the mechanism by
which a fraction of the projectile angular momentum gets
converted into the orbital angular momentum between the
fission fragments.

1.2 Bohr's Unified Model of Fission

The explanation of the nuclear fission was first
given by Bohr and Wheeler in 1939 [14]. They calculated
fission barriers, i.e. the potential energy variation with
the deformation of the nucleus, using liquid drop model of
nucleus. According to this model, only Coulomb energy and
surface energy of nucleus change under deformation and
therefore the nucleus remains stable against small distortions
if the decrease in the Coulomb energy ($-\Delta E_c$) is smaller than
the increase in the surface energy (ΔE_s). On the other hand
if $\left| \dfrac{\Delta E_c}{\Delta E_s} \right| \geqslant 1$, the charged-nucleus becomes unstable against
small deformations. The liquid drop model successfully
explained the gross features of the nuclear fission process.
Some of the fission characteristics such as asymmetric mass
distribution of fission fragments for low energy fission
and fission fragment angular distribution could not be

explained on the basis of liquid drop model.

Bohr and Wheeler [14] also introduced the concept of fission exit channels in terms of saddle point configurations. The exit channels were defined as the fragmentation of the nucleus into two definite nuclear species in the given excited states. The idea of fission exit channels was later extended by A. Bohr in 1956 [15]. He formulated a more generalized model of fission known as the 'Unified Model of Fission' which is described below:

For excitation energies of the compound nucleus not too far above the fission threshold, the nucleus is cold at the saddle point since a major part of its energy is bound in the potential energy of the deformation. The quantum states available to the nucleus at the saddle point are, therefore, widely separated and represent relatively simple type of collective excitation of the nucleus. These states are expected to resemble the ground state excitations of the deformed nucleus, that is, the fission channels at the saddle point form a spectrum similar to the low-lying states of the stable deformed nucleus.

Fig. 1.1 shows the spectrum of nuclear levels for an even-even nucleus as a function of a symmetric deformation parameter using LDM type of barrier. It is assumed that the nuclear shape remains axially symmetric during the passage through the saddle point. The channels are then
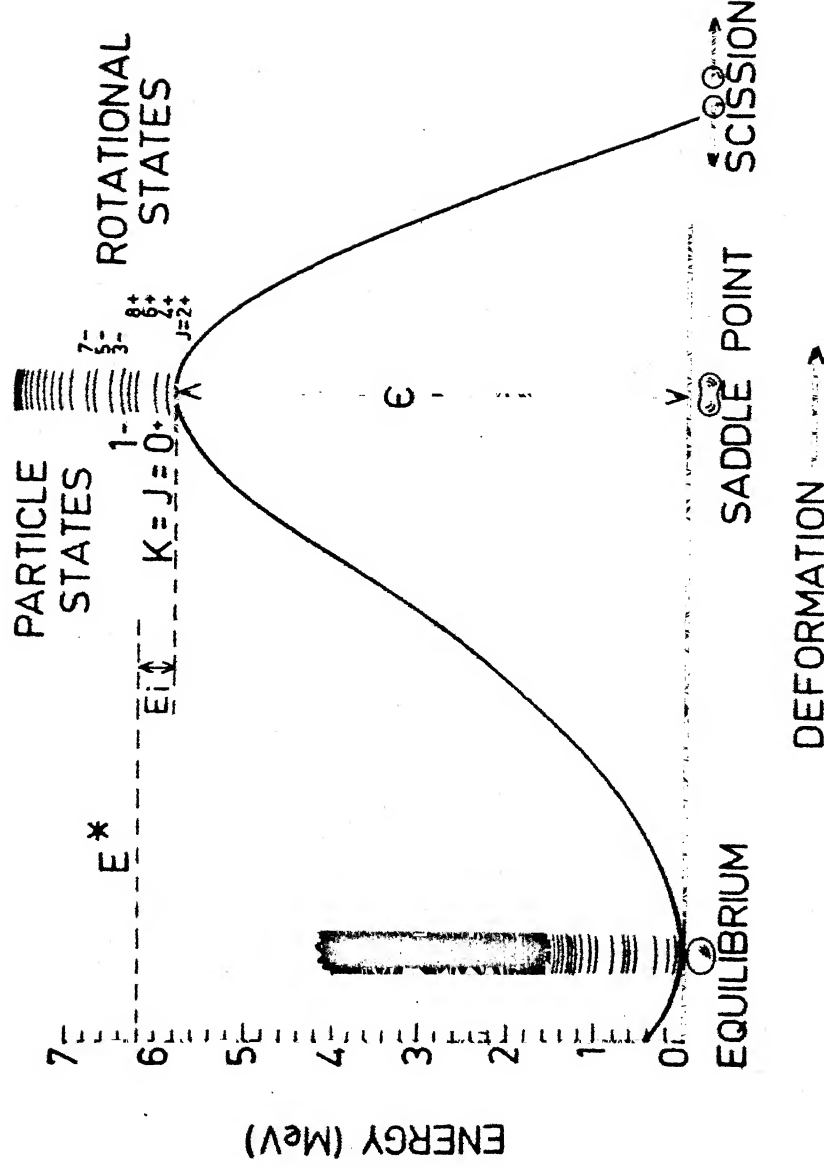
Fig.1.1. Schematic representation of levels at the saddle-point deformation for an even-even fissioning nucleus. (After A. Bohr [15]).

characterized by the quantum number K^π, representing the
component of the nuclear angular momentum J along the body
symmetry axis. For even-even nuclei the lowest state of the
nucleonic structure has K = 0, corresponding to a paired
nucleon configurations. With this intrinsic state, the
associated rotational bands are given by

$$E_{J,K} = E_K + \frac{\hbar^2}{2I} J(J+1) \tag{1.1}$$

where J is the total angular momentum (spin) and I is
the effective moment of inertia. The quantity $(\hbar^2/2I)$ depends
on the deformation and its value is about 7 keV for ground
states of the very heavy elements while the value of this
quantity is smaller at larger deformations.

For nuclei whose shapes possess reflection symmetry the
spectrum for K = 0 contains only even valued rotational levels
such as J = 0, 2, 4, ... etc. all having positive parity.
The rotational band also contains odd J values having negative
parity. These states correspond to excitations of the vibra-
tional states of the deformed nucleus which do not possess
reflection symmetry. These states are antisymmetric with
respect to rotations about 180° and hence give rise to the
negative parity states such as 1^-, 3^-, ... These states
are displaced with respect to the positive parity states by
an amount $\hbar\,w$, where w is the frequency of tunneling motion
between the mirror shapes of the preferred symmetry. The

higher the degree of asymmetry the smaller the w. These low-lying excitations of the nuclear ground state have been observed to occur in the even isotopes of Radium and Thorium with energies in the region of 200 to 300 keV [16]. The energies increase as one goes to still higher elements.

At saddle point, even-even nuclei are expected to have a lowest state of $J^\pi = 0^+$ and close lying collective excitation of 2^+, 4^+, ... etc. as well as states such as 1^-, 3^-....... at somewhat higher energies. Apart from these collective rotational excitations, the nucleus possesses states corresponding to the excitation of the nucleonic configuration, that is, single particle excitations. Since these require the breaking up of a nucleon pair, there will be a significant energy gap ($\sim$1 MeV) between the lowest configuration and the first excited configuration. After this gap the spacing between intrinsic excitation is only of the order of a 100 keV, corresponding to the average spacing of individual particle orbits. With each such intrinsic excitation, characterized by a definite K, there is associated a rotational band with $J = K$, K+1, K+2, ... and both parities.

In odd-A nuclei the lowest K-value is given by the component of angular momentum of the last odd nucleon in its lowest binding state. At saddle point this lowest K-value differs, in general, from the nuclear ground state. The spacing between the states of the last odd particle is of

the order of a few hundred keV. Therefore, the intrinsic
excitations in odd-A nuclei involve no energy gap similar
to that characterizing the paired configuration in even-even
nuclei. With each particle configuration is associated
a rotational band with J = K, K+1, K+2, ... etc. and both
parities. Similarly in odd-odd nuclei the intrinsic excita-
tions would be closely spaced.

Slow neutron ($\ell = 0$) capture by an even-odd nucleus
of spin J_0 leads to a compound nucleus of even-even type
having spin $J = J_0 \pm 1/2$ having same parity as that of the
target nucleus. The transition states will contain only one
of these spin parity combinations in the rotational band
associated with the lowest nucleonic configuration (K = 0) and
therefore the fission thresholds for the two types of compound
nucleus levels are expected to differ appreciably ($\Delta \sim 1$ MeV).
This indicates that, in slow neutron fission, the transition
state is well defined and is expected to influence the fission
characteristics such as the angular distribution, mass
distribution and kinetic energy distribution of fission
fragments, fission widths of the resonances, prompt neutron
and prompt gamma ray emission and energy spectra and emission
probabilities of different light-charged-particles emitted
in fission.

At higher neutron energies, higher partial waves such
as $\ell = 1,2,3,....$ etc. participate in fission process. The

fission cross sections for different partial waves vary significantly with the incident neutron energy. Rae et al. [17] calculated the neutron capture and elastic scattering cross-sections of ^{235}U upto E_n = 1.1 MeV on the basis of the statistical theory of nuclear reactions using ℓ = 0,1,2,3 partial waves. The results are shown in Fig. 1.2. It is seen that the p-wave (ℓ = 1) cross section rises rapidly with energy and becomes equal to the s-wave (ℓ = 0) cross section at E_n = 100 keV. At neutron energies in the energy interval between 100 keV to 500 keV, the p-wave contribution becomes about 50 % - 60 % of the total fission cross section. The d-wave (ℓ = 2) component also increases with energy and at E_n = 500 keV it becomes the same as that of s-wave neutrons. The contribution of other higher partial waves ($\ell > 2$) is negligible in this energy region.

Depending upon the incident neutron energy, these channels influence the fission process to varying extents. In the s-wave fission of $^{235}U(7/2^-)$ the states accessible to the nucleus would be 3^- and 4^- and in p-wave fission these would be 2^+, 3^+, 4^+ and 5^+. The relative predominance of either of these states would depend on the relative predominance of the partial fission cross sections in the neutron energy region under study. If the neutron energy spread is not too large, one or a few of these states can be selectively excited and the fission characteristics resulting thereby can be studied in the low-energy fission. At still higher neutron energies,
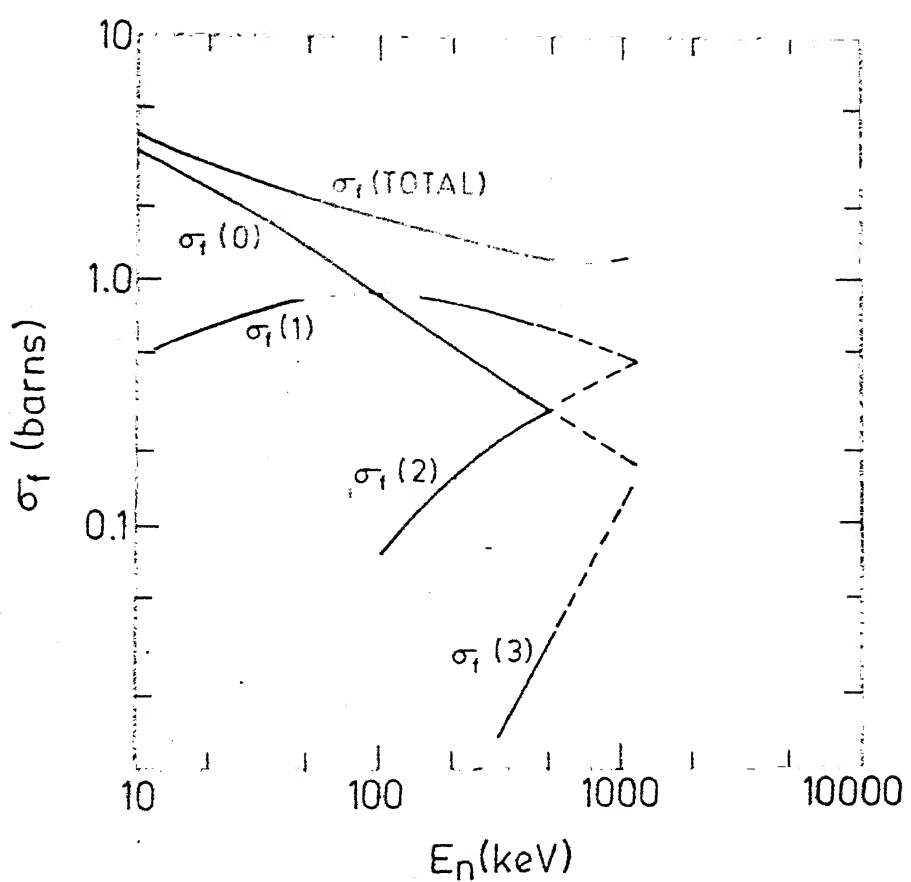
Fig.1.2. Calculated partial wave fission cross sections for neutron induced fission of ^{235}U at various neutron energies upto 1 MeV. (After Cuninghame etal. [17]) .

the channel density increases and therefore many channels participate and these effects are expected to average out.

The most important contribution of the Bohr's unified model was to explain the fission fragment angular distribution using the simple symmetric top model and the quantum numbers characterizing the fission channels. At low neutron energies, the angular momentum vector remains predominantly perpendicular to the body symmetry axis (small K-values play a role), the expected fission fragment angular distribution would be forward peaked which agrees well with the experimental observation [18]. The distributions in fast neutron-induced fission and photo-fission have also been understood in terms of K-bands limited to lower values.

In the low energy fission, the asymmetric mass distribution of the fission fragments is the most puzzling fission characteristic. The corresponding asymmetry parameter is defined as the ratio of peak-to-valley (R) which is expected to differ from resonance to resonance. The studies on $^{235}U(n,f)$ [19,20] and $^{239}Pu(n,f)$ [20,21] for $E_n \leqslant 600$ keV have revealed that the peak-to-valley ratio is a strong function of the spin and parity of the transition state of the fissioning nucleus.

The decrease in the average total fragment kinetic energy in the neutron-induced fission of ^{235}U around $E_n = 200$ keV by about 0.6 MeV [22] and corresponding increase in the

average number of prompt neutrons per fission also reveal the success of the fission channel theory of Bohr.

In 1967, Strutinsky [23] incorporated the shell effects into the liquid drop model and obtained the double-humped fission barrier. These barriers have been quite successful in explaining the recent observed phonomenon known as the fission isomers. Fig. 1.3 shows the double-humped fission barrier along with the LDM type of single-humped fission-barrier. The conclusions are unaltered whether one uses single-humped or double-humped fission-barrier for the purpose of the unified model of fission. In the case of double-humped type of barrier, the channels corresponding to the higher hump are relevant to the fission process.

Since the angular distribution, mass distribution and kinetic energy distribution of fission fragments and prompt neutrons and prompt gammas are influenced by the properties of the saddle states, it is expected that the emission probabilities and energy spectra of different light-charged-particles may also be affected by these states. The light-charged-particle accompanied fission along with the various models used to understand it is described in the following Sections.

1.3 Light-Charged-Particle Accompanied Fission

Light-charged-particle accompanied fission was first observed by Alvarez [24]. Such a division normally occurs once in

average number of prompt neutrons per fission also reveal the success of the fission channel theory of Bohr.

In 1967, Strutinsky [23] incorporated the shell effects into the liquid drop model and obtained the double-humped fission barrier. These barriers have been quite successful in explaining the recent observed phonomenon known as the fission isomers. Fig. 1.3 shows the double-humped fission barrier along with the LDM type of single -humped fission-barrier. The conclusions are unaltered whether one uses single-humped or double-humped fission-barrier for the purpose of the unified model of fission. In the case of double-humped type of barrier, the channels corresponding to the higher hump are relevant to the fission process.

Since the angular distribution, mass distribution and kinetic energy distribution of fission fragments and prompt neutrons and prompt gammas are influenced by the properties of the saddle states, it is expected that the emission probabilities and energy spectra of different light-charged-particles may also be affected by these states. The light-charged-particle accompanied fission along with the various models used to understand it is described in the following Sections.

1.3 Light-Charged-Particle Accompanied Fission

Light-charged-particle accompanied fission was first observed by Alvarez [24]. Such a division normally occurs once in

Fig. 1.3. Schematic illustrations of single-humped (-----) and double-humped (———) fission barriers. Intrinsic excitations in the first and second wells are designated class I and class II states, respectively. The transition in the shape of the nucleus as a function of deformation is schematically represented in the upper part of the figure. The spontaneous fission of the ground state and isomeric state occurs from the lowest energy class I and class II states, respectively. (Ref, [10]).

about every 500 fissions. Several light-charged-particles
such as ^1H, ^2H, ^3H, ^3He, ^4He, ^6He, ^8He, ^6Li, ^7Li, ^8Li, ^9Li,
^7Be, ^9Be, ^{10}Be, B, C, N, and O have been observed in thermal
neutron induced fission of ^{233}U, ^{235}U and ^{239}Pu and in
spontaneous fission of ^{252}Cf. The alpha particles [25-32]
(long-range alpha-particles or LRA) constitute the bulk
(~ 90 %) of the total light-charged-particle yield. Next to
alpha particles are the tritons with an abundance of about 6
to 7 percent. The yield of protons has been reported to
be about 2 percent while the other light-charged-particles
come out with still small probability. The energy distribu-
tions of these particles are observed to have Gaussian shapes.
The most probable (mean) energies of alpha particles, tritons
and protons are about 15 MeV, 8.5 MeV and 8.5 MeV respectively.

Since majority of the light-charged-particles consist
of long-range alpha-particles, the long-range alpha-particle
accompanied (LRA accompanied) fission is the most extensively
studied light-charged-particle accompanied fission for thermal
neutron induced fission of ^{235}U and spontaneous fission of
^{252}Cf. Various correlations between the fission fragment
characteristics and alpha particle characteristics have been
determined experimentally. These correlations are important
due to the interesting possibility of obtaining information
about scission configuration from trajectory calculations.
Review articles of Feather [33] and Halpern [34] give a good

summary of the experimental work in the area of light-charged-particle accompanied fission with special attention on long-range alpha-particle (LRA) accompanied fission. There have been many experiments in which certain features observed in normal binary fission are compared with the same features in the LRA accompanied fission. It is found that the LRA accompanied fission has all the essential characteristics similar to those of binary fission except those having to do with energetics. In the thermal neutron induced fission of ^{235}U, the two main fragments in LRA accompanied fission have mean kinetic energy of 155 MeV which is about 15 MeV less than the same in the binary fission [35]. Similar results were also obtained for spontaneous fission of ^{252}Cf [36]. The mean fragment kinetic energy in LRA accompanied fission is reduced from that in binary fission by about the same amount for all fission fragment-mass-ratios [37]. This has also been confirmed for light-charged-particle accompanied fission in which tritons and protons are released [38].

The mass distribution in binary fission and LRA accompanied fission are very similar. The mass distributions in triton- and proton-accompanied fission have also been obtained [38] and it has been found that the distribution in proton-accompanied fission is quite different as compared to that in the binary fission.

Some measurements [36] have been carried out on the
prompt neutron emission in the LRA accompanied fission which
showed that there are about 0.7 fewer neutrons per fission
emitted in LRA accompanied fission as compared to the binary
fission, although the neutron energy spectra are similar in
both the types of fission. In triton- and proton-accompanied
fission, the average neutron number is less by about 0.3
neutrons per fission as compared to binary fission. The
prompt gamma characteristics in LRA-accompanied fission are
also similar to those in binary fission [39].

One of the most striking features about light-charged-
particle emission in fission is the angular distributions of
these particles with respect to the fission fragment direction.
The angular distributions of all these particles are peaked
around 90° with a width of about 20-25 degrees with the
exception of protons, which are found to have a very wide
angular distribution [28]. Due to the similarity of the
energy spectra and angular distributions of all these
particles, they are believed to be emitted by the same
mechanism. Although most of the light-charged-particles have
angular distributions peaking around 90° with respect to the
fission fragment direction, a small percentage (about 2 %)
is also found to be emitted along the fission fragment
direction. These particles, termed as polar particles, have
been studied by Piasecki et al. [40] in the case of thermal

neutron fission of ^{235}U and it has been found that the relative yields of different polar-light-charged-particles are quite different from those of normal or equatorial-light-charged-particles.

The angular distributions of light-charged-particles led to the belief that the light-charged-particles are emitted very close to the moment of scission from the neck connecting the two heavy fragments. Once these particles are emitted their motion would be influenced by the Coulomb field of the fission fragments and their final energies and angular distributions would be sensitive to the separation and speed of the fragments at the instant of their emission and therefore the study of these particles is expected to provide useful information about the scission stage of the fission process. The correlations between various characteristics of these particles and fission fragments also contain the information regarding their emission mechanism. There have been various models to understand the emission mechanism of these light-charged-particles in fission but none of them is able to explain all the observed characteristics. These models are described in the Section 1.4 below.

An important characteristic of LRA accompanied fission is the observed anti-correlation between the average total fragment kinetic energy and the alpha particle energy. Measurements [37,41] on the multidimensional correlations

between the energies and masses of fission fragments and energy and angle of the long-range alpha-particles emitted from thermal neutron induced fission of ^{235}U have led to the conclusion that the average total fragment kinetic energy $\langle E_k \rangle$ decreases as the alpha particle energy increases. The average slope $(d \langle E_k \rangle /dE_\alpha)$ was found to be about -0.32 for 10 MeV $\leqslant E_\alpha \leqslant$ 26 MeV. Similar results [42] have also been obtained in the case of spontaneous fission of ^{252}Cf. This anti-correlation plays an important role in interpreting trajectory calculation results.

1.4 Models of LCP Emission in Fission

The LRA accompanied fission has been studied most extensively because of its high probability of emission and various correlations have been measured. These include the correlations between various fission fragment characteristics and LRA energy, angle of emission with respect to fission axis. To understand these correlations, several models of alpha particle emission have been proposed in the past. A brief discription of some of these models is given below.

(i) Pre-scission evaporation model

This model [43] assumes that the alpha particle is evaporated from the fissioning nucleus just before scission and then the nucleus undergoes fission. It was based on the

following observations : (i) the sum of most probable kinetic

energies of the fragments in ~~ternary~~ LCP fission and binary fission are

nearly equal, (ii) the probability of ~~ternary~~ LCP fission does

not depend on the mass ratio of the fission fragments, (iii)

lesser number of prompt neutrons are emitted from ~~ternary~~ LCP

fission as compared to binary fission and, (iv) the angular

distribution of the alpha particles is forward/backward

peaked relative to incident neutron direction in the 14 MeV

neutron fission of ^{238}U [43]. One of the strong evidences

in favour of this model is the angular distribution of alpha

particles with respect to the neutron direction in the fast

neutron fission of ^{235}U [44] which is the characteristic of

the particles evaporated from a compound nucleus. The

measured anisotropy agreed well with the calculated one for

alpha particles emitted from a fissioning nucleus having a

large angular momentum. Agreement of alpha particle spectrum

obtained on the basis of statistical theory of evaporation

from the compound nucleus at higher excitation energies is

another evidence favouring this model [44]. However an

important objection against this model was that the

temperature of the compound nucleus calculated from this

model (0.63 MeV) was completely different from that calculated

on the basis of scission neutrons.

(ii) Post-scission evaporation model

To explain the mass distribution of the fission
fragments in ternary fission, Feather [45] assumed that the
light-charged-particle is evaporated from one of the fragments
just after the scission point. Furthermore, the particle
emission was assumed to occur before the recoiling fragment
had acquired more than a small fraction of its final energy.
By comparing the mass distribution in long-range alpha-particle
accompanied fission and binary fission, the probability of
emission of the alpha particles was calculated using the
following expressions:

$$P(A_L) = T(A_{L-4}, A_H, 4)/B(A_L, A_H),\qquad(1.2a)$$

$$P(A_H) = T(A_L, A_{H-4}, 4)/B(A_L, A_H)\qquad(1.2b)$$

where $P(A_L)$, $P(A_H)$ are the probabilities of alpha particle
emission from either fragment A_L or A_H of the fissioning
nucleus. $B(A_L, A_H)$ is the probability of fission into
fragments A_L and A_H in binary fission and $T(A_\ell, A_h, 4)$ is the
probability of LRA fission for the mass division in A_ℓ, A_h.
The increase of the probability of long-range alpha-particle
emission with fission fragment mass number showed a sawtooth
dependence with zero probability for symmetric fission [46]
which exactly parallels the variation of prompt neutrons with
the mass number of the fission fragment and hence provide a

significant support for the hypothesis of this model. Another
evidence in favour of this model is that the mean number of
prompt neutrons and the mean probability of long-range alpha-
particle emission both increase with the mass number of the
fissioning nucleus for low-energy fission. The following
points are against the hypothesis that the alpha particles
accompanying fission are evaporated from the fragments just
after scission : (i) The probability of long-range alpha-
particle emission decreases whereas the number of prompt
neutrons increases with the excitation energy of the compound
nucleus. (ii) A typical evaporation time significantly exceeds
the time ($\sim 10^{-21}$ Sec) that the fragments remain sufficiently
close to each other to provide a field strong enough to account
for the observed angular distribution of the alpha particles.
(iii) If the alpha particles were evaporated, they would tend
to be emitted from the outer ends of the fragments rather than
into the central region where the Coulomb barrier is much
thicker. The angular distribution of alpha particles would be
expected to be forward peaked. (iv) The relative evaporation
rate compared with that for neutrons would be expected to be
much less than the observed rate.

(iii) Sudden-snap model

For an alpha particle or other light-charged-particle
in fission to be able to acquire a very large share of the

available energy that it needs to be released between the
fragments, this energy must in the meantime be stored in the
readily convertible form. This model [47] assumes that just
before scission the nucleus is highly distorted and thus has
a large fraction of its energy in the form of the deformation
energy. Then it suddenly breaks up giving rise to sudden
collapse of distortions. A large fraction of the deformation
energy then goes into the individual particle degrees of
freedom. This gives a finite probability for individual
particle to acquire sufficient energy from the sudden
changing potentials and become free. Later, particle gets
accelerated by the Coulomb forces of the two fission
fragments. This model has been used only for some qualitative
explanation. No detailed quantitative calculations were
carried out with this model for comparision with the
experimental results. However, the energy cost for the
emission of different light-charged-particles were computed.
The average energy cost (E_c), also known as the release
energy (E_R), for the production of different particles was
obtained using the following expression;

$$E_c = B + \triangle V + K, \qquad (1.3)$$

where B is the average binding energy of the emitted light-
charged-particle to its mother fragment, $\triangle V$ is the average
difference in the Coulomb energy between the corresponding

binary and ternary fission configurations, and K is the
average kinetic energy with which the third particle is
born. The binding energy (B) can be calculated from the
mass tables. For alpha particles, it is about 5 MeV. Halpern
[34] calculated ΔV under certain assumption regarding the
binary and ternary scission configurations using the
expression;

$$\Delta V = (\frac{Z_2 Z_3}{d} + \frac{Z_1 Z_3}{4d}) e^2, \qquad (1.4)$$

where Z_1, Z_2 are the charges of the mother fragments, Z_3 is
the charge of the light-charged-particle and 2d is the charge
distance between the two binary fragments. The light-charged-
particle (Z_3) is removed from Z_2 and placed in the middle
such that the centre of mass of the system is unaltered.
The estimated value of ΔV for alpha particles from ^{236}U
fission was found to be about 19 MeV.

In the absence of an explicit model, it is impossible
to estimate K. However, assuming sudden collapse of the
neck in the scission nucleus and considering the phase space
available for the third particle, it was estimated to be
about 2 MeV for an alpha particle, smaller by an order of
magnitude compared to $(B+\Delta V)$.

The total energy cost (E_c) is pressumably made
available for the light-charged-particle release at the
expense of the kinetic plus distortion energies of the two

main fragments at the moment of scission. The larger the
amount of energy that must be transferred in this way from
the fragments to the third particle, the smaller the proba-
bility for the transfer process, and hence the yield of
light-charged-particles is expected to be decreasing
function of energy cost (E_c). The measured yield of the
light-charged-particles ($Z \geqslant 2$) are found to be related to
E_c by the following expression;

$$y \quad \propto \quad \exp(-E_c/T) \tag{1.5}$$

where T is the nuclear temperature. From observed neutron
spectra in low-energy fission, T is known to be about 1 MeV
at scission. The observed triton yield is, however, about
a factor of 10 less than that expected from Eq. (1.5). For
protons and deuterons the case is even worse. The unique
scission point configuration derived from the recent
experimental results on the various correlations between
fission fragment mass, kinetic energy and alpha particle
energy and angle may give clear evidence for Halpern's model.

(iv) Statistical model

The statistical model of fission [48] assumes the
existence of a well-defined scission configuration, upto
which non-adiabatic effects maintain statistical equilibrium,
and beyond which no nuclear interactions occur between the

fission fragments. In the theory, the relative probability
of different scission-configurations (characterized by mass,
charge, deformation, and kinetic energy of the nascent
fragments) is proportional to the density of translational
and excitational states for said configuration. The relative
probability of any mode can be calculated by knowing the
excitation energies of the fission fragments at the time of
scission which can be determined from the experimental results
on the prompt neutron and gamma emission.

Taking intial conditions of long-range alpha-particle
accompanied fission of ^{252}Cf based on statistical theory,
Ertel [49] did some trajectory calculations. A good agreement
with the experimental results for angular distributions was
obtained. More refined trajectory calculations on this line
were carried out by Fong [50-51] and Brown and Fong [52] for
long-range alpha-particle accompanied fission of ^{252}Cf and
thermal neutron induced fission of ^{235}U. The results of these
calculations on (a) the angle of the alpha particle with the
fission fragment as a function of the mass number of the
fragment, (b) the kinetic energy of the alpha particle as a
function of the mass ratio of the fission fragments, and (c)
the total kinetic energy of the two main fragments as a
function of the mass ratio of the fission fragments are in
good agreement with the experimental results.

In 1971, P. Fong [53] applied the statistical theory
of fission to the ~~ternary~~ LCP fission to estimate the probability

of long-range alpha-particle accompanied fission relative to the binary fission. According to this model, the relative probability for a scission configuration with a specific charge and mass division is a function of the excitation energy of the system at the scission point and the level density parameters of the two fission fragments. The relative probability of LRA to binary fission was given by the expression;

$$\frac{P_{LRA}}{P_B} = \frac{E_{LRA}^{11/4}\left\{1 - \frac{19}{4}[(a_1'+a_2')E_{LRA}]^{-1/2}\right\}\exp 2[(a_1'+a_2')E_{LRA}]^{-1/2}}{E_B^{11/4}\left\{1 - \frac{19}{4}[(a_1+a_2)E_B]^{-1/2}\right\}\exp 2[(a_1+a_2)E_B]^{-1/2}}$$

$$\cdots\cdots \quad (1.6)$$

where E's indicate the excitation energy of the system at the scission point, a_1 and a_2 are the level density parameters of the two fission fragments. Using the experimentally obtained values of a_1, a_2, a_1', a_2', E_{LRA} and E_B for thermal neutron induced fission of ^{235}U, Fong found P_{LRA}/P_B to be equal to (1/461) which agrees well with the experimental value of (1/449±30). The value of this ratio for spontaneous fission of ^{252}Cf was found to be about (1/149) which is about a factor of two larger compared to the experimental value of (1/299±18). This disagreement is not understood.

A practical problem with this model is that the evaluation of the probability expression requires fragment

deformation energies and level densities at deformations where direct experimental information is not available and therefore it involves a lot of empirical parameters.

The trajectory calculations based on the statistical theory of fission [49-52] predicted that the initial energies of fission fragments and the initial alpha particle energy have very low values ($E_F^O \backsim 1$ MeV and $E_\alpha^O \backsim 0.5$ MeV). Apart from these, some other trajectory calculations [28,54,55] have also been carried out to reproduce the experimental observations such as the alpha particle energy distribution, angular distribution and various other correlations between fission fragment characteristics and those of alpha particles. These calculations have predicted very large values of initial energies of fission fragments and alpha-particles ($E_F^O \backsim 25 - 40$ MeV and $E_\alpha^O \backsim 3 - 4$ MeV) instead of small values as predicted by statistical theory of fission.

1.5 Motivation of the Present Work

The yield of long-range alpha-particles has been observed [56] to increase with the fissility parameter (Z^2/A). Since the deformation increases with Z^2/A (as indicated by liquid drop model), the yield is directly dependent on the extent of the deformation at the scission point.

As mentioned in the Section 1.2, the emission probability and the energy distribution parameters such as

average energy and width of different light-charged-particles may also be affected by the spin and parity of the transition states (saddle point states). Wagemans and Deruytter [57-59] made measurements on the yield of long-range alpha-particles emitted from neutron induced fission of ^{235}U, ^{239}Pu and ^{241}Pu in the neutron energy region from thermal to 50 eV and found that the ratio of long-range alpha-particle accompanied fission to binary fission varies from resonance to resonance. They observed that the ratio of LRA accompanied fission to binary fission for some of the resonances has very low value while very high for others. The measurements of Melkonian and Mehta [20] and Schröder et al. [60] have also shown the variation of LRA emission probability from resonance to resonance.

Krishnarajulu et al. [61] studied the light-charged-particle accompanied fission of ^{235}U induced by neutrons of energies in the region from thermal to 1 MeV. The yields of long-range alpha-particles and tritons and the energy distribution parameters of alpha particle energy spectrum at various incident neutron energies were determined. The alpha particle yield showed some structure around neutron energy of 200 keV. At higher neutron energies ($E_n \geqslant 500$ keV) the alpha particle yield was found to have the same value as that of thermal neutrons. The most probable energy and the width of alpha particles did not show any appreciable

variation with the neutron energy. The LRA yield structure
around E_n = 200 keV was attributed due to the change in the
parity of transition state of the fissioning nucleus (parity
changes due to p-wave fission in this energy region). The
yield of light-charged-particles having energies $E_{LCP} < 12$ MeV
was expected to contain tritons and therefore the triton
yield was extracted from these events. The triton yield was
found to increase with neutron energy and at E_n = 500 keV,
the yield was found to be about three times that of thermal
neutrons. The yield showed a decrease tending towards the
thermal value for neutron energies above 500 keV. In these
measurements no particle identification was done.

The present work is the extension of the previous
work carried out by Krishnarajulu et al. [61]. A multi-
parameter study of protons, tritons and alpha particles has
been carried out in the neutron induced fission of ^{235}U for
neutron energies in the range from thermal to 700 keV in the
first part of the experiment. For particle identification,
a semiconductor $\triangle$E-E detector telescope was used. The
fission fragments were detected in a thin layer ionization
chamber. The main purpose of the present work was to study
in detail the yields and energy spectra of different light-
charged-particles such as protons, tritons and alpha particles
in the neutron energy region from 100 keV to 1 MeV. The
results are presented and discussed in the Chapter II.

In the high neutron flux required for LCP accompanied fission experiments, the radiation damage in the semiconductor detectors makes the use of these detectors very uneconomic. Since the solid state nuclear track detectors (SSNTDs) are unaffected by beta particles, gammas and neutrons, we have developed a technique (known as the rear-etching technique) using a cellulose nitrate track detector (CNTD) for studying the fine structure, if there is any, in the LRA yield in the neutron energy region from 100 keV to 500 keV. This technique is described in Chapter III.

Using a cellulose nitrate track detector in conjunction with the rear-etching technique, we have performed measurements on the LRA accompanied fission of ^{235}U induced by neutrons in the range from thermal to 500 keV. These measurements are carried out at several neutron energies with small neutron energy spreads. The results are presented and discussed in the Chapter IV.

The results are summarized in the Chapter V. The conclusions derived on the basis of the present work are also discussed there.

REFERENCES

[1] O. Hahn and F. Strassman, Naturwissenschaften 27 (1939) 89.

[2] L. Meitner and O.R. Frisch, Nature (London) 143 (1939) 239.

[3] O.R. Frisch, Nature (London) 143 (1939) 276.

[4] M.L. Muga and C.R. Rice, Proc. Second Symp. Phys. Chem. Fission (held in Vienna) (1969) p. 107 (IAEA, Vienna); M.L. Muga, C.R. Rice and W.A. Sedlacek, Phys. Rev. Lett. 18 (1967) 404; M.L. Muga, C.R. Rice and W.A. Sedlacek, Phys. Rev. 161 (1967) 1266; M.L. Muga, Proc. First Symp. Phys. Chem. Fission (held in Salzburg) Vol. II (1965) p. 409 (IAEA, Vienna).

[5] S.S. Kapoor, R.K. Choudhury, S.K. Kataria, S.R.S. Murthy and V.S. Ramamurthy, Proc. Nucl. Phys. and Solid State Phys. Symp. (India) 15B (1972) 107.

[6] S.K. Kataria, E. Nardi and S.G. Thompson, Proc. Third Symp. Phys. Chem. Fission (held in Rochester) Vol. II (1973) p. 389 (IAEA, Vienna).

[7] D.C. Hoffman and M.M. Hoffman, Ann. Rev. Nucl. Sci. 24 (1974) 151.

[8] W. Reisdorf, J.P. Unik, H.C. Griffin and L.E. Glendenin, Nucl. Phys. A177 (1971) 337.

[9] V.N. Okolovich and G.N. Smirenkin, Atomnaya Energiia 15 (1963) 250.

[10] R. Vandenbosch and J.R. Huizenga, ''Nuclear Fission'', New York : Academic Press (1973).

[11] S.S. Kapoor, R. Ramanna and P.N. Rama Rao, Phys. Rev. 131 (1963) 283.

[12] K. Skarsvag and K. Bergheim, Nucl. Phys. 45 (1963) 72.

[13] E.K. Hyde, ''The Nuclear Properties of Heavy Nuclei'', Vol. II Fission Phenomenon, Engle-wood Cliffs, New Jersey: Prentice Hall (1964)

[14] N. Bohr and J.A. Wheeler, Phys. Rev. 56 (1939) 426.

[15] A. Bohr, Proc. Int. Conf. Peaceful Uses of At. Energy Geneva 2(1956) 151, United Nations, New York.

[16] F. Stephens, Jr., F. Asaro and I. Perlman, Phys. Rev. 96 (1954) 1568.

[17] E.R. Rae, B. Margolis and E.S. Troubetskoy, Phys. Rev. 112 (1958) 492; J.G. Cuninghame, G.P. Kitt and E.R. Rae, Nucl. Phys. 27 (1961) 154.

[18] A.N. Behkami, J.H. Roberts, W.D. Loveland and J.R. Huizenga, Phys. Rev. 171 (1968) 1267.

[19] G.A. Cowan, B.P. Bayhurst, R.J. Prestwood, J.S. Gilmore and G.W. Knobeloch, Phys. Rev. C-2 (1970) 615.

[20] E. Melkonian and G.K. Mehta, Proc. First Symp. Phys. Chem. Fission (held in Salzburg) Vol. 2 (1965) p. 355 (IAEA, Vienna).

[21] G.A. Cowan, B.P. Bayhurst, R.J. Prestwood, J.S. Gilmore and G.W. Knobeloch, Phys. Rev. 144 (1966) 979.

[22] Yu. A. Blyumkina, I.I. Bondarenko, V.F. Kuznetsov, V.G. Nesterov, V.N. Okolorich, G.N. Smirenkin and L.N. Usachev, Nucl. Phys. 52 (1964) 648.

[23] V.M. Strutinsky, Nucl. Phys. A95 (1967) 420.

[24] G. Farwell, E. Segre and C. Wiegand, Phys. Rev. 71 (1947) 327.

[25] M. Dakowski, J. Chwaszczewska, T. Krogulski, E. Piasecki and M. Sowinski, Phys. Lett. B25 (1967) 213.

[26] S.L. Whetstone, Jr. and T.D. Thomas, Phys. Rev. 154 (1967) 1174.

[27] S.W. Cosper, J. Cerny and R.C. Gatti, Phys. Rev. 154 (1967) 1193.

[28] G.M. Raisbeck and T.D. Thomas, Phys. Rev. 172 (1968) 1272.

[29] T. Krogulski, J. Chwaszczewska, M. Dakowski, M. Sowinski and J. Tys, Nucl. Phys. A128 (1969) 219.

[30] A.A. Vorobiev, D.M. Seleverstov, V.T. Grachov, I.A. Kondurov, A.M. Nikitin, A.I. Yegorov and Yu.K. Zalite, Phys. Lett. B30 (1969) 332.

[31] A.A. Vorobiev, D.M. Seleverstov, V.T. Grachov, I.A. Kondurov, A.M. Nikitin, N.N. Smirnov and Yu.K. Zalite, Phys. Lett. B40 (1972) 102.

[32] A.A. Vorobiev, V.T. Grachov, I.A. Kondurov, Yu.A. Mireshnichenko, A.M. Nikitin, D.M. Seliverstov and N.N. Smirnov, Sov. J. Nucl. Phys. 20 (1975) 248.

[33] N. Feather, Proc. Second Symp. Phys. Chem. Fission (held in Vienna) Vol. II (1969) p. 83 (IAEA, Vienna).

[34] I. Halpern, Ann. Rev. Nucl. Sci. 20 (1971) 245.

[35] M. Asghar, C. Carles, R. Chasterl, J.P. Doon, M. Bibrag and C. Signarbieux, Nucl. Phys. A145 (1970) 657.

[36] H. Piekarz, J. Blocki, T. Krogulski and E. Piasecki, Nucl. Phys. A146 (1970) 273.

[37] R.K. Choudhury, S.S. Kapoor, D.M. Nadkarni, P.N. Rama Rao and S.R.S. Murthy, Pramäna 6 (1976) 64.

[38] E. Nardi, Y. Gazit and S. Katcuff, Phys. Rev. 182 (1969) 1244.

[39] N.N. Ajitanand, Nucl. Phys. A133 (1969) 625.

[40] E. Piasecki and J. Blocki, Nucl. Phys. A208 (1973) 381; E. Piasecki, M. Sowinski, L. Nowicki, A. Kordyasz, E. Cieslak and W. Czarnacki, Nucl. Phys. A255 (1975) 387.

[41] C. Guet, C. Signarbieux, P. Perrin, H. Nifenecker, M. Asghar, F. Caitucolli and B. Leroux, Nucl. Phys. A314 (1979) 1.

[42] G.K. Mehta, J. Poitou, R. Ribrag and C. Signarbieux, Phys. Rev. C-7 (1973) 373.

[43] R. Ramanna, K.G. Nair and S.S. Kapoor, Phys. Rev. 129 (1963) 1350.

[44] D.M. Nadkarni, Ph.D. Thesis (1970) (Bombay Univ., India).

[45] N. Feather, Proc. Royal Soc. of Edinburgh 66A (1964) 192.

[46] N. Feather, Proc. Royal Soc. of Edinburgh 68A (1969) 229.

[47] I. Halpern, Proc. First Symp. Phys. Chem. Fission (held in Salzburg) Vol. II (1965) 369 (IAEA, Vienna).

[48] P. Fong, Phys. Rev. 102 (1956) 434.

[49] John P. Ertel, Jr., M.S. Thesis, Emory University, 1968, Published by P. Fong, Statistical Theory of Nuclear Fission (Gordan and Breach, Science Publishers, Inc., New York, 1969) p. 191.

[50] P. Fong, Phys. Rev. C-2 (1970) 735.

[51] P. Fong, Phys. Rev. C-16 (1977) 251.

[52] C.S. Brown and P. Fong, Phys. Rev. C-16 (1977) 243.

[53] P. Fong, Phys. Rev. C-3 (1971) 2025.

[54] Y. Boneh, Z. Fraenkel and I. Nebenzahl, Phys. Rev. 156 (1967) 1305.

[55] B. Krishnarajulu and G.K. Mehta, Pramäna 4 (1975) 74.

[56] R.A. Nobles, Phys. Rev. 126 (1962) 1508.

[57] C. Wagemans and A.J. Deruytter, Nucl. Phys. A194 (1972) 657.

[58] C. Wagemans and A.J. Deruytter, Nucl. Phys. A212 (1973) 556.

[59] C. Wagemans and A.J. Deruytter, Nucl. Phys. A234 (1974) 285.

[60] I.G. Schröder, A.J. Deruytter and J.A. Moore, Phys. Rev. B-137 (1965) 519.

[61] B. Krishnarajulu, G.K. Mehta, R.K. Choudhury, D.M. Nadkarni and S.S. Kapoor, Pramäna 8 (1977) 315.

CHAPTER II

MULTIPARAMETER STUDY OF LIGHT-CHARGED-PARTICLES EMITTED IN FAST NEUTRON INDUCED FISSION OF ^{235}U

2.1 Introduction

Once in every several hundred fission events, the fission fragments are accompanied by an additional light-charged-particle. This particular mode of fission is termed as the light-charged-particle accompanied fission (in short LCP fission). These particles were first observed in 1944 by Alvarez [1] in the case of thermal neutron induced fission of ^{235}U. Since then several studies have been carried out. Upto 1960, the amount of information extracted about these particles was limited because of the limitations of the detectors available. The development of the surface barrier detectors and ΔE-E semiconductor detector telescope in early sixties led to a considerable amount of work on these particles and several types of light-charged-particles like

protons, tritons and alpha particles etc. have been reported.
These studies of light-charged-particle accompanied fission
are of particular interest to the theory of the fission
process. The interest arises because the studies of the
angular distributions of these light-charged-particles indicate
that these particles are released in the space between the two
separating fission fragments very nearly at the time of the
actual scission of the fissioning nucleus. The probability of
emission of these light-charged-particles along with their
energy and angular distributions are thus expected to carry
information concerning the configuration of the nucleus at
the time of scission.

The motivation for the study of light-charged-particle
emission in fission is manifold. For example, it is expected
to throw light on (a) the existence and stability of neutron
rich nuclei like He^5, He^6 and He^8 etc., (b) the emission
mechanism of different light-charged-particles from fissioning
nucleus and (c) the scission point configuration. The review
articles of Feather [2] and Halpern [3] give the summary of
the experimental work of the light-charged-particle accompanied
fission along with the various models proposed for understanding
the emission of these particles in fission.

Several measurements [4-12] have been carried out to
study the effect of Z, A, spin and excitation energy of the
compound nucleus on the emission probabilities of different
light-charged-particles and to determine the correlations

between various characteristics of fission fragments and light-charged-particles. The correlations among the fission fragment kinetic energy, mass, light-charged-particle energy and its angle with respect to the fission axis are needed in trajectory calculations to derive a unique set of parameters describing the scission point configuration. Some investigations have been carried out to study the dependence of yields and energy spectra of light-charged-particles on the spin and the excitation energy of the compound nucleus [4-10]. Recently, Krishnarajulu et al. [11-12] performed some measurements on the neutron induced fission of ^{235}U and ^{239}Pu and studied the variation of yields and energy distributions of tritons and alpha particles with neutron energy upto 1 MeV. We have carried out a multiparameter study of ^{1}H, ^{3}H and ^{4}He particles in the neutron induced fission of ^{235}U for the neutron energy range from thermal to 700 keV.

In this chapter, we shall first give a review of the previous experimental work carried out by various authors on the yields and energy spectra of different light-charged-particles emitted from the spontaneous fission of ^{252}Cf and in thermal neutron induced fission of ^{233}U, ^{235}U and ^{239}Pu. Section 2.3 describes the various particle indentifier techniques in brief. In Sections 2.4, 2.5 and 2.6, a detailed description of the experimental method used in our measurements is given. The procedure of data analysis is described in the Section 2.7. The results and discussions are presented in

Section 2.8.   The conclusions drawn from the present study,
are outlined at the end of the chapter.

2.2 Review of Earlier Work

The yields and energy distributions of tritons and
alpha particles emitted from spontaneous fission of ^{252}Cf were
first reported by Watson [13] in 1961. He employed a gas
filled proportional counter as $\frac{dE}{dx}$ detector and a CsI(Tl)
scintillation detector as E-detector. Wegner [14] made use of
$\triangle$E-E semiconductor detector telescope for particle
identification and observed the emission of protons, deuterons,
tritons, ^{3}He and alpha particles from the spontaneous fission
of ^{252}Cf. Using radiochemical techniques, Horrocks [15]
determined the absolute yield of tritons emitted from the
spontaneous fission of ^{252}Cf. In the subsequent year, the
spontaneous emission of ^{6}He from ^{252}Cf was reported by
Whetstone et al. [16] using $\triangle$E-E counter telescope consisting
of two silicon semiconductor detectors. Since then a large
volume of work has been carried out to study the yields,
energy spectra, and angular distributions of different light-
charged-particles (^{1}H, ^{2}H, ^{3}H, ^{3}He, ^{4}He, ^{6}He, ^{8}He, ^{10}He, ^{6}Li, ^{7}Li,
^{8}Li, ^{9}Li, ^{9}Be and ^{10}Be etc.) emitted from spontaneous fission
of ^{252}Cf [17-20], and from thermal neutron induced fission
of ^{233}U [21], ^{235}U [22-26] and ^{239}Pu [27-29]. In some of
these investigations [17-20,22,28], the $\triangle$E-E semiconductor
detector telescopes were used to identify these light-charged-

particles. Andreev et al. [23,27] used a gridded multi-layer ionization chamber for particle identification which measured simultaneously the specific ionization $(\frac{dE}{dx})$, the energy (E), and the range (R) of each particle. Vorobiev et al.[21,24,25, 29] and Kugler et al. [26] carried out measurements on particle identification using a magnetic time-of-flight mass spectrometer which determines simultaneously the energy, time-of-flight over a fixed distance, and magnitude of $H\rho$ for each particle.

From these studies, it is now almost established that the alpha particles form about 90 % of the total light-charged-particles, tritons, and protons form about 6.5 % and 2 % of the total light-charged-particles respectively. The other light-charged-particles come out with comparitively very low probability. The relative yields of protons, deuterons, tritons and alpha particles emitted from thermal neutron induced fission of ^{233}U, ^{235}U and ^{239}Pu and from spontaneous fission of ^{252}Cf are summarized in the Table - 2.1(a). The most probable energies ($\bar{E}$) and the standard deviations (σ_E) for these particles are given in the Table - 2.1(b). It is clear from the table that the most probable energies of alpha particles ($\bar{E}_\alpha$) lie between 15 MeV - 16 MeV, the most probable energies of tritons ($\bar{E}_t$) lie between 8 - 9 MeV and that of protons ($\bar{E}_p$) also lie between 8 - 9 MeV. Raisbeck and Thomas [19] observed that, except protons, all other

Table - 2.1(a) Yields of different light-charged-particles as per 100 alpha particles emitted in thermal neutron-induced fission of ^{233}U, ^{235}U and ^{239}Pu and in spontaneous fission of ^{252}Cf.

Light-charged-particle	Detected energy-range of different light-charged-particles (MeV)				Relative yield (extrapolated) per 100 alpha particles			
	^{252}Cf	^{233}U	^{235}U	^{239}Pu	^{252}Cf	^{233}U	^{235}U	^{239}Pu
^{1}H	7.3-18.8[a] 3.18-19.62[b]		4.5-17.0[e]	4.0-18.0[g]	1.75±0.30[a] 1.60+0.20[b]		1.15±0.15[e]	1.9±0.1
^{2}H	5.3-21.5[a] 3.83-18.22[b]	5.5-13.3[d]	5.5-17.0[e] 4.8-15.0[f]	4.5-19.0[g]	0.68+0.03[a] 0.63±0.03[b]	0.41±0.02[d]	0.50±0.10[e] 0.50±0.02[f]	0.5±0.1 0.69+0.02
^{3}H	6.5-24.3[a] 3.89-23.13[b] 5.00-22.00[c]	4.0-11.0[d]	6.0-17.0[e] 4.2-11.6[f]	5.5-20.0[g]	3.46±0.28[a] 5.90±0.2[b] 7.4±0.3[c]	4.60±0.20[d]	6.20±0.5[e] 7.20±0.3[f]	6.8±0.3 7.2±0.3
^{4}He	8.3-37.7[a] 7.75-34.75[b] 12.0-34.0[c]	3.0-33.2[d]	12.0-32.0[e] 10.6-34.6[f]	10.0-29.0[g]	100	100	100	100

a - [17], b - [18], c - [20], d - [21], e - [22], f - [24], g - [28], h - [29] and i - [35].

Table - 2.1(b)   The energy characteristics of different light-charged-particles emitted in thermal neutron-induced fission of ^{233}U, ^{235}U and ^{239}Pu and in spontaneous fission of ^{252}Cf.

Light-charged-particle	Most probable energy, E (MeV)				Full-width at half maximum (MeV)			
	^{252}Cf	^{233}U	^{235}U	^{239}Pu	^{252}Cf	^{233}U	^{235}U	^{239}Pu
^{1}H	7.8±0.8[a], 9.0±2.0[b]		8.6±0.3[e]	8.40±0.15[g]	6.8±0.8[a], 6.0±2.0[b]		6.9±0.5[e]	7.2±0.3[g]
^{2}H	8.0±0.5[a], 7.0±2.0[b]	8.4±0.2[d]	7.9±0.3[e], 8.06±0.15[f]	8.2±0.2[g], 8.7±0.1[h]	7.2±0.5[a], 7.0±1.0[b]	6.3±0.3[d]	7.0±1.0[e], 7.1±0.2[f]	7.2±0.5[g], 7.6±0.2[h]
^{3}H	8.0±0.3[a], 8.0±1.0[b], 9.0±0.5[c]	8.4±0.2[d]	8.6±0.3[e], 8.2±0.15[f]	8.2±0.15[g], 8.4±0.10[h]	6.2±0.3[a], 6.0±1.0[b], 8.2±0.5[c]	6.5±0.3[d]	6.7±0.6[e], 6.5±0.2[f]	7.6±0.4[g], 7.0±0.15[h]
^{4}He	16.0±0.2[a], 16.0±0.5[b], 16.1±0.8[c]	16.3±0.01[d]	15.7±0.3[e], 15.9±0.1[f], 15.0±0.1[i]	16.0±0.01[g], 15.8±0.1[h]	10.2±0.2[a], 11.5±0.5[b], 13.0±0.7[c]	9.7±0.2[d]	9.8±0.4[e], 9.8±0.1[f]	10.6±0.2[g], 10.3±0.15[h]

a – [17], b – [18], c – [20], d – [21], e – [22], f – [24], g – [28], h – [29] and i – [35].

particles peaked at about 90° from the fission axis. Since
the majority of the light-charged-particles consists of alpha
particles, several multiparameter studies have been carried
out to obtain correlations between mass, kinetic energy of
fission fragments and alpha particle energy and angle to
understand the emission mechanism of these particles. The
most recent studies of this type are those of Guet et al. [30]
and Choudhury et al. [31].

Drapchinski et al. [32], Thomas and Whetstone [33],
and Loveland et al. [34] carried out some measurements on the
total yield of light-charged-particles at higher excitation
energies of the compound nucleus. These results show large
discrepencies, which may be understood in terms of second and
third chance fissions taking place at higher excitation
energies. However, if the yield is measured at those
excitation energies where only first chance fissions contribute,
then a clearer picture of the excitation energy dependence of
yield can emerge. For neutron induced fission of ^{235}U, this
neutron energy range is from thermal to about 5 MeV. In a
measurement, Nadkarni and Kapoor [35] determined the light-
charged-particle (LCP) yields in the neutron induced fission
of ^{235}U in the neutron energy region from thermal to 4 MeV
with 1 MeV energy interval. They observed that the yield
remains constant in this neutron energy region. The yields
of tritium and alpha particles from neutron-induced fission

of ^{235}U from thermal to 700 keV region were determined by
Fluss et al. [36] using radiochemical techniques as well as
$\triangle$E-E detector telescope. The tritium yield was found to
increase abruptly for fast neutron fission over thermal value
and observed to be about three times that of thermal neutrons
while alpha particle yield remained constant. In subsequent
measurements at neutron energies of 0.75, 1.25, 1.50 and
1.75 MeV, Nadkarni et al. [37] observed that the yield of light-
charged-particles having energies above 12 MeV showed no
variation with the incident neutron energy while the LCP yield
below energy 12 MeV showed a strong dependence on the neutron
energy. Recently, Krishnarajulu et al. [11] performed
measurements on the fast neutron induced fission of ^{235}U
employing a single semiconductor detector for light-charged-
particle detection in coincidence with fission. These
measurements were made for thermal, 120, 180, 500, 800 and
1020 keV neutron energies. The yield of light-charged-
particles having energies above 12 MeV was found to show an
increase of about 20 % above thermal value in the neutron
energy region around 200 keV while at higher neutron energies
the yield coincided with that of thermal neutrons. This
component of light-charged-particles was attributed to alpha
particles. In the data analysis, it was assumed that the
yield of light-charged-particles having energies above 12 MeV
is due to only alpha particles and therefore the LCP energy

spectra above 12 MeV were least squares fitted to Gaussian shapes. The triton yield was then obtained by deducting the alpha particle Gaussian tail from the total yield of light-charged-particles having energies between 6.5 MeV and 12 MeV. The triton yield showed a continuous increase with incident neutron energy upto 500 keV, at which its value became about 3 times that of thermal neutrons. At neutron energies above 500 keV, the yield showed a decrease tending towards the thermal value. In 1979, Krishnarajulu et al. [12] repeated these measurements for thermal and fast neutron induced fission of ^{239}Pu. The alpha particle yield showed a drop of about 14 % for the neutron energy region from 200 keV to 350 keV as compared to that for thermal neutrons. In the other regions of neutron energy the alpha yield was found to be equal to the thermal yield. The triton yield was found to remain constant upto neutron energy of 500 keV and at neutron energies above 500 keV the triton yield was observed to be below the thermal value.

It is realised that to understand the emission mechanism of light-charged-particles and to see the effect of spin and excitation energy of the compound nucleus on the emission probabilities of different light-charged-particles it is necessary to study the variation of yields, energy distribution parameters and angular distribution parameters of different light-charged-particles from neutron-induced

fission of ^{235}U with incident neutron energy. A multiparameter experiment was performed to study the yields and the energy distribution parameters of protons, tritons and alpha particles from neutron-induced fission of ^{235}U. The measurements were carried out in coincidence with fission fragments at neutron energies; thermal, 150, 180, 230 and 550 keV. For particle identification and proper discrimination of different light-charged-particles, a semiconductor ΔE-E detector telescope was used. The method of particle identification and result of this experiment are described in the following sections.

2.3 Particle Identifier Techniques

The different types of charged particles produced in light-charged-particle accompanied fission can be identified by determining the atomic number (Z) and the mass number (A) associated with it. A complete determination of Z and A requires the measurement of the two quantities excluding the energy which are independent functions of Z and A. For non-relativistic particles, A = M and therefore M and Z need be determined with enough accuracy to separate the adjacent charged particles. Several static as well as on-line techniques have been developed in the past two decades for particle identification. The static techniques, which include radiochemical, photographic and solid state nuclear track detector techniques [38], are of limited use. The on-line

techniques, however, offer an ideal method for unique identification of nuclear charged particles. The semiconductor $\triangle$E-E detector telescope, time-of-flight (TOF) technique and magnetic mass spectrometers are the main on-line method for particle identification.

Since the fractional differences between the adjacent small integers corresponding to M and Z for light particles are large, a semiconductor $\triangle$E-E detector telescope works satisfactorily giving good resolution. For heavy charged particles, the necessary resolution becomes difficult or even impossible to achieve with a detector telescope alone. And therefore, sometimes, all the three (detector telescope, time-of-flight and magnetic mass spectrometers) techniques are combined to achieve necessary resolution for heavy-charged-particles.

A detector telescope consists of a thin transmission ($\triangle$E) detector for providing a direct measure of $\frac{dE}{dx}$ for a particular segment of a particles track and a thick (E) detector to measure residual energy of the particle. The detector thicknesses are so chosen that the particles of interest pass through the front $\triangle$E-detector, providing a $\triangle$E signal, then completely stop in the rear E-detector.

The two types of particle identifiers have been developed in the past making use of $\triangle$E and E signals; the multiplier type of identifier and the power-law type of identifier. The first type of identifier was developed from the simplified version of the Bethe-Block equation. For

non-relativistic light-charged-particles,

$$-\frac{dE}{dx} = a(\frac{MZ^2}{E}) \ln (\frac{bE}{M}) \qquad (2.1)$$

where a and b are constants that depend on the absorber
material. If a detector of thickness $\triangle x$ absorbs a very
small fraction of the incident energy of a particle to produce
a signal proportional to the energy loss $\triangle E$, and a second
detector absorbs the remainder of the energy E to produce a
signal proportional to E then for a broad range of energies
and types of particles the final form of the function used in
multiplier type of identifier is

$$(E + E_o + k \triangle E)\triangle E \propto MZ^2 \triangle x \qquad (2.2)$$

where E_o and k are parameters to be adjusted experimentally
for optimum constancy of the particle identifier output as a
function of energy. For $\triangle E \ll E$, k equals 0.5 to good
approximation.

A major difficulty with the multiplier type of
identifiers is the need for experimental adjustment of
parameters. The use of empirical range-energy relation
provides a better method for particle identification. The
empirical range-energy relation,

$$R = a E^n \qquad (2.3)$$

was used in power-law particle identifier [39], where $a \sim \frac{1}{Z^2}$.

For particles ranging from protons to alpha particles in the energy region from 5 MeV to 50 MeV, the value of n is 1.76 [40]. If a light-charged-particle deposits an amount of energy ΔE in the first detector of thickness Δx of a telescope, then stops in the second detector depositing the remaining energy E, the range of the particle with energy $(E + \Delta E)$ is Δx larger than the range of the same particle with energy (E) and therefore,

$$\frac{\Delta x}{a} = [(E + \Delta E)^n - E^n]$$

or
$$MZ^2 . \Delta x = [(E + \Delta E)^n - E^n] \tag{2.4}$$

Knowing Δx and determining E and ΔE, the value of MZ^2 can be obtained from eqn. (2.4) accurately. Since this method does not involve any arbitrary constants as in the other method (eqn. (2.2)), it has been used in the present study for particle identification.

2.4 Experimental Setup and Details

The experiment was carried out with the 2 MV Van de Graaff accelerator at the Indian Institute of Technology, Kanpur. This machine is capable of providing positive ion beams (protons, deuterons and alpha particles) upto about 100 μA with an energy resolution better than ± 4 keV without any extra stabilization system. Beam spot of size less than

5 mm in diameter was obtained at the target after focussing it with the help of quadrupole lens. Beam current at the target was monitored with a current integrator at the console. The schematic diagram of the beam transport system is shown in Fig. 2.1 along with the ionization chamber and the neutron counter assemblies.

2.4.1 Neutron Target Holder

Fig. 2.2 shows the neutron target holder assembly. It consists of a water cooled collimator and a target holder made of copper. The target was cooled by flowing chilled water through a copper tube wrapped around the target holder and around the collimator tube. With this assembly it was possible to use proton currents upto 50 µA at 2 MeV energy on the target without significant target deterioration for periods over 24 hours. The nuclear reactions, $^7Li(p,n)^7Be$ and $^3H(p,n)^3He$, were used for neutron flux production. The lithium targets of about 10 keV thickness at proton energy of 2 MeV were prepared by vacuum evaporation of lithium metal on the copper backings. A lithium target on the aluminium backing, prepared simultaneously with the other targets on the copper backings, was used to determine the lithium target thickness accurately by measuring the shifts in the various aluminium resonances. Tritium targets were used for the production of higher energy neutrons. The
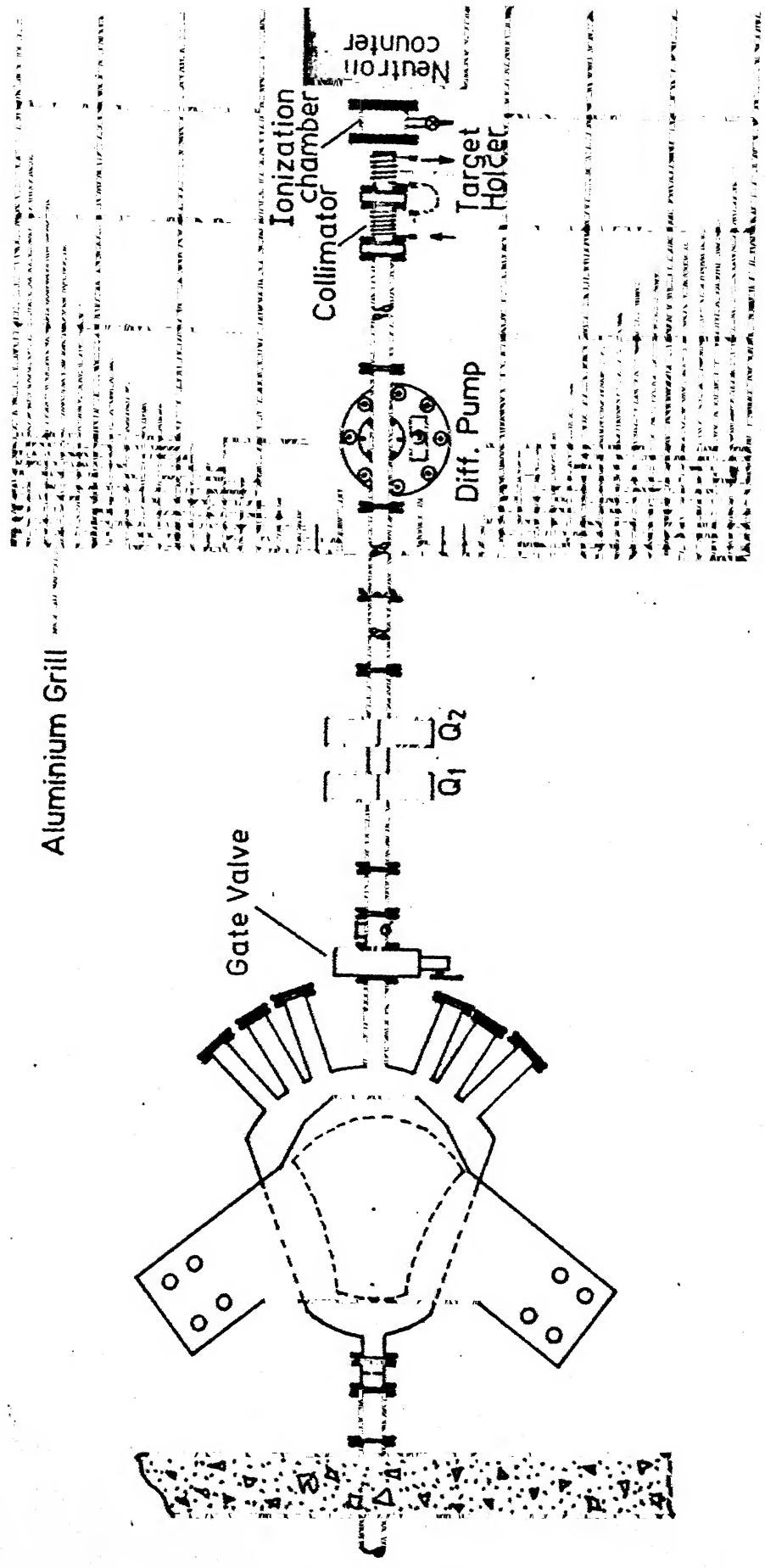
Fig. 2.1. Schematic diagram of experimental setup.
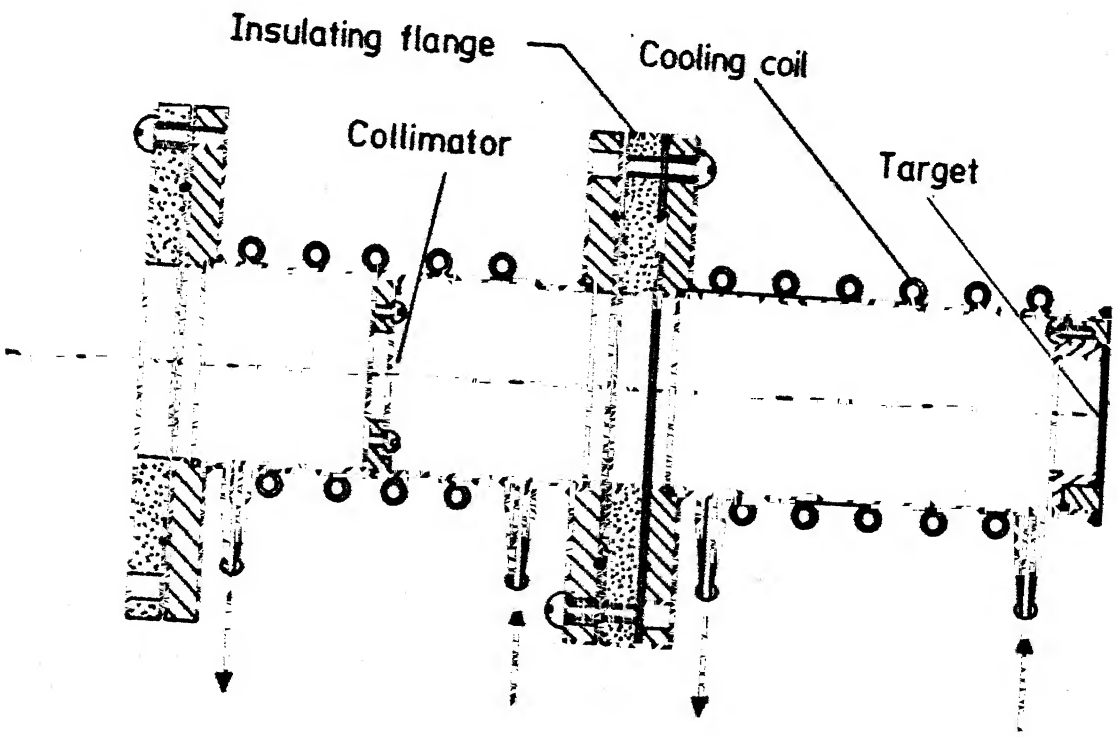
Fig. 2.2. The neutron target holder and collimator.

tritium targets were obtained from the Isotope Division, Bhabha Atomic Research Centre, Bombay. The targets of activities upto 8 Ci were used in the present experiment. These targets consisted of titanium deposited on a copper disc in which tritium was adsorbed such that the ratio of number of atoms of tritium to that of titanium was 1:1. The thickness of these targets in keV were determined as follows:

For a tritium target of activity A (Ci)

$$\frac{dN}{dt} = -\lambda N = A \ (Ci)$$

or $$\lambda N = 3.7 \times 10^{10} \ A \ disintegrations/sec.$$

Thus the number of tritium and titanium atoms in the targets of activity A Ci is

$$N = 3.7 \times 10^{10} \times \frac{12.33 \times 3.15 \times 10^{7}}{0.693} A = 2.07 \times 10^{19} \ A$$

The titanium is deposited over an area of diameter 2 cm. Thus the thickness of the titanium layer would be

$$= \frac{2.07 \times 10^{19}}{6 \times 10^{23}} \times \frac{48}{\pi} A = 0.523 \ A \ mg/cm^2$$

As the mass number of titanium (48) is very large compared to that of tritium (3), the protons lose most of their energy in titanium and hence using the energy loss rate of protons in the titanium in units of $MeV/mg/cm^2$, the net loss for any target of specified activity may be

calculated. The energy loss of protons in the titanium in units of $MeV/mg/cm^2$ can be obtained from tables [41]. As an example; for protons of energy 2 MeV in a target of 8 Ci, the energy loss would be 155 keV and therefore the target thickness of a 8 Ci target to 2 MeV protons is about 155 keV.

A long counter was used to monitor the neutron flux and the neutron target deterioration. It consisted of a BF_3 counter axially embeded in a paraffin cylinder and was placed at a distance of about two meters away from the neutron target holder. The response of this counter for thermal neutrons is about 70 % of the response to 1 MeV neutrons [42]. For neutrons of energy above 1 MeV, the counter has flat response.

2.4.2 Detector Assembly

A schematic diagram of the detector assembly is shown in Fig. 2.3. It consisted of three parts; an ionization chamber filled with argon gas, $\triangle$E-detector and E-detector. A 5 mg/cm^2 ^{235}U (93.9 % enrichment) source was used in the measurement. It was over an area of 4 cm^2 on a nickel backing. This source formed the cathode of the ionization chamber. An aluminium foil (of thickness $\sim$7 mg/cm^2) was placed at a distance of about 2 mm from the fissile source which served as the collector of the ionization chamber used to detect the fission fragments. The chamber was filled
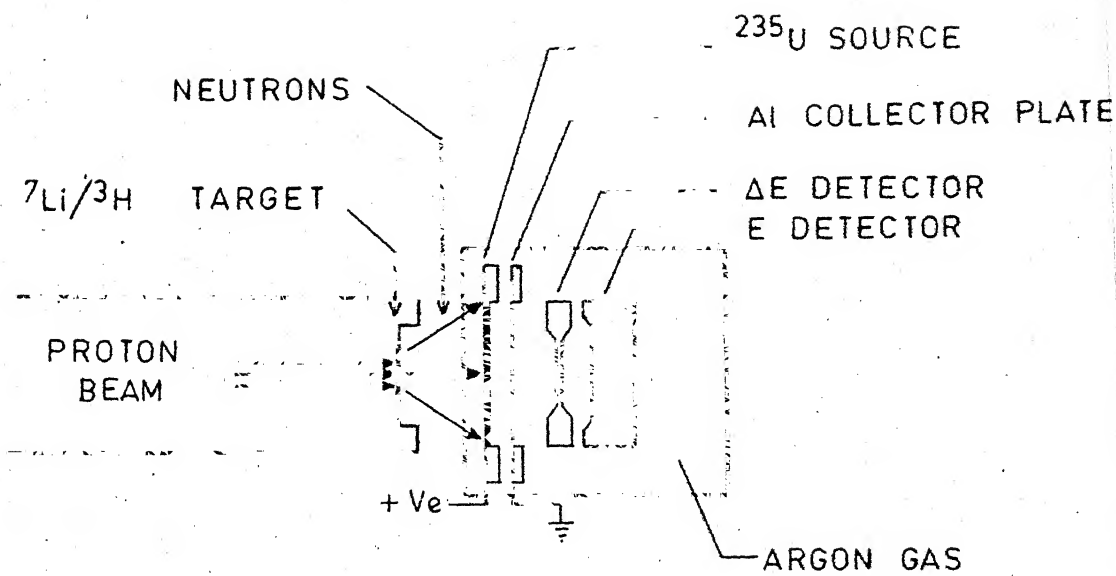
Fig. 2.3. Schematic diagram of the detector assembly.

with a high purity argon gas to a pressure of about one atmosphere. The voltage on the collector was adjusted to give suitable fission pulses. The natural alpha particles and the fission fragments were stopped by the aluminium foil (collector foil) allowing only the light-charged-particles to pass through to the semiconductor ΔE-E detector telescope mounted close to the collector foil. The ΔE-detector was a standard semiconductor $\frac{dE}{dx}$ detector obtained from ORTEC. It had a thickness of about 64 microns. The E-detectors were standard silicon surface barrier detectors of 2 cm diameter and a depletion depth of 600 microns. These detectors had an energy resolution of about 100 keV for 5.47 MeV ^{241}Am alpha particles. The total thickness of ΔE- and E-detector was sufficient ($\backsim$670 microns) to absorb tritons of energy 16 MeV and protons of energy 11 MeV. Two pulsers, one for ΔE-channel and the other in E-channel, were calibrated in terms of the known energy outputs of ΔE- and E-detectors using low intensity alpha source of ^{241}Am and ^{227}Np. These pulses were used for on-line calibration of the two detectors.

2.4.3 Electronic Arrangement

Fig. 2.4 shows the block diagram of the electronic system used in the experiment. The pulses from ΔE- and E-detectors were amplified and fed to the timing single channel analysers to get the timing signals. The timing
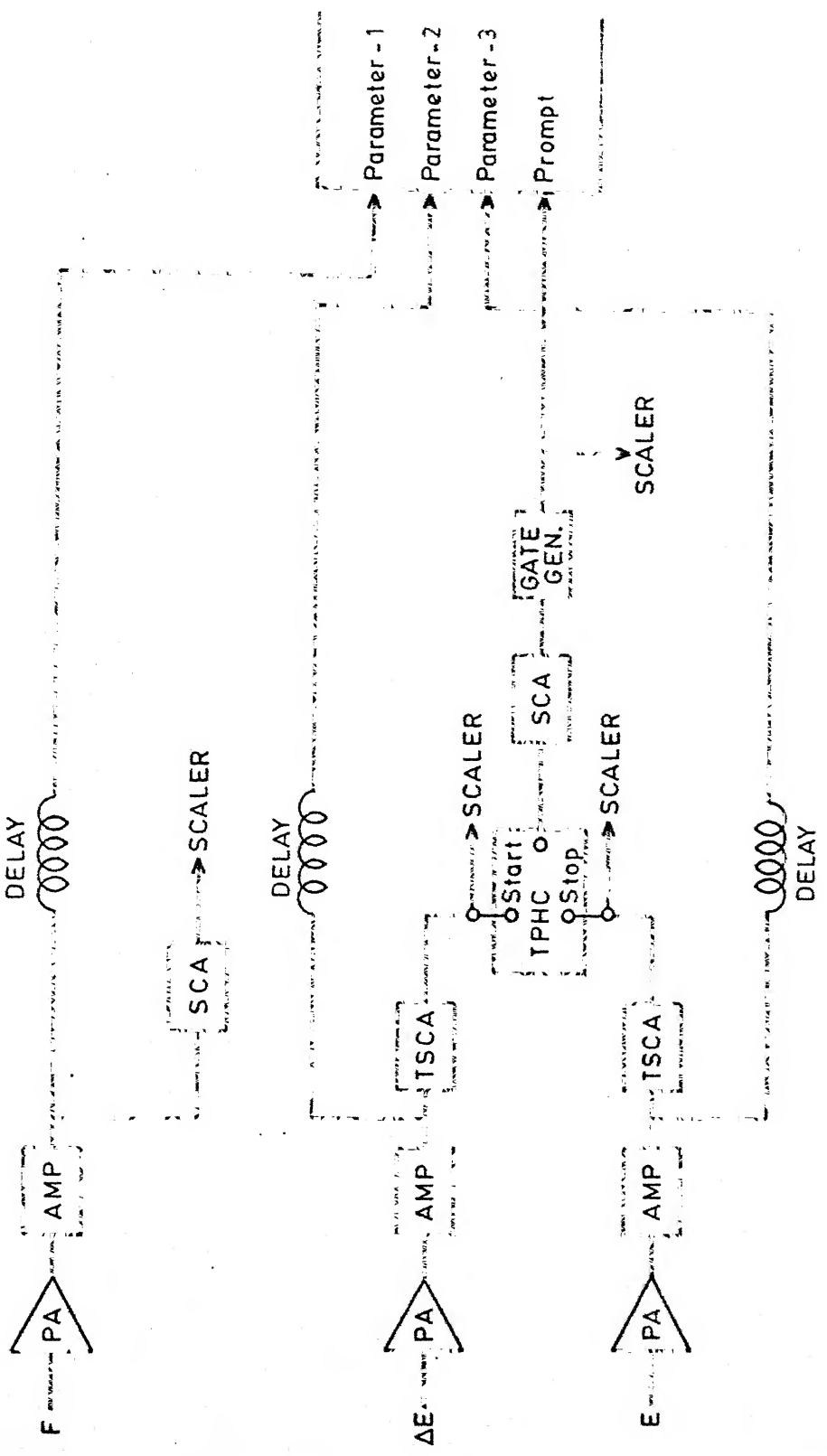
Fig. 2.4. Block diagram of the electronic system used in the experiment.

signals were fed to a time-to-pulse-height converter, the
output of which was shaped and fed to the prompt input of
the three parameter data acquisition system. The time
resolution (2τ) was chosen to be about 1.0 µsec. The
ionization chamber pulses were also amplified and sent to
one of the ADC's of the three parameter system. The three
amplified pulses, from ionization chamber, ΔE- and E-detectors,
were then recorded in coincidence mode onto a magnetic tape
with the help of a three parameter data acquisition system.
The fission and the light-charged-particle count rates were
simultaneously monitored. The discriminator on the fission side
was set to cut off the natural alphas (~ 6 MeV). The details
of the three parameter data acquisition system is given in the
next section.

2.5 Three Parameter Data Acquisition System

Multiparameter systems play an important role in the
studies of correlations between two or more parameters of the
nuclear origin. These multiparameter systems may have an
on-line computation facility. In the absence of an on-line
facility, the digitised information can be recorded on a
computer compatible magnetic tape. In the present experiment
we have used a three parameter data acquisition system to
process the analog pulses from the three detectors and the
digitised data were recorded on a computer compatible

magnetic tape. Main features of the system are described briefly in the following.

The three parameter data acquisition system consists of three identical data acquisition systems, each made up of an Analog-to-Digital Converter (ADC) and a set of decade scalers for temporary storage. The three ADC's can be used independently or programmed for operation under different sets of condition. Each ADC is capable of digitizing the information in 1000 channels. Each pulse is processed by ADC only if it satisfies certain amplitude and timing conditions. The amplitude conditions are set by the three potentiometers connected with each ADC, namely, the threshold potentiometer to set the 'zero' of the ADC, the sensitivity potentiometer to set the minimum acceptable level and to set the upper maximum acceptable level, an upper level potentiometer. The timing conditions are set by providing appropriate coincidence signals. When each of the three ADC's has stored a channel number (temporarily) on its scalers a common transfer command is generated. This command scans each scaler and transfers the addresses serially to the magnetic tape recording unit. This command also multiplexes the serial output with special information bits. The combined multiplexed information (serial output and special bits) is called one 'Word'. In our case, one word consists of twelve bits (or characters) i.e. three bits from each parameter corresponding to a

channel number (000 to 999) and three special character bits. The serial converter produces a pulse called digit pulse for every character in the word. These digit pulses are also transferred in sequence along with the characters in the word for monitoring the data. The sequence of the characters and corresponding digit pulses are shown in Fig. 2.5. Besides digit pulses, the serial converter gives out a pulse, known as the word pulse for each word at the instant of a scan command. When a complete word is transferred to the magnetic tape recorder (MTR), the three parameter system (3 PS) becomes ready to process another set of pulses.

An interface is used to connect the 3 PS with the MTR. It has various circuits to generate different functions. The digit line circuit generates a signal to produce movement of the magnetic tape and a step command necessary for writing the data on the tape. The word counting circuit counts the word pulses from 3 PS and generates a signal at the end of each record which is counted by record counter. The number of words in a record can be fixed manually at 32, 64,128 or 256. After each record the word counter gets reset automatically. The recording of data on the tape is in the Binary-Coded-Decimal (BCD) format. The MTR generates the parity bit necessary to make the vertical parity of each character even. This parity bit is recorded along with the character and checked. In checking, the vertical parity is
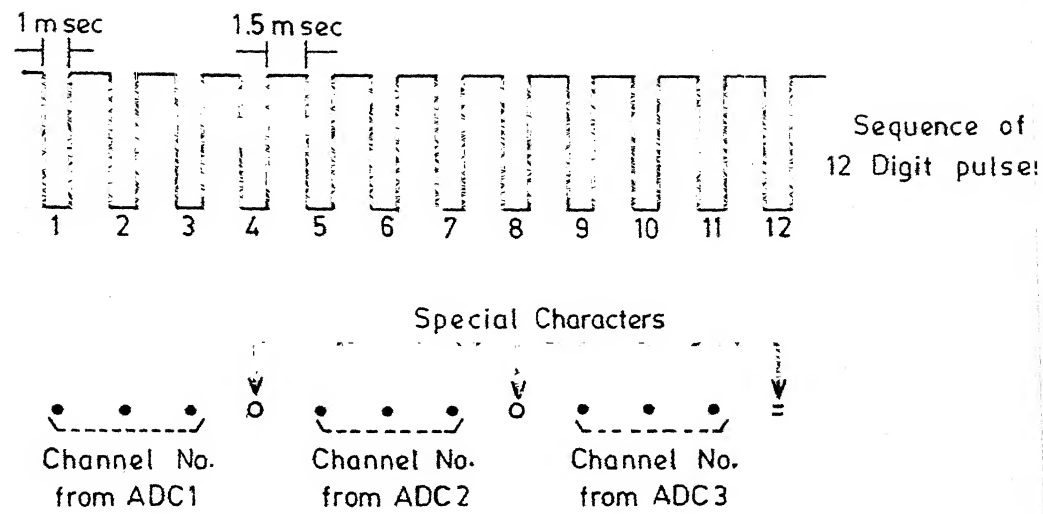
Fig. 2.5. Sequence of characters in each word recorded on the magnetic tape.

again generated from the recorded character and compared with the previously generated vertical parity. In the event of mis-match in these two vertical parity bits, the MTR generates a parity error signal. To monitor parity error signals the interface is provided with a Parity Error Counter circuit. Interface also generates beginning of tape (BOT), end of file (EOF), system reset and read/write command signals. The speed of serial transfer of digits from the 3 PS to the MTR is governed by a speed control circuit in the interface. The speed can be varied upto 600 characters per sec.

The MTR records and consequently stores the digital data on a magnetic tape. There are three packing densities 200, 556 and 800 BPI (bits per inch) available for writing and two packing densities 200 and 556 BPI available for reading. In the present experiment, the recording was done in the BCD format at 200 BPI.

2.6 Experimental Procedure

The pulses from ionization chamber, ΔE- and E-detectors were recorded onto a magnetic tape with the help of the three parameter data acquisition system described above. The detector assembly was placed very close to the neutron target holder. Neutrons of energies 120 keV and 180 keV were produced from $^7Li(p,n)^7Be$ reaction [43] and neutrons of energies 230 keV and 550 keV were obtained from $^3H(p,n)^3He$

reaction [44]. The spread in the neutron energy was calculated using the energy loss and angular spread considerations. The ^{235}U target intercepted the neutron beam in a cone of angle of 30°. The energy spread, thus estimated, for 120 keV and 180 keV was about $\pm$ 20 keV and that for 230 keV and 550 keV was about $\pm$ 90 keV. For the production of thermal neutrons, a thick paraffin block (thickness ∿5 cm) was placed between the neutron target holder and the fission chamber. The total of eight 'fast' runs, two for each of the four neutron energies, were taken. Each 'fast' run was preceded and followed by a thermal run. These thermal runs served as a monitor for possible drifts and also provided a normalization for the fast runs. The stability of the system was monitored frequently using on-line precision pulsers for Δ E- and E-detector channels. Because of the neutron damage the detector leakage current increases which reduces the bias on the detector since the voltage drop across the series resistance in the preamplifier increases. The reduction in the detector bias reduces the depletion depth of the E-detector hence resulting in the loss of high energy light-charged-particles. Therefore, the leakage current in the E-detector was continuously monitored and the bias was appropriately adjusted. When the leakage current become excessive detector was changed. The neutron target was also replaced when the neutron flux reduced after a long use. The average proton current used was about 30 μA

giving neutron flux of $\sim 10^7$ neutrons/cm^2/sec. The fission rate was about 1.5×10^3 per sec. The average light-charged-particle count rate was about 150-200 per hour. Each 'fast' as well as 'thermal' run consisted of about 5×10^7 fissions.

2.7 Data Analysis

The three parameters recorded were : fission, $\triangle E$- and E-detector pulses respectively. The data were analysed off-line on IBM-1800 and DEC-10 systems.

Although the coincidence between $\triangle E$- and E-detector pulses used in the present experiment was necessary for detecting the light-charged-particles of fission origin in the semiconductor $\triangle E$-E detector telescope but this coincidence condition did not prevent recording of some light-charged-particles of non-fission origin. The light-charged-particles in coincidence with fission were analysed by eliminating all the events of non-fission origin as described below.

2.7.1 Noise Elimination

The determination of absolute energies of $\triangle E$- and E-detector pulses for each event was carried out as follows:

$$\triangle E \;=\; A_2 X_2 + B_2,$$

$$E \;=\; A_3 X_3 + B_3$$

where X_2 and X_3 are the channel numbers of second and third parameters respectively. A_2, B_2 and A_3, B_3 are the calibration constants for $\triangle E$- and E- channels respectively. The calibration constants were determined using the channel numbers corresponding to the peak positions of the known energy alpha particles from the standard sources of ^{241}Am and ^{227}Np. The absolute energies of $\triangle E$ and E for each event were then used to obtain the particle identifier spectrum using the expression,

$$PI \;=\; (E + \triangle E)^{1.76} - E^{1.76} \tag{2.5}$$

A typical particle identifier spectrum for one of the thermal runs is shown in Fig. 2.6. The spectrum consists of three well separated peaks besides the low energy peaking due to noise. Using the thickness of the $\triangle E$-detector and the known energy distributions for protons, tritons and alpha particles from the thermal neutron induced fission of ^{235}U [22], a calculation was carried out to determine the expected regions for these particles in the particle identifier spectrum. The expected regions of protons, tritons and alpha particles are also indicated in the Fig. 2.6 by double-headed-horizontal bars. The region below channel number five was attributed to the noise in the particle identifier spectrum and therefore the events above this channel number were analysed to study the various correlations. The compressed typical spectra for fission channel, $\triangle E$-channel and E-channel
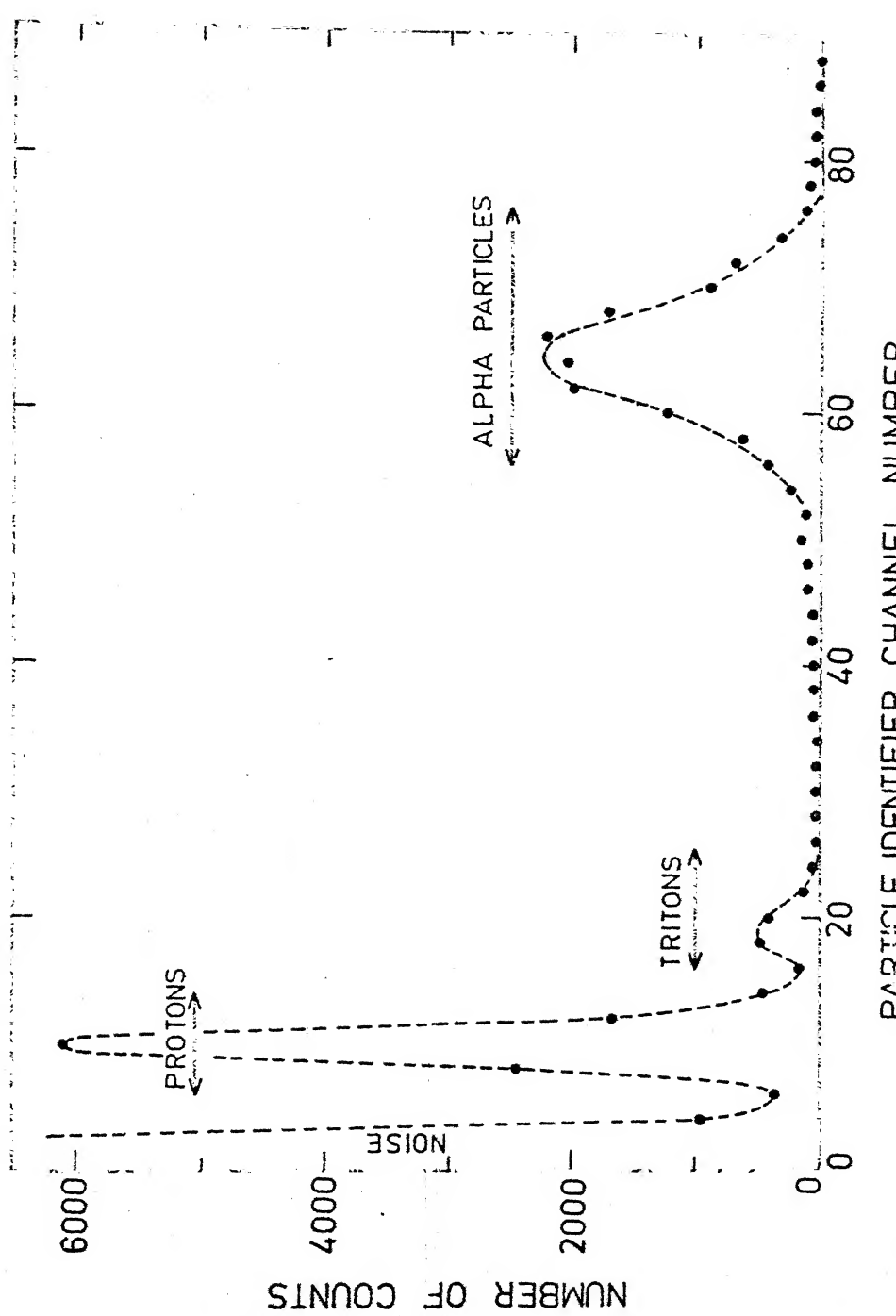
Fig. 2.6. A typical particle identifier spectrum.

for the above thermal run after eliminating the noise are
shown in Fig. 2.7. Similar spectra for all the fast as well
as thermal runs were obtained to check the overall consistency
of the recording system.

2.7.2   Elimination of Events of Non-fission Origin

The light-charged-particles of non-fission origin
could be due to (n,p), (n,α), (α,p) etc. nuclear reactions
with the various elements present in the detector assembly
chamber. These could be eliminated by forcing a coincidence
with fission pulses of above a certain amplitude. The fission
spectra were used to eliminate the light-charged-particles
(events) of non-fission origin from the various neutron energy
runs. Keeping various biases in the fission channel, the
particle identifier spectra were obtained. Fig. 2.8 shows a
typical particle identifier spectrum for a thermal run without
and with bias corresponding to channel 90 in the fission
spectrum. The areas under different peaks in the particle
identifier spectrum give the yields of the three particles
separately. The ratio of triton to alpha and proton to alpha
particle yields thus were determined at various biases in
the fission channel for all the fast and thermal neutron runs.
These ratios for a typical thermal run are listed in the
Table – 2.2 and are shown in Fig. 2.9.[*]

[*] Fig. 2.7a is a compressed fission spectrum. Fig. 2.9 has been obtained
from uncompressed fission spectrum containing total channels 999.
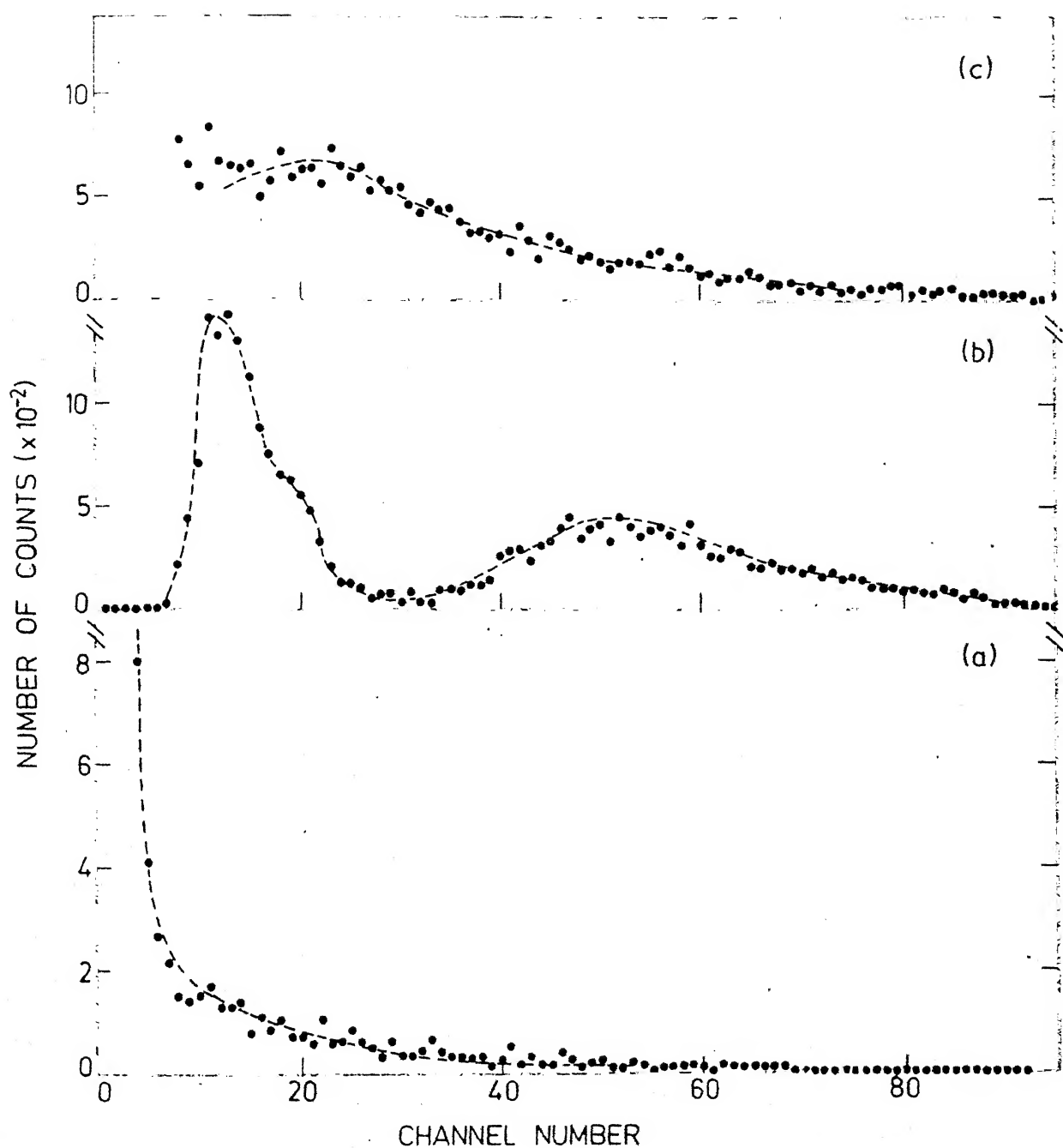
Fig. 2.7. (a) Fission spectrum (b) ΔE-spectrum and (c) E-spectrum.
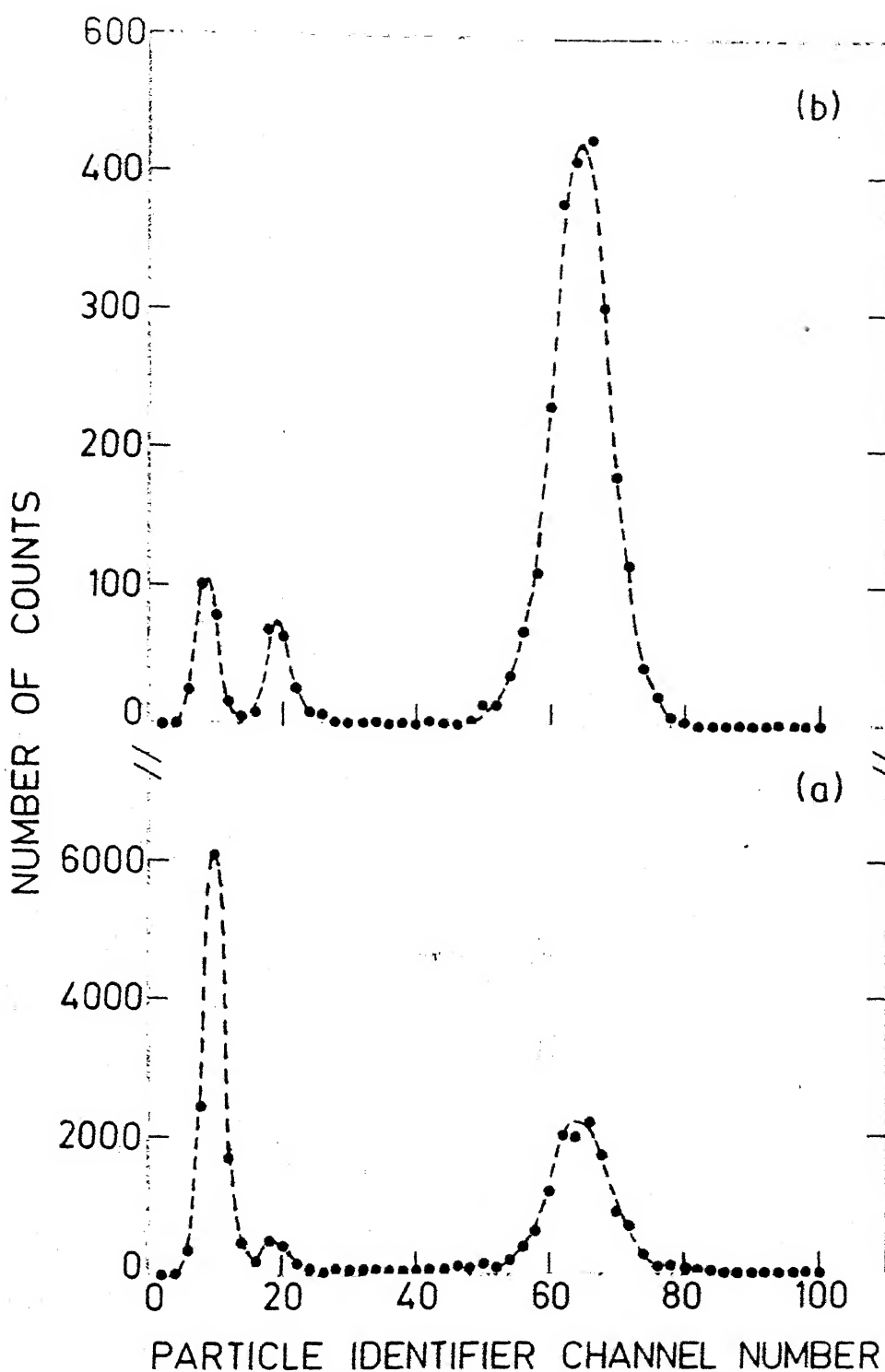
Fig. 2.8. Typical particle identifier spectra for a thermal run (a) without any fission bias and (b) with fission bias at channel number 90.

Table – 2.2   Ratios of the yields of tritons and protons to
alpha particle yield for various biases in the
fission channel for a thermal neutron induced
fission run.

Fission Bias (channel no.)	Triton to Alpha Particle Yield	Proton to Alpha Particle Yield
0	0.131 ± 0.004	0.970 ± 0.012
10	0.131 ± 0.004	0.970 ± 0.012
20	0.131 ± 0.004	0.970 ± 0.012
30	0.131 ± 0.004	0.970 ± 0.012
40	0.131 ± 0.004	0.970 ± 0.012
50	0.100 ± 0.007	0.580 ± 0.012
60	0.090 ± 0.007	0.510 ± 0.010
70	0.086 ± 0.006	0.180 ± 0.009
80	0.075 ± 0.006	0.120 ± 0.008
90	0.070 ± 0.006	0.092 ± 0.007
100	0.070 ± 0.006	0.092 ± 0.007
110	0.073 ± 0.007	0.090 ± 0.007
120	0.073 ± 0.007	0.095 ± 0.007
130	0.070 ± 0.007	0.094 ± 0.008
140	0.067 ± 0.007	0.093 ± 0.008
150	0.068 ± 0.007	0.090 ± 0.008
160	0.072 ± 0.007	0.099 ± 0.009
170	0.070 ± 0.007	0.092 ± 0.009
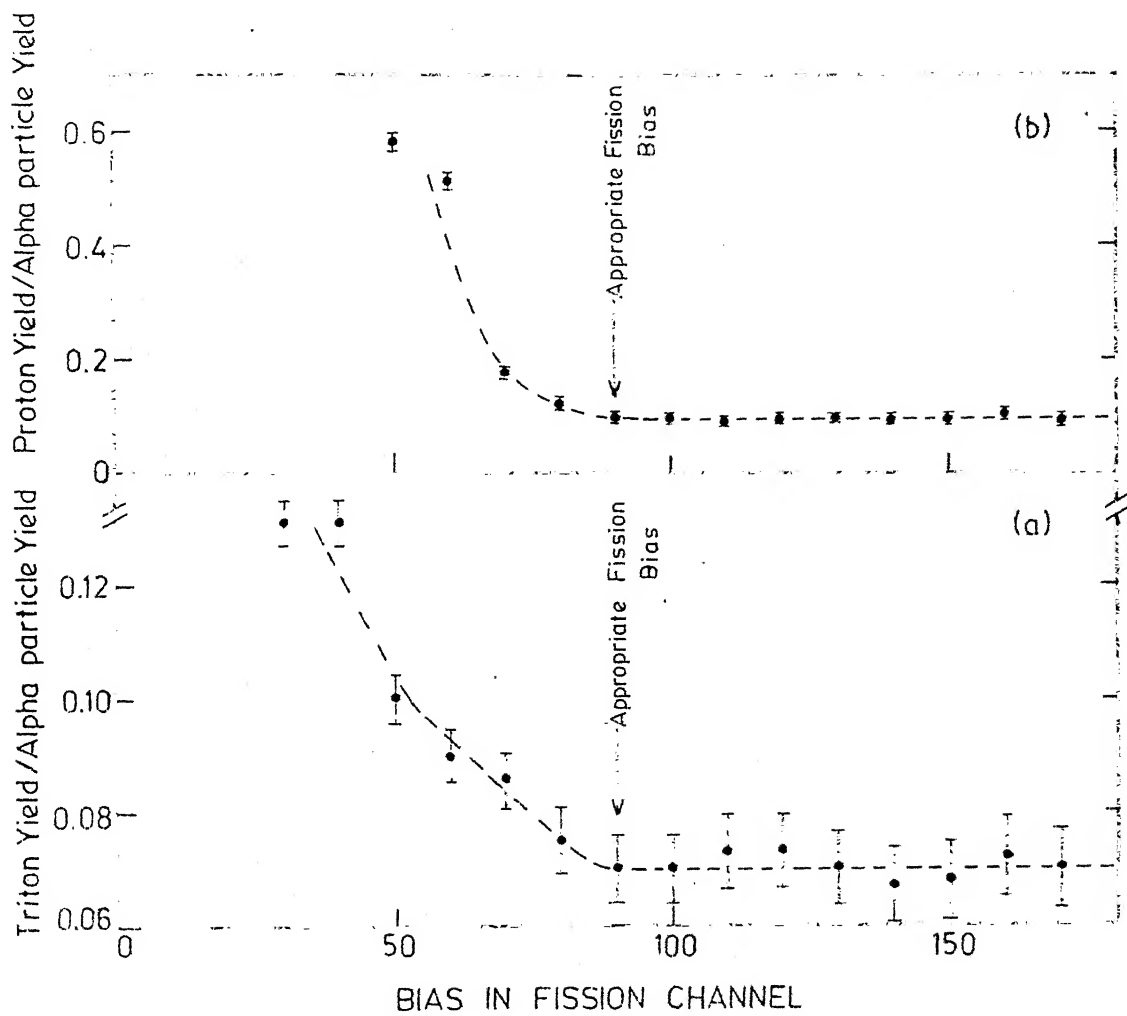
Fig. 2.9. The plot of the ratios (a) triton yield to alpha particle yield and (b) proton yield to alpha particle yield as functions of fission channel bias for a thermal run.

To eliminate the light-charged-particles originating from the non-fission events, a certain bias (at 90) in the fission channel was incorporated which was chosen such that beyond this the ratio of triton to alpha and proton to alpha particle yields remained constant within the statistical errors for each run. The constancy of ratios for higher fission biases indicates that the region of the fission spectrum above channel 90 is due to only the genuine fission events while the lower region of the fission spectrum contains a mixture of the events of fission and non-fission origin.

2.7.3 Energy-Loss Correction

The energy distributions of protons, tritons and alpha particles for various neutron energy runs were obtained using the particle identifier spectra after eliminating the particles of non-fission origin. These distributions correspond to different peaks in the particle identifier spectra assigned due to protons, tritons and alpha particles and were corrected for the energy losses in the argon gas of the chamber and aluminium collector foil using the tables of Northcliff and Schilling [41]. The energy loss correction was carried out in the following manner.

Since the exact thickness for energy loss correction was not known, the equivalent thickness of aluminium was

determined by ensuring that the observed most probable energy
of alpha particles in one of the thermal neutron runs comes
at the known value [35] of 15 MeV. The estimated equivalent
thickness of aluminium was found to be = 8.4 mg/cm^2 which was
used to determine the initial energies of the particles from
the residual energies. The curves for obtaining the initial
energies from the residual energies for protons, tritons and
alpha particles for above mentioned equivalent thickness are
shown in Fig. 2.10. Fig. 2.11 shows the uncorrected and
corrected energy spectra for the three light-charged-particles
in a typical thermal run.

2.7.4 Total Yields Determination

From Fig. 2.11, it is clear that the corrected energy
spectra for protons, tritons and alpha particles have energy
cut offs at 3.5 MeV, 6.5 MeV and 11.5 MeV respectively. The
yields, determined from the particle identifier spectra were
therefore the partial yields of these light-charged-particles.

The total yields (extrapolated yields) of these
light-charged-particles were determined using the energy
distribution parameters obtained by least squares fitting
to the Gaussian shapes in the following expression

$$Y_{Total} = \sqrt{2\pi} . \sigma . H \tag{2.6}$$

where σ is the standard deviation and H is the peak height
of the Gaussian distribution.
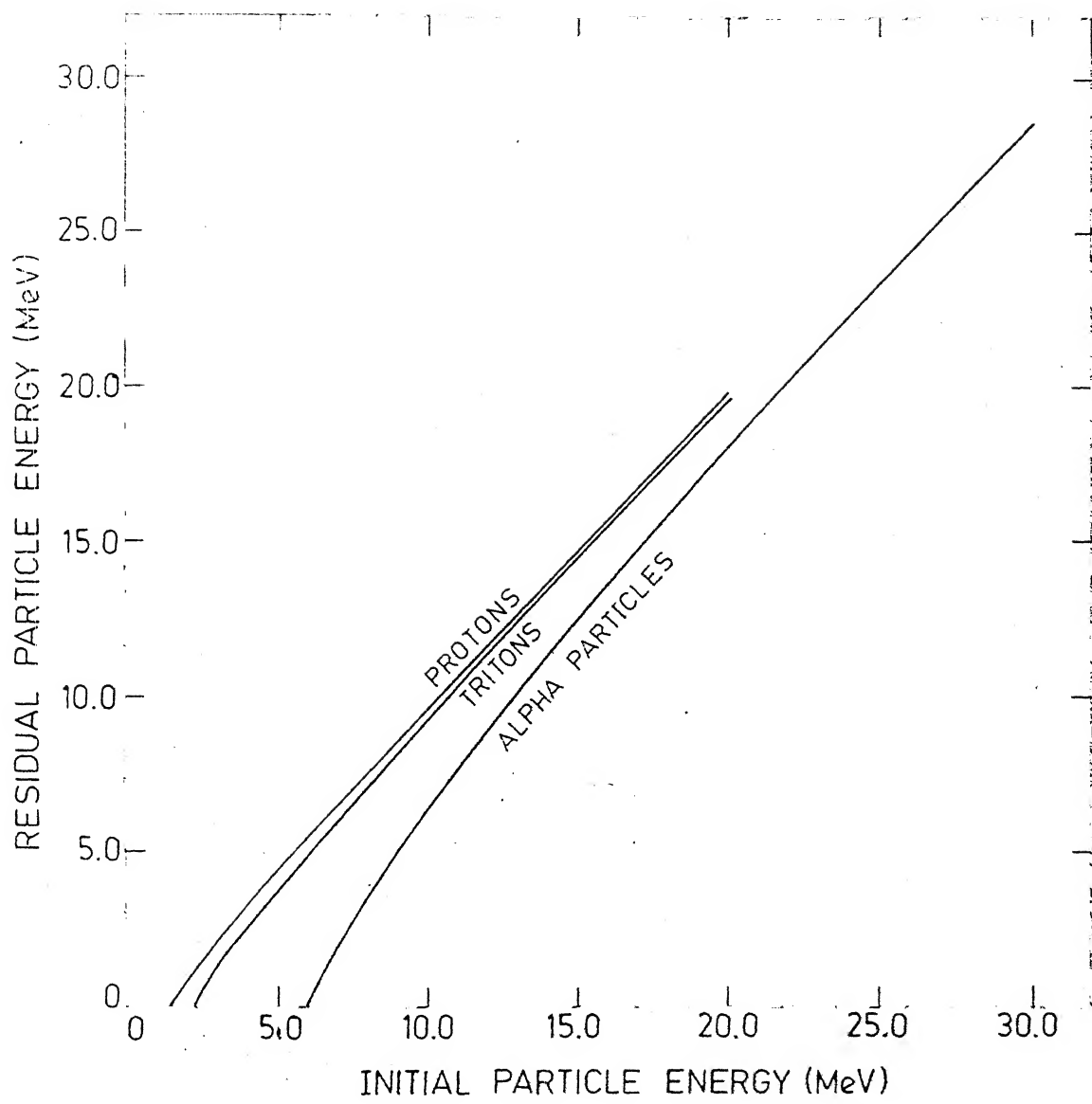
Fig. 2.10. Residual particle energy as a function of initial particle energy for equivalent thickness of aluminium (~8.4 mg/cm²) for alpha particles, tritons and protons.
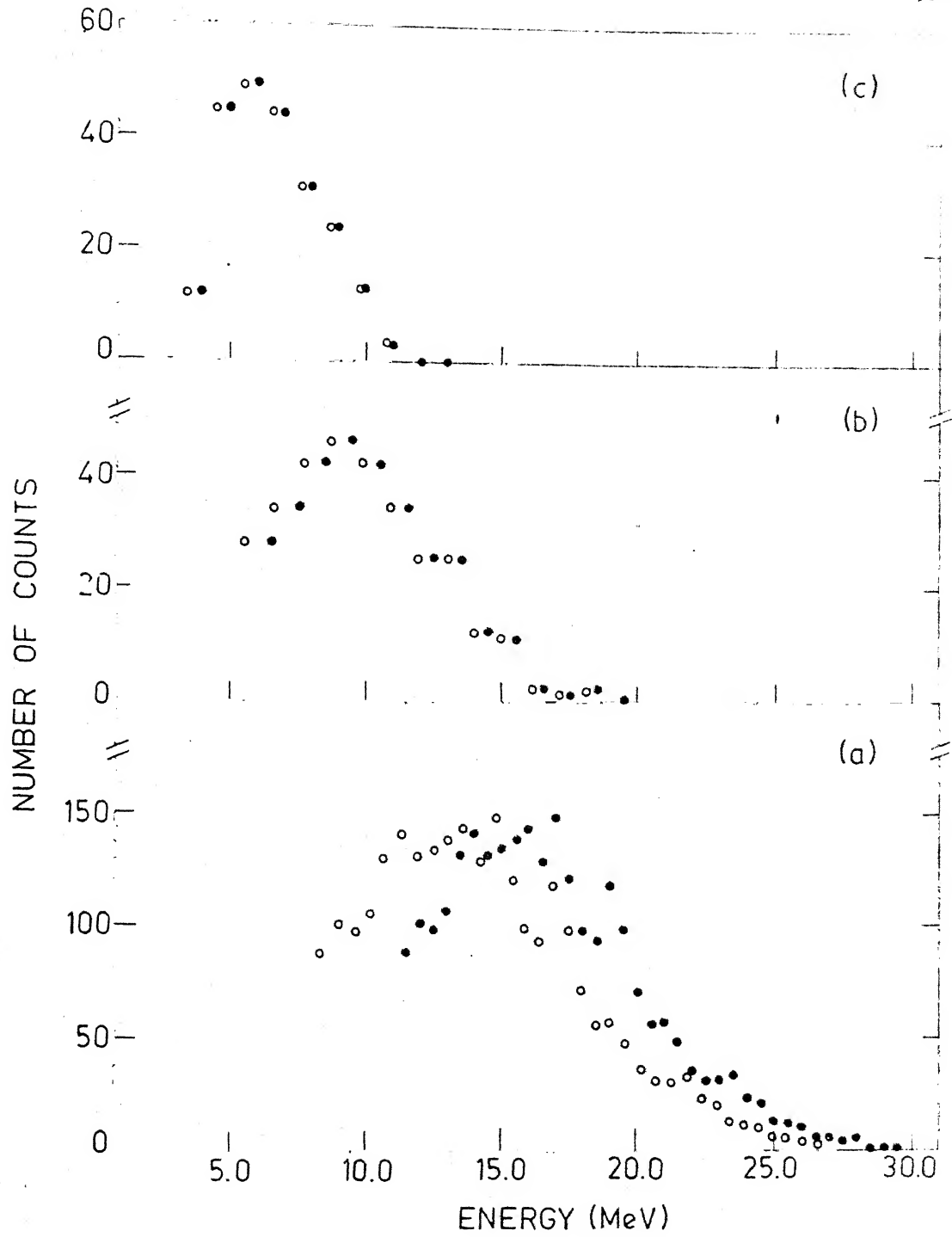
Fig. 2.11. The uncorrected (○) and corrected (●) energy spectra for the three light-charged-particles in a thermal run (a) Alpha particle, (b) triton and (c) proton energy spectra

2.8 Results and Discussion

The particle identifier (PI) spectra, for the thermal neutron induced fission run and for the fast neutron induced fission runs are shown in Fig. 2.12. Each spectrum consists of three well separated peaks. The peaks corresponding to protons, tritons and alpha particles were identified by carrying out a Monte Carlo calculation for the present geometrical configuration of the source detector assembly and using the known energy spectra [22] of these particles in the thermal neutron induced fission. The observed broadening of the peaks in the PI spectra is mainly due to the dispersion in the track lengths traversed by the particles in the ΔE detector in the compact geometry employed in the present experiment. The yields and energy spectra of different light-charged-particles were obtained by taking the events corresponding to the different peaks in the particle identifier spectra. The results on the yields and energy distribution parameters of different light-charged-particles in the thermal runs taken at different times are presented and discussed first. The average values and the maximum uncertainties in their determination were determined. The results on the yields and energy spectra of different particles for various incident neutron energies are then presented.
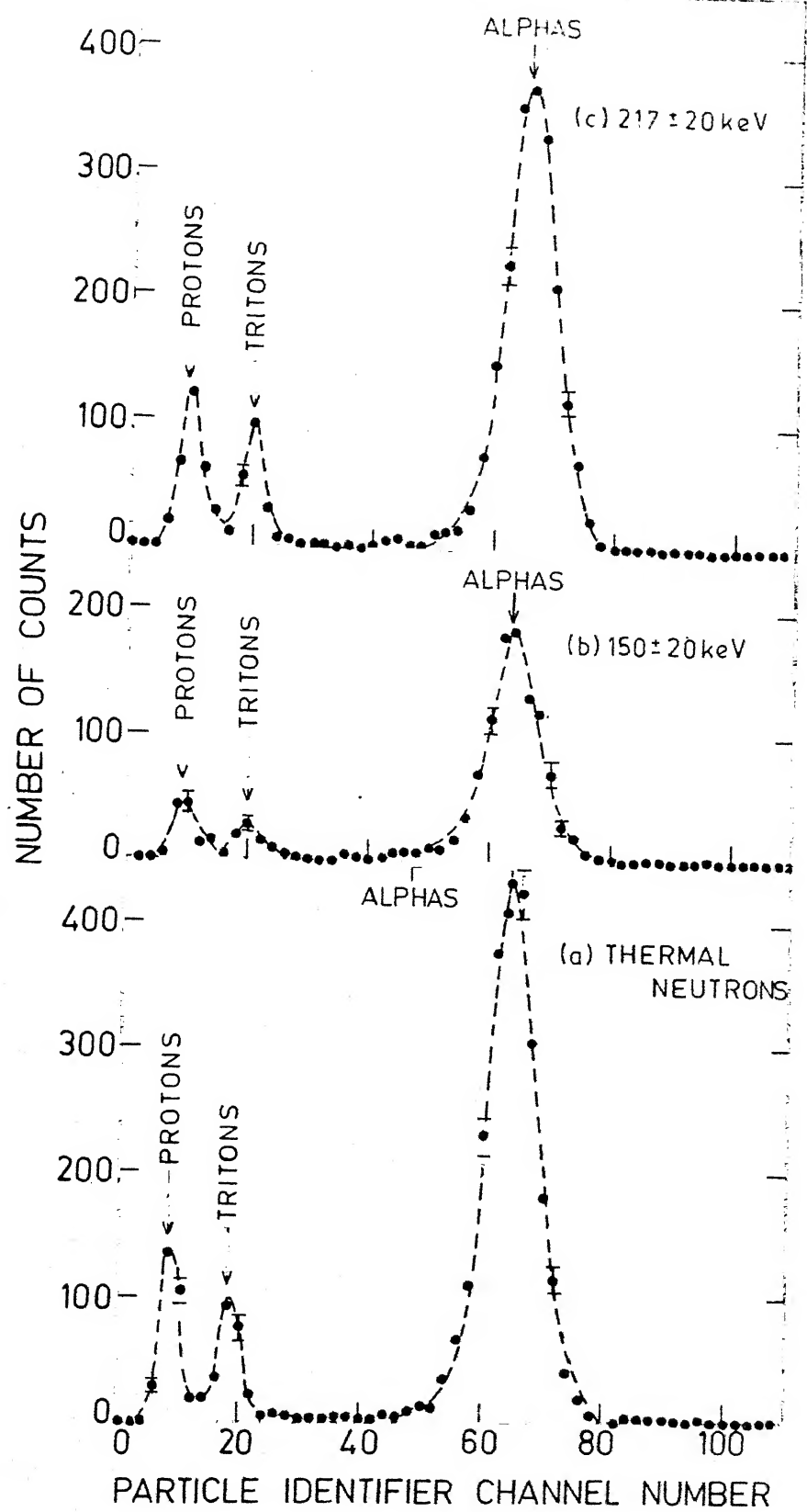
Fig. 2.12. Particle identifier spectra for various incident neutron energies.
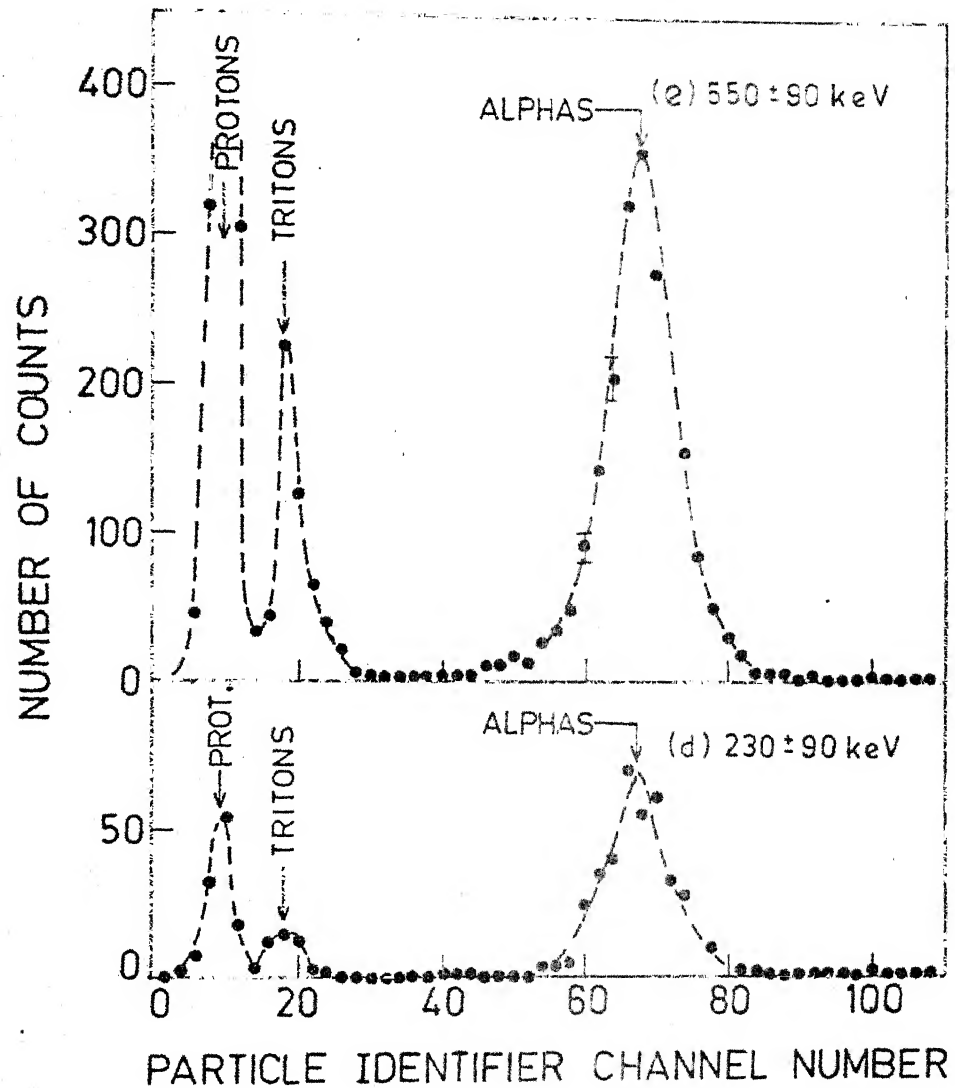
Fig. 2.12.(contd.) Partcle identifier spectra for various
incident neutron energies.

2.8.1 Thermal Yields and Energy Distribution Parameters

The analysis of the various thermal runs taken at different times was carried out as described in the section 2.8. The results thus obtained in the three typical thermal neutron energy runs are presented and discussed here.

The yields of alpha particles, tritons and protons for the three thermal runs are listed in the Table - 2.3 after normalising the observed alpha particle yield for one of the thermal neutron runs to the known [10] absolute value of 2×10^{-3} per fission and then normalising other runs with respect to the normalised run. The yields of tritons and protons per hundred alpha particles are given in the fourth and fifth columns respectively. The average yield of tritons relative to that of alpha particles is found to be 6.78 ± 0.82 percent which is in agreement with the earlier studies [22]. The average yield of protons is seen to be 9.35 ± 0.76 percent of that of alpha particles which is significantly larger than the reported values in most of the earlier measurements [22, 24]. Since the present results were obtained with fission coincidence, the observed higher yield of protons can not be due to any (n,p) reactions caused by the incident neutrons in the materials present inside the detector assembly. The contribution to protons due to fission neutrons was estimated to be negligible. The reason for such higher yield of protons obtained in the present measurement will be discussed

Table - 2.3   Yields of alpha particles, tritons and protons in the three thermal
neutron induced fission runs taken at different times.

Run Number	Yield (per fission)			Relative yield (per 100 alpha particles)	
	Alpha Particles	Tritons	Protons	Tritons	Protons
1	$(2.00\pm0.04)\times10^{-3}$	$(1.40\pm0.10)\times10^{-4}$	$(1.84\pm0.12)\times10^{-4}$	7.04 ± 0.56	9.25 ± 0.66
2	$(2.02\pm0.04)\times10^{-3}$	$(1.30\pm0.09)\times10^{-4}$	$(1.88\pm0.11)\times10^{-4}$	6.44 ± 0.48	9.32 ± 0.58
3	$(1.99\pm0.04)\times10^{-3}$	$(1.30\pm0.10)\times10^{-4}$	$(1.88\pm0.12)\times10^{-4}$	6.58 ± 0.52	9.47 ± 0.64
MEAN	$(2.005\pm0.055)\times10^{-3}$	$(1.35\pm0.15)\times10^{-4}$	$(1.86\pm0.14)\times10^{-4}$	6.73 ± 0.82	9.35 ± 0.76

later.

The most probable energies ($\bar{E}$) and the standard deviations (σ_E) for alpha particles, tritons and protons were obtained by least squares fitting to the Gaussian shapes of the energy spectra and are listed in Table - 2.4. The mean most probable energies and the mean standard deviations with the maximum uncertainties in their determination in the present experiment are also listed in the Table - 2.4. The most probable energy of tritons is found to be about 8.65 MeV, which compares well with the earlier measured values [22] for thermal neutron induced fission of ^{235}U. However, $\bar{E}_p$ is a little lower than the earlier reported values [22] of 8.2 MeV. This is because the depletion depth of the detectors used was enough to absorb only about 11 MeV protons.

The maximum deviations in the values of the yields and the energy distribution parameters in the thermal neutron runs, which represent the uncertainties in their determination in the present experiment, are indicated in all the following figures by means of hatched areas.

2.8.2 Alpha Particles

The energy distributions of alpha particles in the thermal and the various fast neutron induced fission runs are shown in Fig. 2.13. The low-energy cut-off in the energy spectra is due to the energy loss of alpha particles in the

Table - 2.4 The most probable energies ($\bar{E}$) and the standard deviations (σ_E) for alpha particles, tritons and protons in the three thermal neutron runs taken at different times.

Run Number	Alpha particles		Tritons		Protons	
	Most probable energy ($\bar{E}_\alpha$) MeV	Standard deviation (σ_{E_α}) MeV	Most probable energy ($\bar{E}_t$) MeV	Standard deviation (σ_{E_t}) MeV	Most probable energy ($\bar{E}_p$) MeV	Standard deviation (σ_{E_p}) MeV
1	15.01±0.09	4.40±0.03	8.60±0.16	2.92±0.05	6.80±0.16	1.81±0.05
2	14.95±0.08	4.21±0.03	8.59±0.14	2.59±0.05	6.91±0.15	1.84±0.05
3	14.73±0.12	4.33±0.03	8.66±0.20	2.83±0.05	6.70±0.16	1.78±0.05
Mean	14.85±0.25	4.30±0.12	8.65±0.21	2.75±0.21	6.80±0.26	1.81±0.08
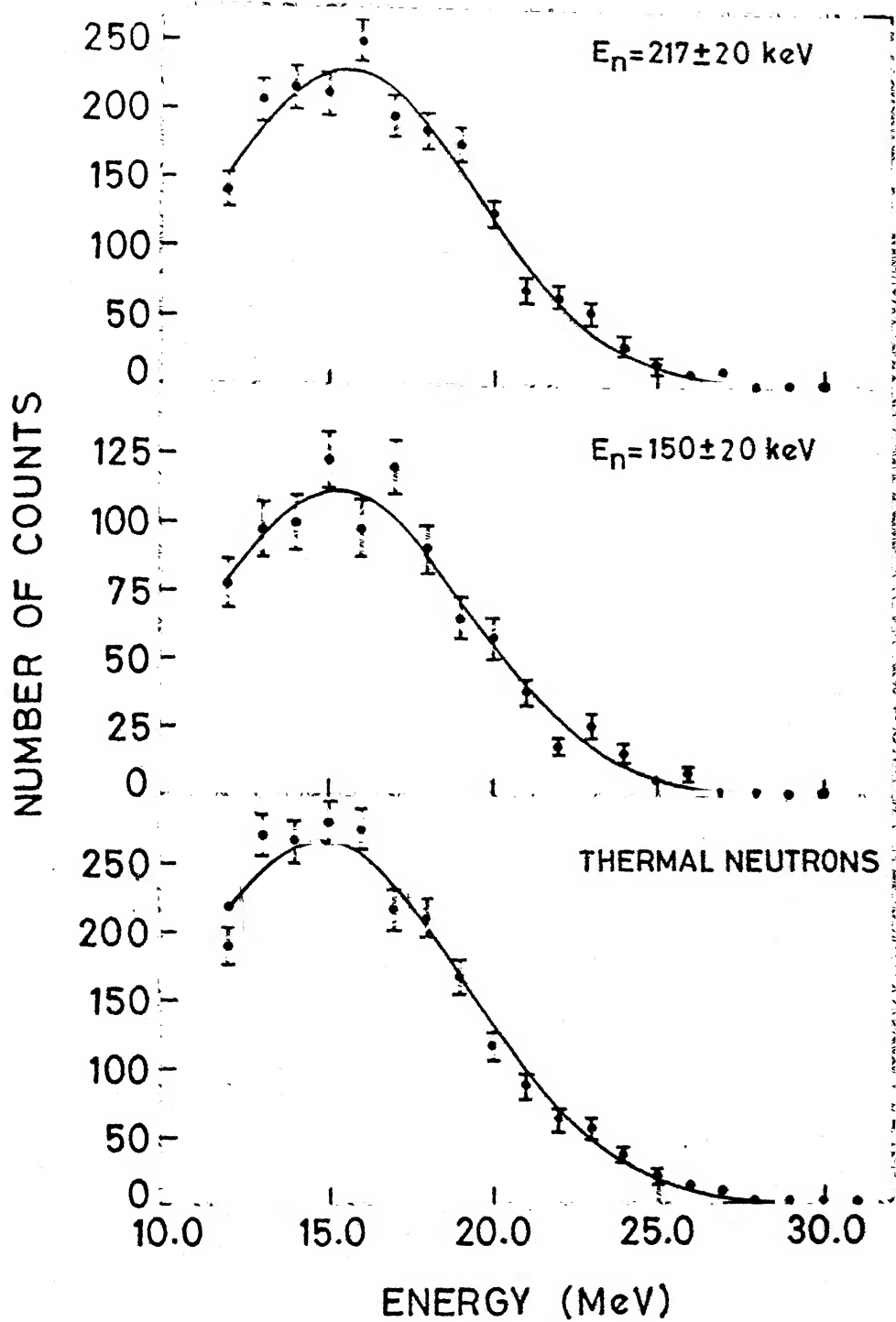
Fig.2.13. The LRA energy spectra for various incident neutron energies.
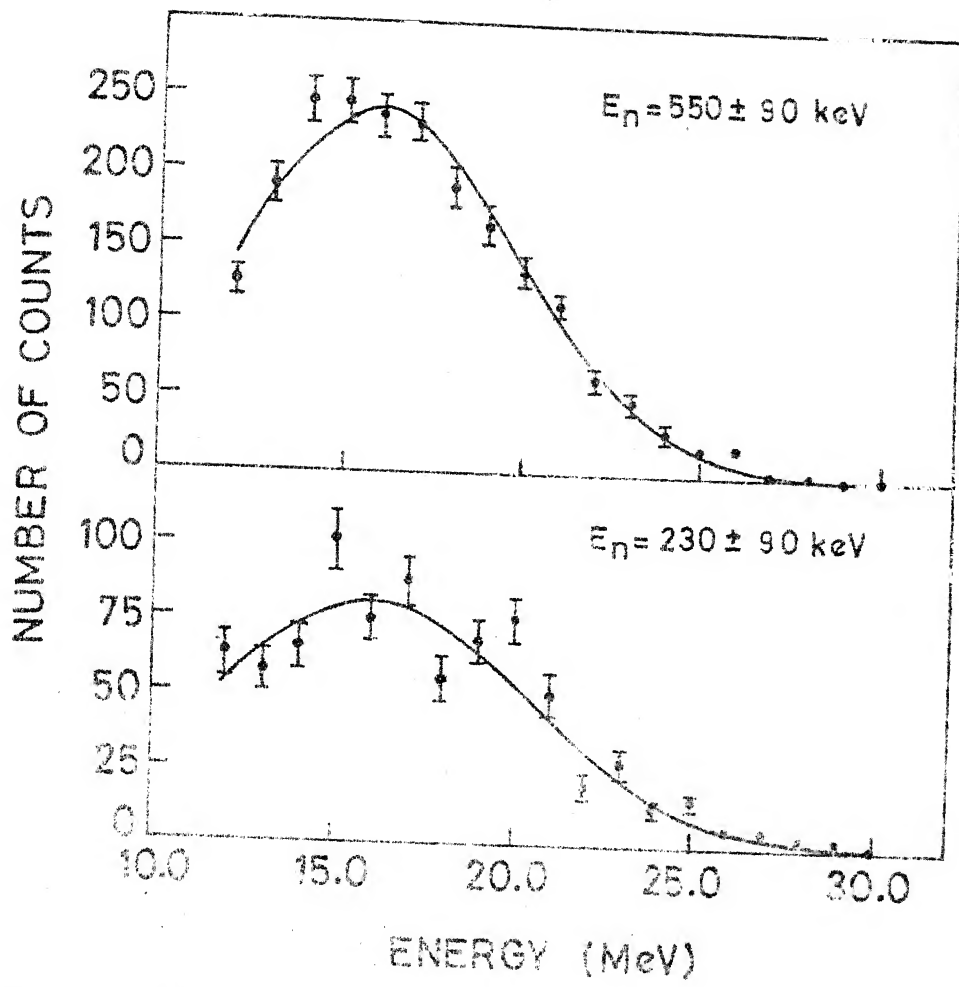
Fig. 2.13. (contd.) The LRA energy spectra for various incident neutron energies.

aluminium foil, the argon gas of the ionization chamber and
the $\triangle E$ detector and is found to be about 12 MeV. These energy
spectra were least square fitted to Gaussian shapes and the
energy distribution parameters, namely the most probable energy
($\bar{E}_\alpha$) and the standard deviation (σ_{E_α}) were thus determined.
The values of $\bar{E}_\alpha$ and σ_{E_α} for different incident neutron
energies are listed in Table - 2.5. The variations of $\bar{E}_\alpha$ and
σ_{E_α} with incident neutron energy are shown in Fig. 2.14. As
mentioned earlier, the hatched areas shown in the figure
correspond to the uncertainties in the values of $\bar{E}_\alpha$ and σ_{E_α}
for the different thermal neutron induced fission runs taken
at different times. It is seen from the figure that there is
no striking difference in the values of $\bar{E}_\alpha$ and σ_{E_α} in the fast
neutron induced fission as compared to their values in the
thermal neutron induced fission. However, $\bar{E}_\alpha$ shows a slightly
increasing trend beyond E_n = 230 keV. In an earlier measure-
ment, Krishnarajulu et al. [11] observed an increase of about
1 MeV in the value of $\bar{E}_\alpha$ in the energy range from 200 keV
to 700 keV while σ_{E_α} is observed to be insensitive to the
variation in the incident neutron energy.

The yields of alpha particles for different neutron
energies were obtained from the number of counts observed
beyond the energy cut-off value of 12 MeV. The results on
the yields of alpha particles per fission after normalising
the observed yield for the thermal neutron induced fission

Table - 2.5   The most probable energy and the standard
               deviation of alpha particle energy distri-
               butions for various incident neutron
               energies.

Neutron Energy (keV)	Most Probable Energy $(\bar{E}_\alpha)$ (MeV)	Standard Deviation (σ_{E_α}) (MeV)
THERMAL	14.85 ± 0.25	4.30 ± 0.12
150 ± 20	15.50 ± 0.12	4.03 ± 0.03
217 ± 20	15.80 ± 0.09	4.00 ± 0.02
230 ± 90	16.24 ± 0.22	4.37 ± 0.05
550 ± 90	15.86 ± 0.17	4.36 ± 0.04

Table - 2.6   Yields of alpha particles, tritons and protons
               for various incident neutron energies.

Neutron Energy (keV)	Y_{alpha} (x10^3)	Y_{triton} (x10^4)	Y_{proton} (x10^4)
THERMAL	2.00 ± 0.040 [*]	1.40 ± 0.110	1.84 ± 0.121
150 ± 20	2.66 ± 0.083	2.07 ± 0.230	3.14 ± 0.290
217 ± 20	2.26 ± 0.044	2.33 ± 0.160	3.19 ± 0.189
230 ± 90	2.58 ± 0.064	3.00 ± 0.460	7.20 ± 0.701
550 ± 90	1.94 ± 0.080	4.82 ± 0.213	17.64 ± 0.401

* normalized
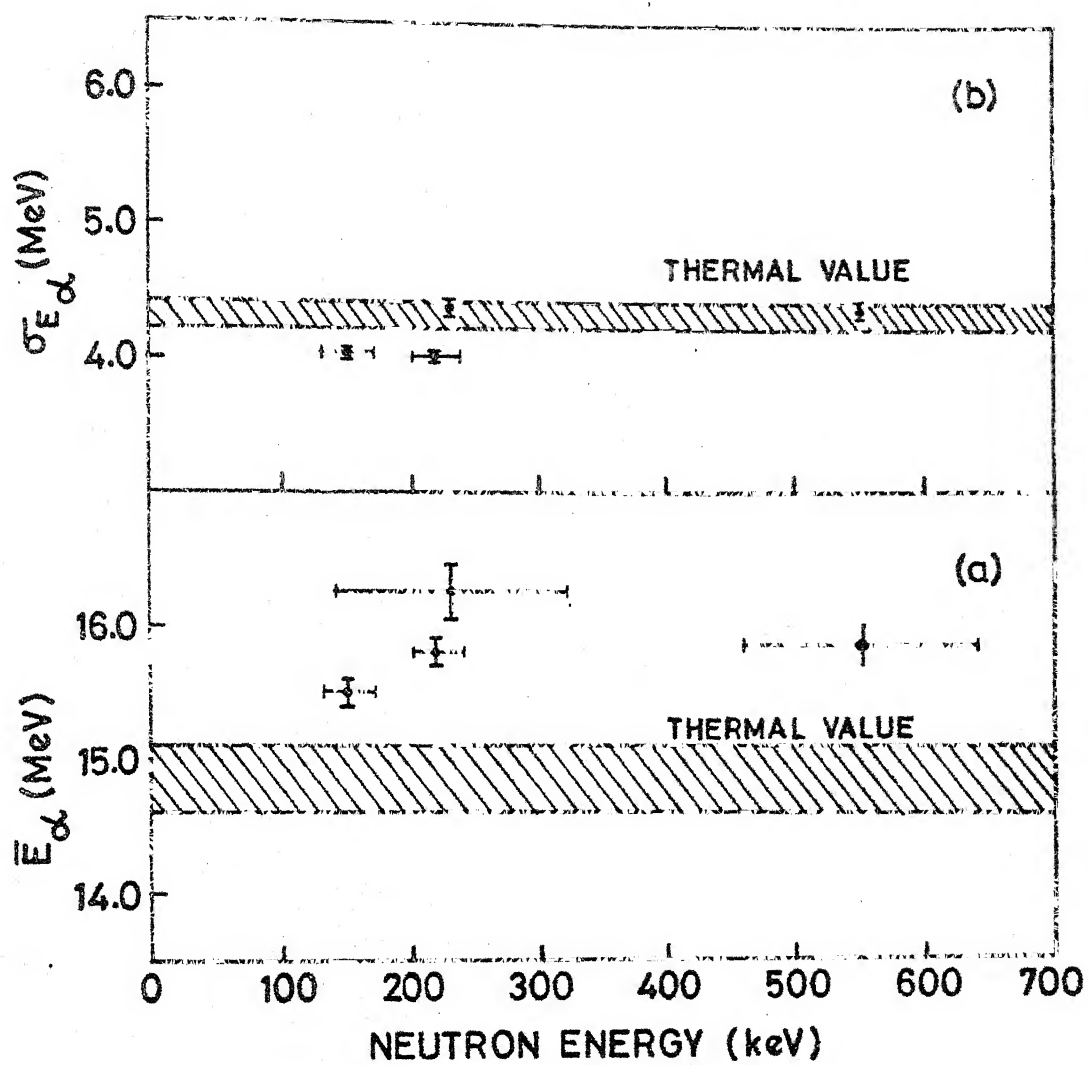
Fig. 2.14. Variation of (a) the most probable alpha particle energ
($\overline{E}_\alpha$) and (b) the standard deviation (σ_{E_α}) with incident
neutron energy.

to the known [10] absolute value of 2×10^{-3} per fission are shown in Fig. 2.15(a). It is seen from the figure that there is some structure in the yield of alpha particles around E_n = 200 keV, with the yield being higher by about 20 % at this neutron energy as compared to the value for the thermal neutron induced fission. At E_n = 550 keV, however, the alpha particle yield coincides with the thermal neutron value. This result is in good agreement with the earlier measurement [11] in which a similar structure was also observed in the yield of light-charged-particles beyond 12 MeV. At neutron energies between 500 keV and 1 MeV, Krishnarajulu et al. [11] found this yield to be the same as that for thermal neutrons. Beyond E_n = 1 MeV, the yield was also measured [37] and was found to be equal to that for thermal neutron induced fission within the limits of error.

The increase in the yield around E_n = 200 keV can not be attributed to any excitation energy dependence since the change in the compound nucleus excitation energy is very small and the yield does not vary monotonically with neutron energy. Moreover, previous measurements [11,37] showed that the yield for neutron energies above E_n = 600 keV is the same as that of thermal neutron fission. In the thermal neutron fission (s-wave fission) of ^{235}U ($\frac{7}{2}^-$) the states 3^- and 4^- are accessible to the fissioning nucleus and at neutron energies around E_n = 200 keV, the p-wave contribution to
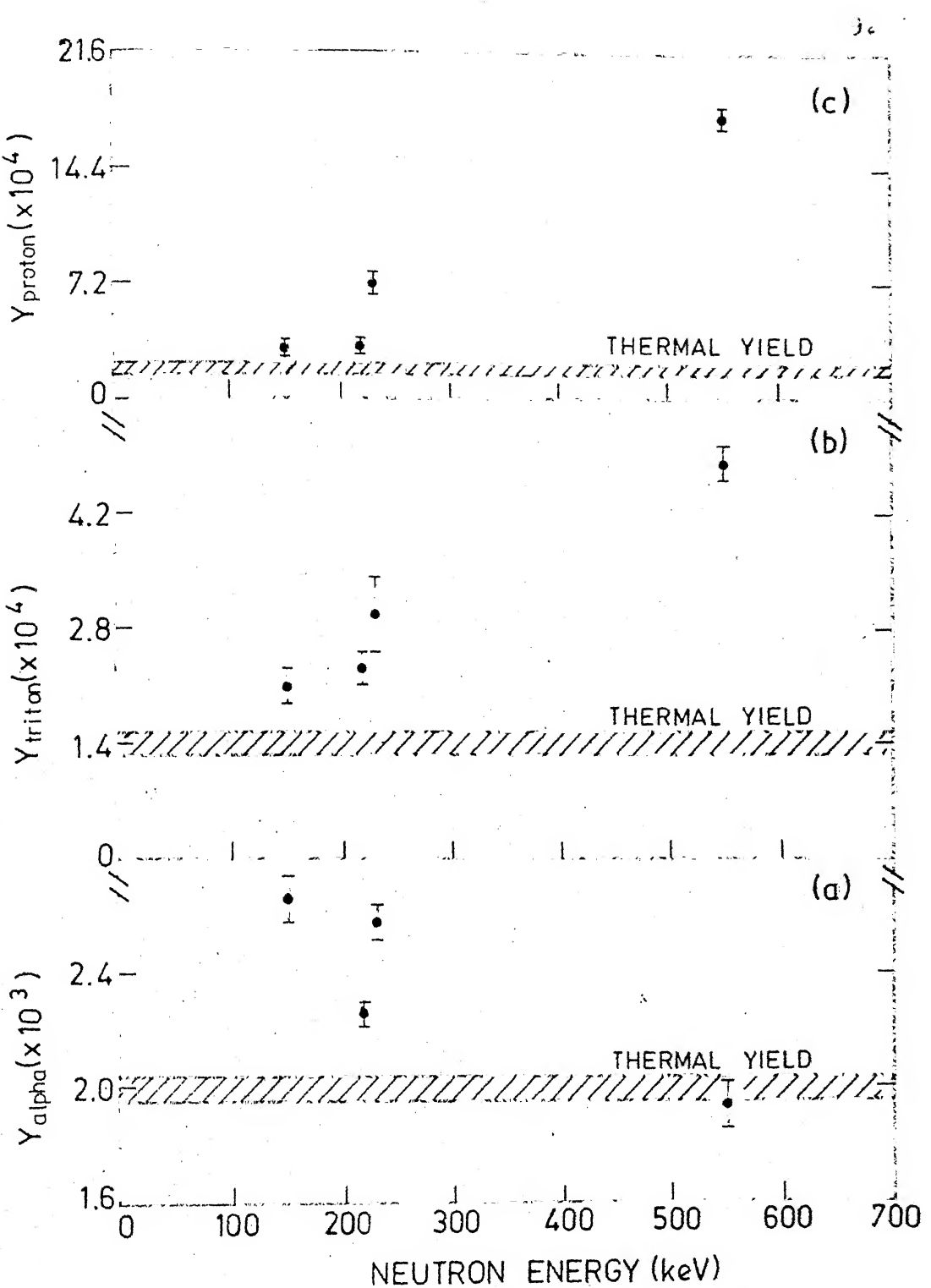
Fig. 2.15. Variation of (a) alpha particle yield; (b) triton yield and (c) proton yield with incident neutron energy.

the fission cross section is expected to dominate and the states 2^+, 3^+, 4^+ and 5^+ are accessible to the fissioning nucleus. At still higher neutron energies, the higher partial waves also contribute to the fission cross section and therefore the states of both parities are accessible to the fissioning nucleus at higher neutron energies. Thus the increase in the yield of alpha particles around E_n = 200 keV may be associated with the increase in relative number of fissions proceeding via the even parity states populated by p-wave interaction at these energies. Since the positive parity states lie lower ($\sim$0.6 MeV) than the negative parity states, the extra energy available at the saddle point in the p-wave fission can go into the degrees of freedom such as deformation, fragment kinetic energy, fragment excitation energy or into light-charged-particle emission. An increase in the number of prompt neutrons in p-wave fission at these neutron energies as compared to that for thermal neutrons [45] evidenced that the extra energy may go into the excitation energy of the fission fragments. The higher yield of alpha particles in this energy region indicates that the extra energy may also be available for alpha particle emission. At higher neutron energies, the averaging over all the fission channels takes place in such a way that the yield equals to that for thermal neutrons.

In a measurement for the case of ^{239}Pu [12]
Krishnarajulu et al. observed a drop in the yield of alpha
particles for the neutron energies in the range from 200-400
keV. At these neutron energies the domination of the p-wave
interaction provides negative parity state (1^- state)
accessible to the fissioning nucleus. Since the negative
parity state (1^- state) lies higher [45] than the 0^+ ground
state, the energy available for light-charged-particle
emission reduces and hence a drop in the yield of alpha
particles.

To establish the fission channel-effects on the yield
of alpha particles more firmly, the measurement with better
neutron energy resolution is required. The radiation damage
due to neutrons makes the use of surface-barrier detectors
impractical. We have used cellulose nitrate track detector
to study the fine variation of yield of alpha particles as a
function of neutron energy in the range 150-450 keV. These
results are presented in Chapter IV.

2.8.3 Tritons

Fig. 2.16 shows the energy spectra of tritons for
various incident neutron energies. The low-energy cut-off
in the energy spectra is seen to be about 6.5 MeV. These
spectra were least square fitted to the Gaussian shapes.
The results on the most probable energy ($\bar{E}_t$) and the
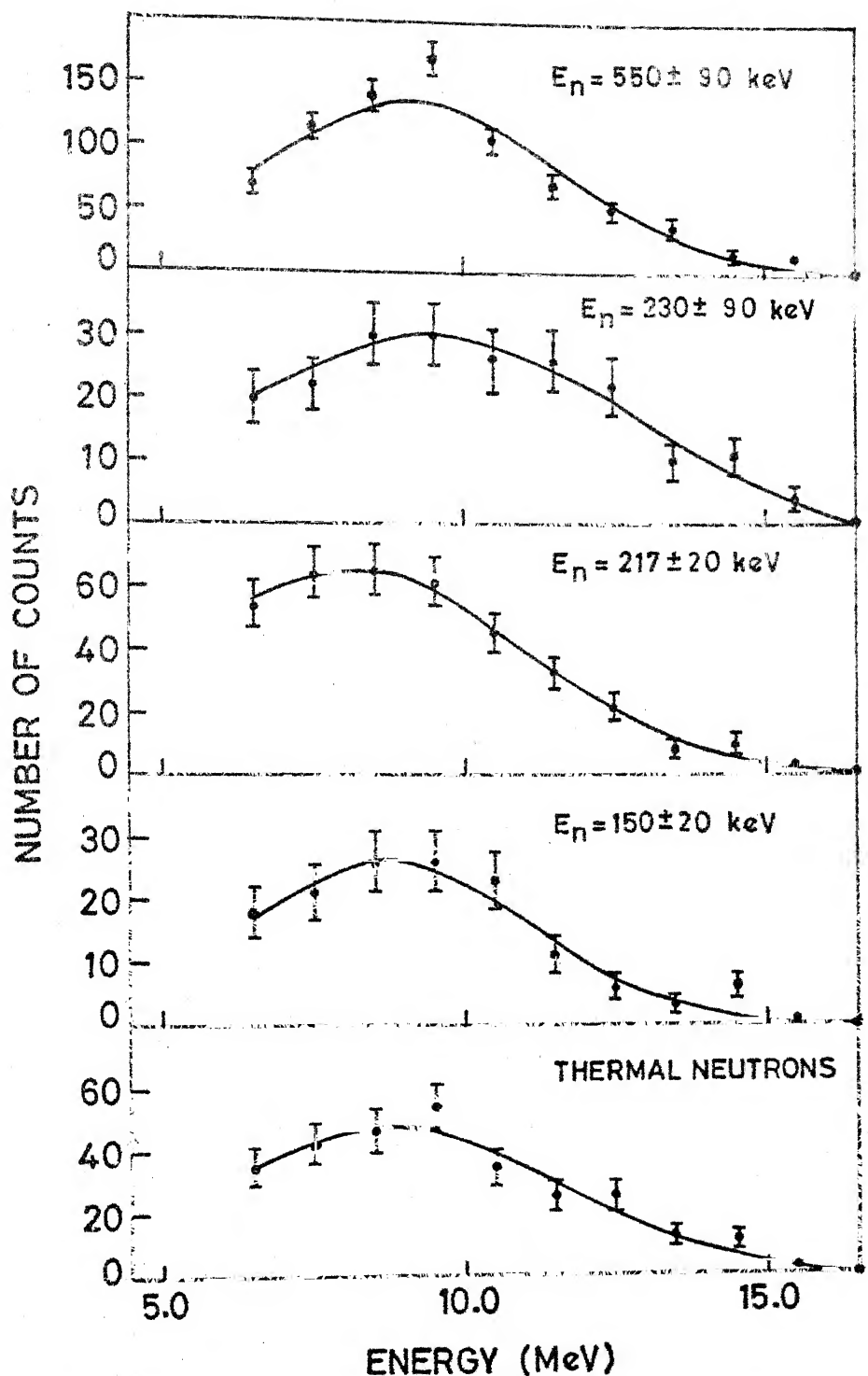
Fig. 2.16. Triton energy distributions for various incident neutron energies.

standard deviation (σ_{E_t}) are listed in the Table - 2.7. The variations of $\bar{E}_t$ and σ_{E_t} with the incident neutron energy are shown in Fig. 2.17. It is seen from the figure that there is no noticeable variation in the values of $\bar{E}_t$ and σ_{E_t} with the incident neutron energy.

The results on the yields of tritons for thermal and various fast neutron induced fission runs are shown in Fig. 2.15(b). It is seen that the yield of tritons for thermal neutron fission is about 6.5 percent of that of the alpha particles, which is in agreement with the earlier known values [22]. The yield, however, increases significantly at higher neutron energies such that at E_n = 550 keV, it is about 3.5 times that of the thermal neutron induced fission.

Fluss et al. [36] had earlier observed an abrupt increase in the yield of tritons in the fast neutron induced fission of ^{235}U above E_n = 150 keV by a factor of about 2 to 3 times that for thermal neutron induced fission. They had remarked that their data were not sufficiently precise to establish the energy dependence of the yields they observed. The present measurements, show that the yield of tritons increases gradually with the incident neutron energy. In an earlier measurement [11] from our lab, the yield of tritons at E_n = 500 keV was found to be about three times that of the thermal neutron fission, beyond E_n = 500 keV the yield was found to be decreasing but to be always higher than the

Table - 2.7 The most probable energy and the standard deviation of tritons for various incident neutron energies.

Neutron Energy (keV)	Most Probable Energy ($\bar{E}_t$) (MeV)	Standard Deviation (σ_{E_t}) (MeV)
THERMAL	8.65 ± 0.21	2.75 ± 0.21
150 ± 20	8.55 ± 0.20	2.44 ± 0.05
217 ± 20	7.89 ± 0.15	2.91 ± 0.05
230 ± 90	9.10 ± 0.45	3.10 ± 0.16
550 ± 90	8.82 ± 0.16	2.70 ± 0.05

Table - 2.8 The most probable energy and the standard deviation of protons for different incident neutron energies.

Neutron Energy (keV)	Most Probable Energy ($\bar{E}_p$) (MeV)	Standard Deviation (σ_{E_p}) (MeV)
THERMAL	6.80 ± 0.26	1.81 ± 0.08
150 ± 20	6.80 ± 0.35	1.84 ± 0.12
217 ± 20	6.92 ± 0.20	1.78 ± 0.09
230 ± 90	6.72 ± 0.16	2.17 ± 0.06
550 ± 90	6.66 ± 0.13	2.40 ± 0.05
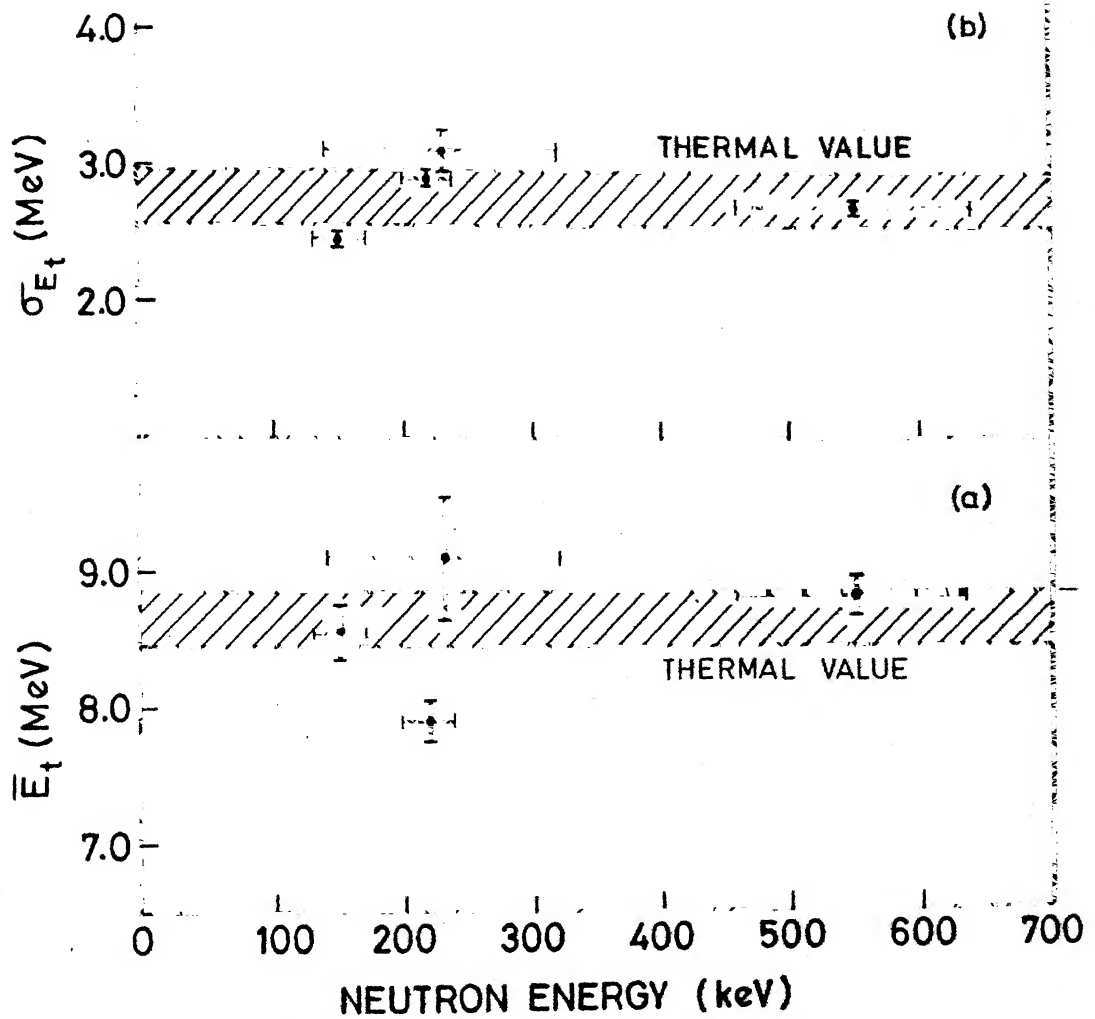
Fig. 2.17. Variation of (a) the most probable triton energy ($\overline{E}_t$) and (b) the standard deviation (σ_{E_t}) with incident neutron energy.

thermal value. Although the method used in the earlier experiment to extract the triton yield was not quite satisfactory, these results agree well with the present results.

The variation in the yield of tritons with the incident neutron energy is altogether different in nature as compared to that of alpha particles. The striking increase in the yield of tritons at higher incident neutron energies can not be explained by the existing models of emission mechanism of light-charged-particles in fission [2,3]. These results will be further discussed below along with the results obtained for protons.

2.8.4 Protons

As mentioned earlier, the yield of protons observed in the present experiment for the case of thermal neutron induced fission is significantly higher than the previously reported values [22]. This difference can arise due to the present experimental geometry used for detection of the fission fragments and light-charged-particles. The fission fragments emitted at angles close to 90° with respect to the mean direction of the light-charged-particle detection in the ΔE-E detectors, have a lower efficiency of detection in the ionization chamber, due to the fact that at these large angles, the fragments get stopped in the thick source

foil used in the present experiment. The detection efficiency of the fragments in the ionization chamber was estimated by carrying out Monte Carlo calculations with the known fission fragment light-charged-particle angular correlations and for the equatorial emission of alpha particles, it was found to be only 20 %. This reduction in the events corresponding to the equatorial emission of alpha particles results in a relatively greater weightage to the polar particles. Since the polar alpha particles constitute a very small fraction ($\lesssim 2$ %) of the equatorial alpha particles, this does not cause any appreciable change in the observed energy spectra of alpha particles. But since the ratio of the yield of protons to alpha particles in the case of polar emission is about 20 times more than that for equatorial emission [46] the observed yield of protons is significantly enhanced. The earlier measurements [22] for the proton yield correspond to only equatorial emission, whereas the present measurement includes both the types of events.

Since the ratio of the yield of tritons to that of alpha particles in the case of polar emission is about the same as that for equatorial emission [46], the reduction in the events corresponding to the equatorial emission resulting in greater weightage for the polar particles does not change the observed energy spectra of tritons appreciably. The yield, however, remains same for thermal neutron induced fission as reported earlier.

The results on the energy spectra of protons for different incident neutron energies are shown in Fig. 2.18. The cut-off in the energy spectra is seen to be about 3.5 MeV. The most probable values of energy ($\bar{E}_p$) and the standard deviation (σ_{E_p}) of the energy spectra, obtained by least squares fitting to the Gaussian shapes, are listed in the Table − 2.8. The variations of $\bar{E}_p$ and σ_{E_p} with the incident neutron energy are shown in Fig. 2.19. The average energy of protons in the thermal neutron fission is about 6.8 MeV, which is slightly lower than the earlier reported values [22] of about 8.2 MeV. This, as mentioned earlier, is because the depletion depth of the detector used was enough to absorb only 11 MeV protons. However, we can say that there is no significant variation of $\bar{E}_p$ and σ_{E_p} with the incident neutron energy.

The results on the yield of protons for various incident neutron energies are shown in Fig. 2.15(c). In many of the earlier measurements [17-19], the determination of the yield of protons in fission has been marked with difficulties due to the contributions from (n,p) reactions and a few experiments [18] indicated the presence of two or three components in the energy spectra of protons. In the present experiment, since the fission coincidence was ensured, any contribution due to (n,p) reactions can only be due to the fission neutrons. The possible such reaction is $^{27}Al(n,p)^{27}Mg$
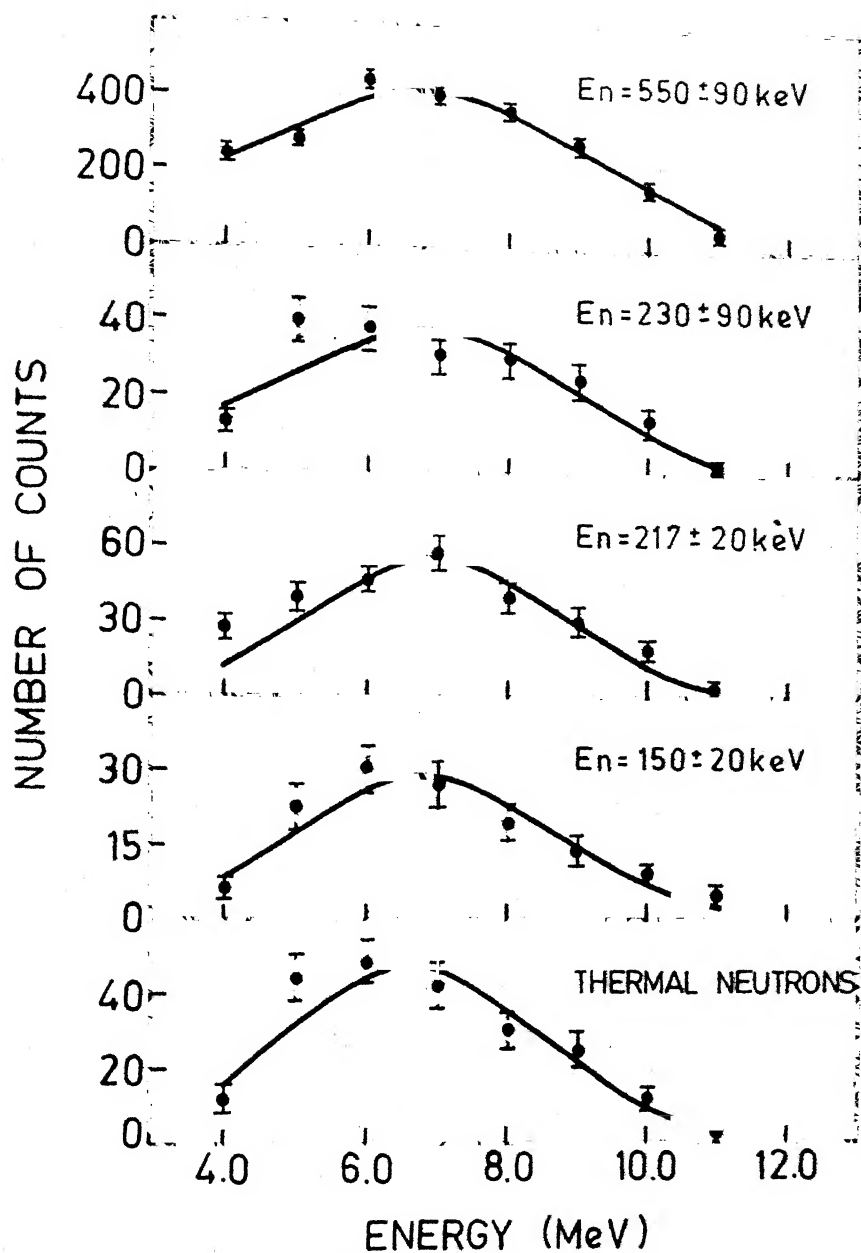
Fig. 2.18. The proton energy spectra for various incident neutron energies.
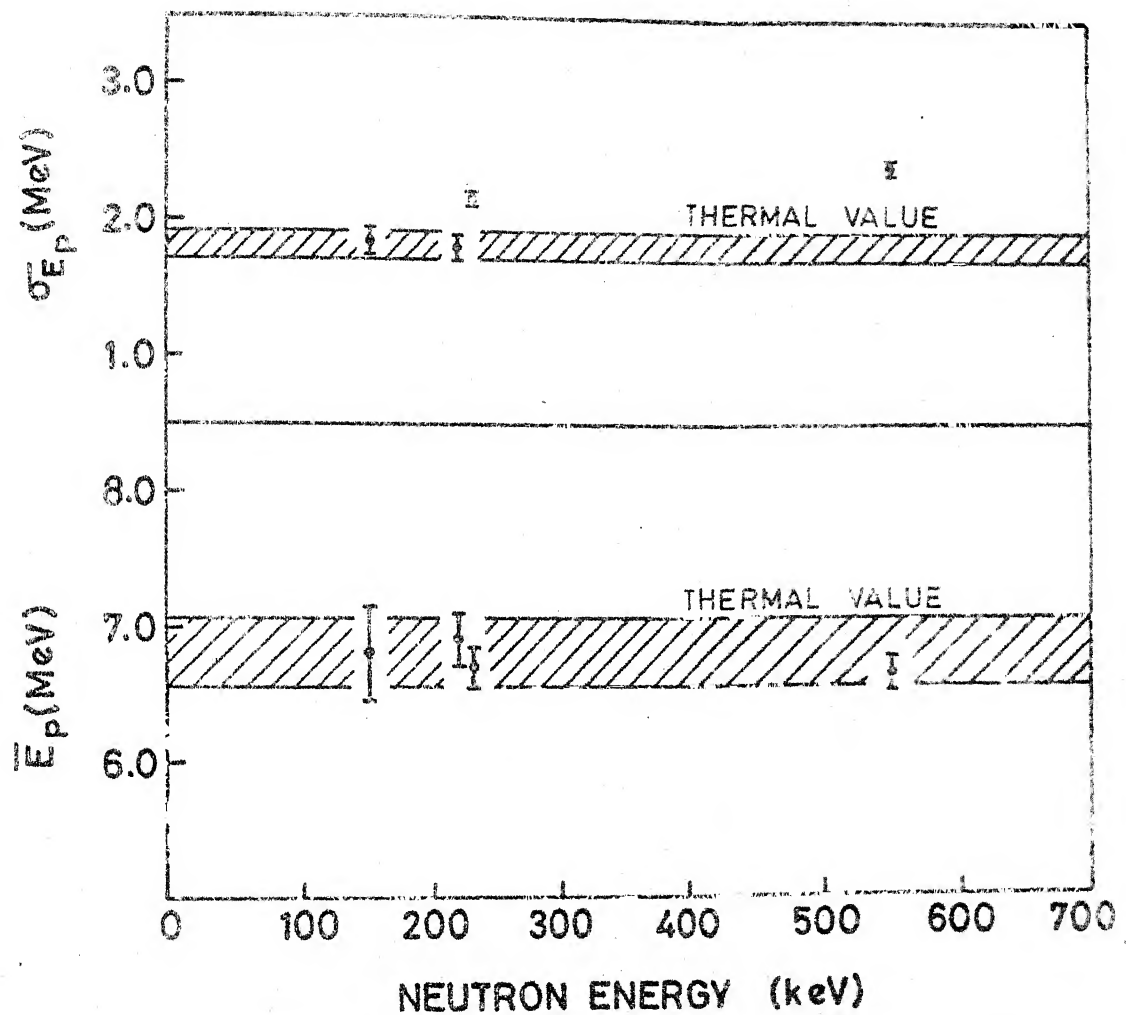
Fig. 2.19. Variation of (a) the average proton energy ($\bar{E}_p$) and (b) the standard deviation (σ_{E_p}) with incident neutron energy.

in our measurements which can interfere with fission protons.
The contribution of these events was estimated to be negligible
($\leqslant 0.5 \%$). It is seen from Fig. 2.15(c) that the yield of
protons increases very strongly with neutron energy. The
yield at E_n = 550 keV is about ten times that for the thermal
neutron fission. Such a strong increase in the yield of
protons at higher incident neutron energies can be due to the
increase in either the polar events or the equatorial type
of events. The emission mechanism of polar particles has been
assumed to be different [46] from that of the equatorial
particles and the present results should prove to be important
in the investigation of the true origin of these particles.
In the same way, the increase in the yield of tritons at
higher incident neutron energies can also be either due to
the polar or the equatorial type of events. Further experi-
ments are under progress to resolve the polar and the
equatorial type of events.

2.8.5 Relative Yields

The yields of alpha particles, tritons and protons
per fission for various incident neutron energies are
tabulated in Table - 2.6 and the yields of tritons and
protons per 100 alpha particles are listed in the Table -
2.9. The first and third columns of Table - 2.9 represent the
observed yields of tritons and protons per 100 alpha particles

Table - 2.9   Relative yields of tritons and protons per hundred alpha particles for various incident neutron energies.

Neutron Energy (keV)	Triton Yield		Proton Yield	
	Observed	Extrapolated	Observed	Extrapolated
THERMAL	7.04±0.57	6.40±0.49	9.25±0.66	8.46±0.48
150 ± 20	7.89±0.93	7.50±0.83	11.83±1.12	10.97±1.11
217 ± 20	10.31±0.75	11.30±0.75	14.15±0.90	14.01±0.83
230 ± 90	11.23±1.79	12.10±1.73	27.04±2.57	28.37±2.46
550 ± 90	25.01±1.23	23.40±1.07	91.22±2.74	92.03±2.71

respectively. The extrapolated total yields of alpha particles, tritons and protons were obtained as described in the section 2.7.4. The extrapolated yields of tritons and protons per 100 alpha particles are also given in the second and fourth columns of Table - 2.9 respectively.

Previous studies [3] have related the yields of light-charged-particles to the calculated release energy, defined as the energy cost of producing and placing a third particle between the two parent fission fragments. The release energy E_R is the sum of the binding energy of light-charged-particle to its mother fragment, the change in Coulomb potential and the initial kinetic energy. All the light-charged-particles emitted from thermal neutron induced fission of ^{235}U, having $Z \geqslant 4$, have shown a systematic dependence of yield with calculated release energies which can be expressed as

$$y \propto e^{-E_R/T} \tag{2.6}$$

where T is a constant. The yields of other light-charged-particles ($Z \leqslant 4$) do not follow the above relationship. For example, the triton yield is about a factor of 10 less than the expected value based on calculated release energy.

The present results on the unusual increase in the relative yields of protons and tritons with incident neutron energy can be interpreted on the basis of the potential

energy change encountered by the light particles in fast neutron fission. According to the Halpern's Sudden Snap model, the change may be more sudden in fast neutron fission as compared to that in thermal neutron induced fission for lighter particles and therefore the transfer of energy to protons and tritons etc. seems to be more efficient than alpha particles. The present results indicate that, if the equation (2.6) is valid for particles $Z < 4$ also, the effective release energy for protons or tritons decreases by a large factor at higher incident neutron energies while the release energy for alpha particles does not change much. This poses a question as to how the release energies for protons and tritons are very sensitive functions of small changes in the excitation energy while it is not true for alpha particles?

2.9 Errors in the Present Measurements

Reliability of any experimental finding is indicated by total error or by sources of errors involved in the experimental measurements. Since the fission cross section of ^{235}U for thermal neutrons ($\sim$600 barns) is very large as compared to that for keV neutrons ($\sim$1.5 barns), a trace of thermal neutrons in keV neutrons beam will produce a large discrepency in the keV neutron results. Therefore, the contribution of thermal neutrons in the keV neutron

energy runs and the error due to statistics are the two main sources of errors in the present measurements. These are described below.

(a) Error due to the contribution of thermal neutrons in the keV neutron energy runs

To produce a reasonably high neutron flux ($\simeq 10^7$ neutrons per sec), a large proton beam current ($\geqslant 20\mu A$) is required. This proton current produces a lot of heat at the neutron producing target (lithium or tritium) which causes evaporation of the target material and hence reduces the life of the target. To overcome this, the target has to be continuously cooled by flowing chilled water through a copper tube wrapped around the target holder. Because of multiple scattering in water, some of the neutrons get thermalized and reach the fissile target. Thermal neutrons can also originate due to the reflection from walls, electronic units etc. and can reach to the fissile target. Since the ratio of thermal neutron fission cross section to keV neutron fission cross section is about 400 for ^{235}U, a small percentage of thermal neutrons in keV neutrons is going to contribute quite a lot.

A separate experiment was performed to determine the ratio of thermal neutron flux to keV neutron flux at different neutron energies in the energy interval from 120 keV

to 600 keV. Two indium foils (having equal mass and equal size) one covered with cadmium and the other uncovered were used for this purpose. The samples were placed at the position of the fissile target symmetrically around the 0° direction of neutron beam. After irradiating for about two hours continuously, the γ-activity of the samples were measured with the help of a NaI(Tl) scintillation detector. The ratio of thermal to keV neutrons at $E_n = 150$ keV was found to be about 10^{-4} at the fissile target. At neutron energies above 150 keV, the ratio was even smaller than this value. Backward calculations have shown that about 4 % of the total fission events are produced due to the presence of thermal neutrons at neutron energies between 120 keV to 600 keV. This introduces an error of about 1.5 % - 3 % in the alpha particle yields, error of about 2 % - 4 % in the triton yields and error of about 1.5 % - 3 % in the proton yields.

(b) Statistical errors

Statistical errors depend on the total counts and therefore it varies from run to run. In the present measurements, it varies from 2 % to 4 % for alpha particle yields, from 6 % to 10 % for triton yields and from 3 % to 9 % for proton yields.

2.10 Conclusions

The most probable energies and the standard deviations of alpha particles, tritons and protons do not vary significantly in the neutron energy region from thermal to 600 keV.

The yield of alpha particles at neutron energies around E_n = 200 keV increases by 20 % as compared to that for the thermal neutron fission, which may be attributed to the even parity of the transition states accessible to the fissioning nucleus in this energy region. To establish this more firmly, the measurements with the better neutron energy resolution are necessary.

The variations in the yields of tritons and protons with the incident neutron energy are altogether different in nature as compared to that of alpha particles. Since the present results have a mixture of the polar and equatorial type of events, the increase in the yields of tritons and protons may be due to the increase in either the polar or the equatorial or both type of events. Further experiments are necessary to study the effect of incident neutron energy on both the types of events separately.

The measurement of yields of light-charged-particles in fission is important for the understanding of the nature of the three-fragment event because unlike energy and angular distribution measurements which sample post-fission Coulomb

forces, yields depend on the pre-scission motion of the nucleus. The present results emphasize the need of yield measurements of different light-charged-particles at still higher neutron energies.

REFERENCES

[1] G. Farwell, E. Segre and C. Wiegand, Phys. Rev. 71 (1947) 327.

[2] N. Feather, Proc. Second Symp. Phys. Chem. Fission (Vienna) Vol. II (1969) p. 83 (IAEA, Vienna).

[3] I. Halpern, Ann. Rev. Nucl. Sci. 21 (1971) 245.

[4] A.J. Deruytter and Neve de Mevergnies, Phys. Chem. Fission IAEA Symp. Salzburg Vol. II (1965) 429.

[5] E. Melkonian and G.K. Mehta, Phys. Chem. Fission IAEA Symp. Salzburg Vol. II (1965) 355.

[6] I.G. Schröder, A.J. Deruytter and J.A. Moore, Phys. Rev. B137 (1965) 519.

[7] C. Wagemans and A.J. Deruytter, Nucl. Phys. A194 (1972) 657.

[8] T.D. Thomas and S.L. Whetstone, Phys. Rev. 144 (1966) 1060.

[9] W.D. Loveland, A.W. Fairhall and I. Halpern, Phys. Rev. 163 (1967) 1315.

[10] R.A. Nobles, Phys. Rev. 126 (1962) 1508.

[11] B. Krishnarajulu, G.K. Mehta, R.K. Choudhury, D.M. Nadkarni and S.S. Kapoor, Pramana 8 (1977) 315.

[12] B. Krishnarajulu, S. Sen and G.K. Mehta, J. Phys. G : Nucl. Phys. 5 (1979) 319.

[13] J.C. Watson, Phys. Rev. 121 (1961) 230.

[14] H.E. Wegner, Bull. Am. Physical Soc. 6 (1961) 307.

[15] D.L. Horrocks, Phys. Rev. 134 (1964) B1219.

[16] S.L. Whetstone, Jr. and T.D. Thomas, Phys. Rev. Lett. 15 (1965) 298.

[17] S.L. Whetstone, Jr. and T.D. Thomas, Phys. Rev. 154 (1967) 1174.

[18] S.W. Cosper, J. Cerny and R.C. Gatti, Phys. Rev. 154 (1967) 1193.

[19] G.M. Raisbeck and T.D. Thomas, Phys. Rev. 172 (1968) 1272.

[20] D.E. Cumpstey and D.G. Vass, Proc. Fourth Symp. Phys. Chem. Fission (held in Jülich) (1979) (IAEA, Vienna).

[21] A.A. Vorobiev, D.M. Seleverstov, V.T. Grachov, I.A. Kondurov. A.M. Nikitin, A.I. Yegorov and Yu. K. Zalite, Phys. Lett.B30 (1969) 332.

[22] M. Dakowski, J. Chwaszczewska, T. Krogulski, E. Piasecki and M. Sowinski, Phys. Lett. B25 (1967) 213.

[23] V.N. Andreev, V.G. Nedopekin and V.I. Rogov, Sov. J. Nucl. Phys. 8 (1969) 22.

[24] A.A. Vorobiev, D.M. Seleverstov, V.T. Grachov, I.A. Kondurov, A.M. Nikitin, N.N. Smirmov and Yu.K. Zalite, Phys. Lett. B40 (1972) 102.

[25] A.A. Vorobiev, V.T. Grachov, A.P. Komar, I.A. Kondurov, A.M. Nikitin and D.M. Seliverstov, Sov. J. At. Energy 27 (1969) 713.

[26] G. Kugler and W.B. Clarke, Phys. Rev. C-5 (1972) 551.

[27] V.N. Andreev, V.G. Nedopekin and V.I. Rogov, Sov. J. Nucl. Phys. 9 (1969) 14.

[28] T. Krogulski, J. Chwaszczewska, M. Dakowski, E. Piasecki, M. Sowinski and J. Tys, Nucl. Phys. A128 (1969) 219.

[29] A.A. Vorobiev, V.T. Grachov, I.A. Kondurov, Yu.A. Miroshnichenko, A.M. Nikitin, D.M. Seliverstov and N.N. Smirnov, Sov. J. Nucl. Phys. 20 (1975) 248.

[30] C. Guet, C. Signarbieux, P. Perrin, H. Nifenecker, M. Asghar, F. Caitucolli and B. Leroux, Nucl. Phys. A314 (1979) 1.

[31] R.K. Choudhury, S.S. Kapoor, D.M. Nadkarni, P.N. Rama Rao and S.R. Srinavas Murthy, Pramana 6 (1976) 64.

[32] L.V. Drapchinski, S.S. Kovalenkov, K.A. Petrzhak and I.I. Tyutyugin, Sov. J. At. Energy 16 (1964) 164.

[33] T.D. Thomas and S.L. Whetstone, Phys. Rev. 144 (1966) 1060.

[34] W.D. Loveland, A.W. Fairhall and I. Halpern, Phys. Rev. 163 (1967) 1315.

[35] D.M. Nadkarni and S.S. Kapoor, Proc. Nucl. Phys. Solid State Phys. Symp. (India) 13B (1970) 73.

[36] M.J. Fluss, N.D. Dudey and R.L. Malewicki, Phys. Rev. C-6 (1972) 2252.

[37] D.M. Nadkarni, R.K. Choudhury, P.N. Rama Rao and S.S. Kapoor, Proc. Nucl. Phys. Solid State Phys. Symp. (India) 18B (1975) 131.

[38] P.B. Price and R.L. Fleischer, Ann. Rev. Nucl. Sci. 21 (1971) 295.

[39] F.S. Goulding and B.G. Harvey, Ann. Rev. Nucl. Sci. 25 (1975) 167.

[40] D.J. Skyrme, Nucl. Instr. Meth. 57 (1967) 61.

[41] L.C. Northcliffe and R.F. Schilling, Nucl. Data Tables A7 (1970) 233.

[42] W.D. Allen, In ''Fast Neutron Physics'', (J.B. Marion and J.L. Fowler, eds.) Vol. I (1960) 361. Interscience Publishers, New York.

[43] J.H. Gibbons and H.W. Newson, In ''Fast Neutron Physics'', (J.B. Marion and J.L. Fowler, eds.) Vol I (1960) 133. Interscience Publishers, New York.

[44] M. Coppola and H.H. Knitter, Kern. Isotope. Chemie. 10 (1967) 459.

[45] Yu. A. Blyumkina, I.I. Bondarenko, V.F. Kuznetsov, V.G. Nesterov, V.N. Okolovich, G.N. Smirenkin and L.N. Vsachev, Nucl. Phys. 52 (1964) 648.

[46] E. Piasecki and L. Nowichi, Proc. Fourth Symp. Phys. Chem. Fission (held in Zülich) (1979) (IAEA, Vienna).

CHAPTER III

ETCHING CHARACTERISTICS OF CN-85 CELLULOSE NITRATE TRACK DETECTOR

3.1 Introduction

The advantages of solid state nuclear track detectors (SSNTD) over nuclear track emulsions in detecting charged particles have resulted in an almost complete replacement of the latter in many fields of applications. The advantages of these detectors over semiconductor detectors are the spatial resolving power and the insensitivity of these detectors to beta particles, gamma rays and neutrons. The time-consuming evaluation and the insufficient energy resolution have been limiting the utility of these detectors in the past. However, the image analysing computers have made the evaluation very fast.

The story of track detectors started with the Young's study [1] of etching fission fragment tracks in lithium fluoride and the electron microscopic observation of fission fragment tracks in mica by Silk and Barnes [2]. Since then a tremendous amount of work has been done [3-4] to develope new track detector materials and to improve etching and counting techniques. Table - 3.1 lists some of the important track detector materials along with their characteristics. Normally these detectors are insensitive to light-charged-particles and thus behave like threshold detectors, recording all highly ionizing particles and ignoring all those charged particles which are lightly ionizing. Most of the laboratory made track detectors and naturally occuring mineral track detectors record fission fragments as well as heavy particles and are essentially unaffected in any direct way by immense doses of electrons, protons and even alpha particles. This property of seeing certain particles well and others not at all is a highly valued quality of any track detector. Cellulose nitrate track detector (CNTD) [5] is the most sensitive track detector material which can be used in alpha particle detection.

The etching characteristics of Kodak CN-85 (old trade name: CA 80-15) cellulose nitrate track detector have been studied in detail which are described in the present Chapter. The bulk-etch rate (V_B) is necessary to determine

Table - 3.1   Some important solid state nuclear track detectors.

Detector name	Composition	Particles (ions) studied
Muscovite Mica	$KAl_3Si_3O_{10}(OH)_2$	Fission fragments and heavy ions ($A \geqslant 20$)
Silica Glass	SiO_2	Fission fragments and heavy ions ($A \geqslant 40$)
Quartz	SiO_2	Fission fragments and heavy ions ($A \geqslant 40$)
Flint Glass	$18SiO_2:4PbO:1.5NaO_2:K_2O$	Fission fragments and heavy ions ($A \geqslant 20$)
Soda Lime Glass	$23SiO_2:5Na_2O:5CaO:Al_2O_3$	Fission fragments and heavy ions ($A \geqslant 20$)
Polyethylene	CH_2	Fission fragments
Lexan	$C_{16}H_{14}O_3$	Fission fragments and charged-particles heavier than alpha particles.
Makrofol	$C_{16}H_{14}O_3$	Fission fragments and particles heavier than Neon.
Cellulose Nitrate (Kodak-CN-85)	$C_6H_8O_9N_2$	Alpha particles and other ions heavier than alpha particles.

the removed layer of the track detector material by etching and for obtaining the true etched track-length from the observed etched track-length. The methods for measuring the bulk-etch rate are described in Section 3.2. The temperature dependence of the bulk-etch rate is used to determine the activation energy for the bulk-etching of the material.

The development of the rear-etching technique in the recent years has provided good energy resolution for alpha particles [6] and therefore these detectors have become very useful in the light-charged-particle spectroscopy. The method of rear-etching is described in the Section 3.4. The technique is then applied to obtain ^{227}Ac alpha energy spectrum and to obtain long-range alpha-particle (LRA) energy spectrum from spontaneous fission of ^{252}Cf. These results are presented and discussed in the Sections 3.5 and 3.6 respectively.

3.2 Bulk-Etch Rate Measurements

To determine the residual thickness of a track detector sample after etching it for certain period of time, one requires an accurate value of the bulk-etch rate (V_B) for the etching conditions used. The bulk-etch rate is defined as the speed with which the undamaged regular material of a track detector is dissolved out by an etchant. We have determined the bulk-etch rates of CN-85 cellulose

nitrate track detector in 6N NaOH solution at different
temperatures by two methods:

(i)   Gravimetric method,

(ii) Track-diameter method.

The gravimetric method is based on the loss of mass by
etching for certain time at a fixed temperature and concentra-
tion. A 100μm thick sample of CN-85 (size: 3 cm x 3 cm) of
known mass (m) was dipped inside 6N NaOH solution maintained
at a fixed temperature (62 $\pm$ 0.5 $^{\circ}$C) in a thermostat
controlled water bath. The detector foil was attacked by
the etchant uniformly normal to the two faces. After etching
for a certain period of time (30 minutes), the sample was
taken out of the solution and was thoroughly washed with the
de-mineralized water. After air-drying at room temperature,
the sample was weighed on a semi-micro balance again and
thus the mass loss ($\triangle$m) by etching was determined. The
layer removed (layer etched) from one face of the sample was
then calculated as follows:

Since the original thickness of the sample of mass (m) was
100 μm, the thickness removed from both the faces correspon-
ding to the mass loss ($\triangle$m) = $(\frac{\triangle m}{m})$ x 100 μm.

And therefore the layer removed from one face

$$= \frac{1}{2} \text{ x } (\frac{\triangle m}{m}) \text{ x } 100 \text{ μm.}$$

The mass loss due to the etching of the side faces was
calculated and it was found to be less than 1 % of the

total mass loss and therefore the contribution of the material etched out from the side faces of the sample was neglected in the calculations.

Fig. 3.1 indicates the variation of the thickness of the layer removed from one face of the sample with the cumulative etching time. The bulk-etch rate (V_B) obtained by least-squares fitting is

$$V_B = 6.720 \pm 0.008 \ \mu m/hr.$$

The rate of etching along the particle track in any track detector is known as the track-etch rate (V_T) which is always greater than the bulk-etch rate of the detector material. From the track-diameter kinetics [7], it is known that the particle tracks having $V_T/V_B \gg 1$ can be used to determine the bulk-etch rate along the surface plane. The rate of increase of the radius of the tracks equals the bulk-etch rate. Thus if Δd is the increase in track diameter in time Δt

$$\frac{\Delta d}{\Delta t} = 2V_B$$

or
$$V_B = \frac{1}{2}\left(\frac{\Delta d}{\Delta t}\right) \tag{3.1}$$

The track-diameter method of evaluating the bulk-etch rate is reliable only upto track-diameters of about 14 μm [8-9]. The track-diameter versus etching time curve remains linear in this range. The linearity is not preserved at larger
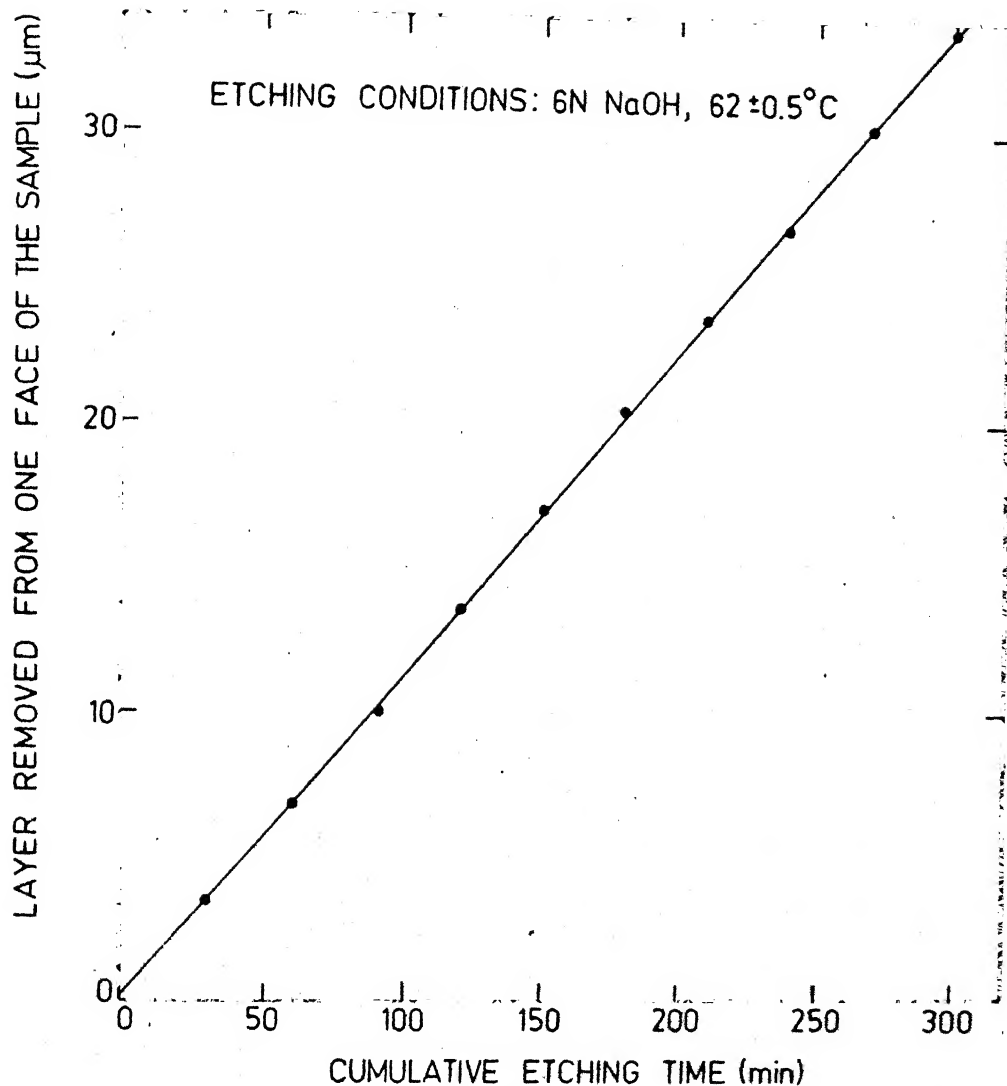
Fig. 3.1 Variation of the thickness of the layer removed from one face of the sample as a function of the cumulative etching time.

track-diameters because of the saturation effects [8].

A sample of CN-85 (size: 3 cm x 3 cm) was irradiated with ^{252}Cf spontaneous fission source in a vacuum chamber (Fig. 3.2). The source was kept at a distance of 2.5 cms from the detector foil. A collimator of 2 mm diameter was used in between the source and detector foil to prevent the obliquely incident fission fragments and to confine the area of interest. After irradiating for half an hour, the sample was etched in 6N NaOH solution kept at 62 ± 0.5 $^{\circ}$C in steps of 15 minutes. The variation of track-diameters with etching time is shown in Fig. 3.3. The bulk-etch rate obtained from this curve is

$$V_B = 6.7 \pm 0.5 \ \mu m/hr.$$

The measurements of the track-diameters were carried out at magnification of 1600. The uncertainty in the track-diameter measurements is ± 0.5 μm. The two bulk-etch rates, obtained from gravimetric method and track-diameter method, agree within the experimental uncertainties. This suggests that the bulk-etching is isotropic in CN-85 cellulose nitrate track detector and therefore this detector is suitable for rear-etching technique as described in the Section 3.4.

3.3 Temperature Dependence of the Bulk-Etch Rate and the Activation Energy of Bulk-Etching

Most of the non-crystalline materials such as plastics show an isotropic behaviour when etched in some

CN - 85 Foil
(Size: 3cm X 3cm)

Collimator of 2mm
diameter

^{252}Cf/ ^{227}Ac Source

Source Backing
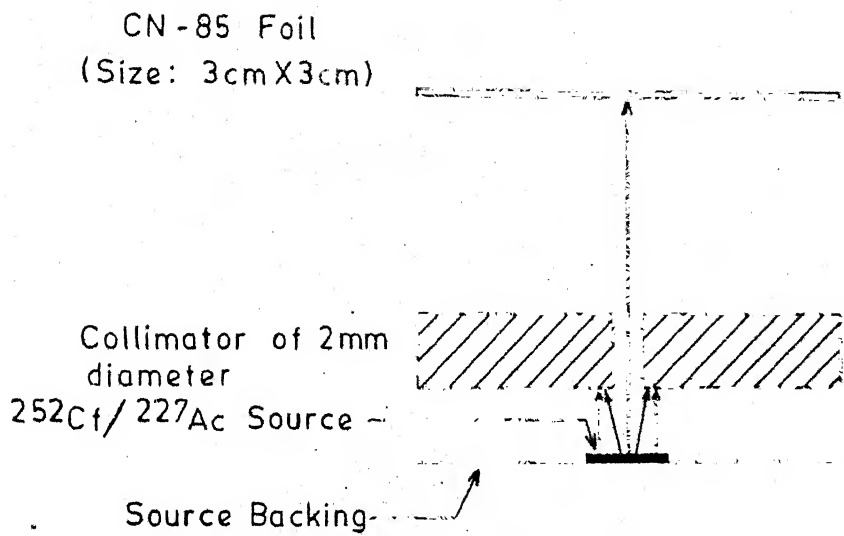
Fig. 3.2. Schematic diagram of the system used for irradiation of the detector foils in a Vacuum chamber.
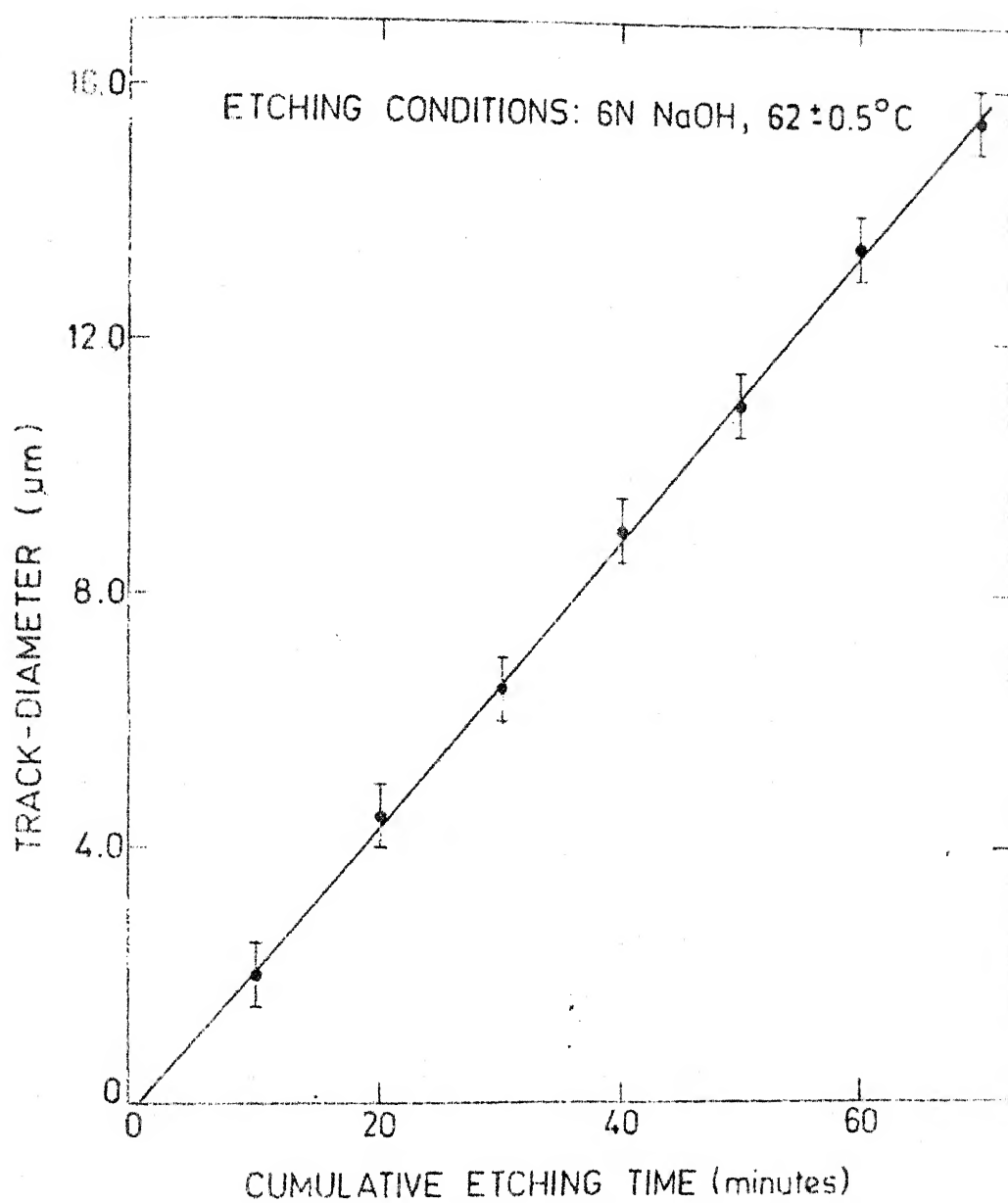
Fig. 3.3. Variation of track-diameter with cumulative etching time

chemical etchant [3]. The bulk-etch rates normal and along the surface of such solids are, therefore, equal, as has been seen in CN-85 cellulose nitrate track detector in the present study. The diameter of the initial damage-trails formed by undegraded fission fragments in plastics was found to be less than 100 $\overset{o}{A}$ [10]. The chemical etching results in a preferential attack along the track of the particle. The degree of damage and the track-etch rate both decrease with the depth of penetration inside the solid state nuclear track detectors for fission fragments. The etch-rate along the track beyond the damage-trail is equal to the bulk-etch rate of the undamaged material.

The growth of the track-diameter of the fission fragment tracks with the cumulative etching time has been measured in CN-85 at temperatures: $25^{o}C, 33^{o}C, 40^{o}C$, $50^{o}C$, $62^{o}C$ and $70^{o}C$. Fig. 3.4 shows the track-diameter versus cumulative etching time curves for these temperatures. By least-squares-fitting, the bulk-etch rates have been determined for different temperatures. These values are listed in the Table - 3.2.

Making use of the gravimetric technique, as described earlier, we have obtained the variation of the layer removed from one face as a function of the cumulative etching time at various temperatures. These curves are shown in Fig. 3.5. The values of bulk-etch rate at different temperatures,
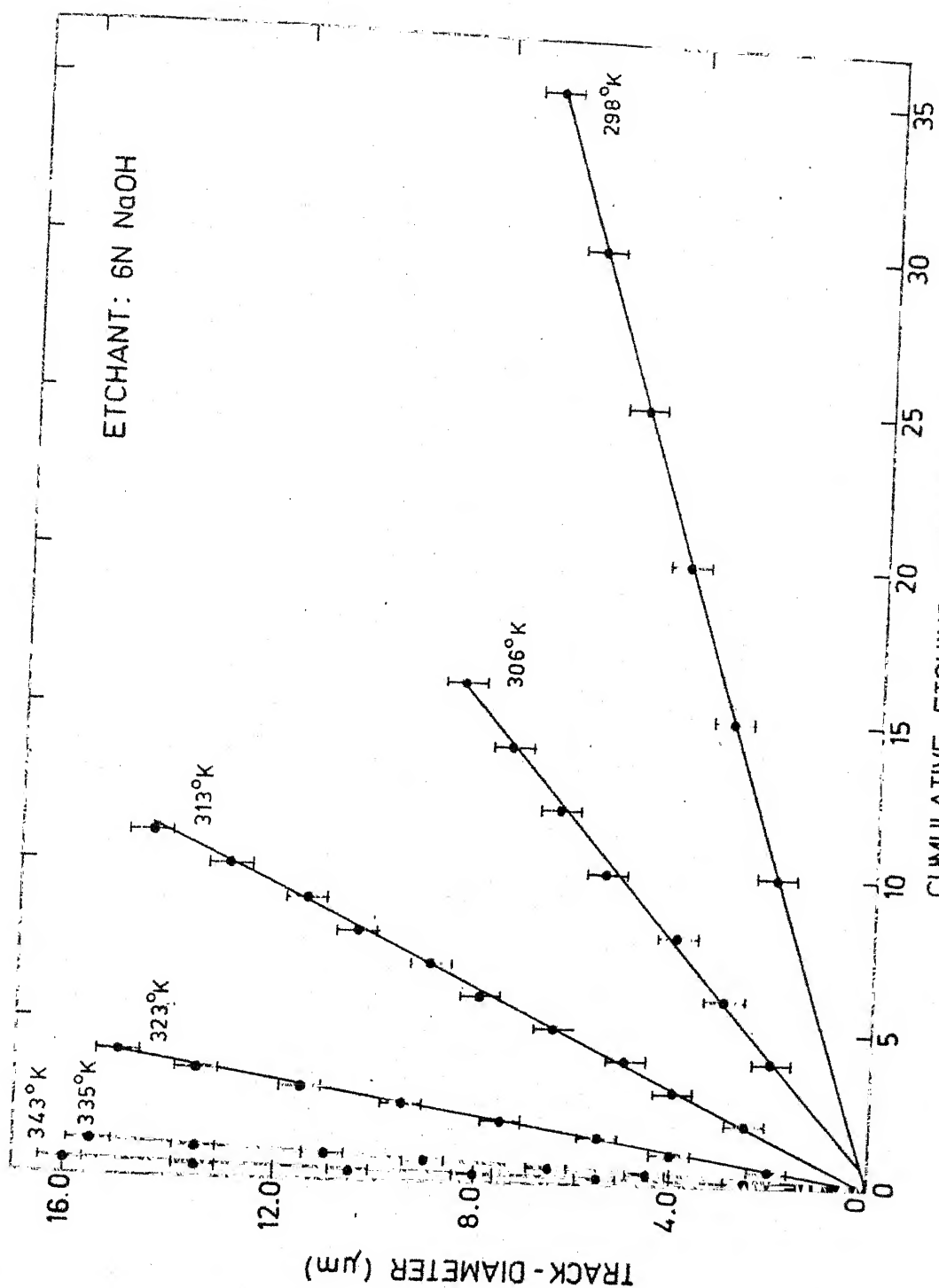
Fig. 3.4. Variation of track-diameter as a function of the cumulative etching time at various temperatures.

Table - 3.2   The bulk-etch rate (V_B) of CN-85 determined by two methods at various temperatures.

Etching Temp. (T) ($^\circ$C)	$\frac{1}{T}$ (X10^3) ($^\circ$K)$^{-1}$	Bulk-Etch Rate (μm/hr)	
		Gravimetric method	Track-diameter method
25 ± 0.5	3.356 ± 0.006	0.080 ± 0.001	0.10 ± 0.01
33 ± 0.5	3.268 ± 0.005	0.270 ± 0.005	0.28 ± 0.02
40 ± 0.5	3.195 ± 0.005	0.650 ± 0.004	0.65 ± 0.04
50 ± 0.5	3.096 ± 0.005	1.91 ± 0.01	1.89 ± 0.23
62 ± 0.5	2.985 ± 0.005	6.72 ± 0.01	6.75 ± 0.47
70 ± 0.5	2.915 ± 0.004	17.43 ± 0.01	16.20 ± 0.95
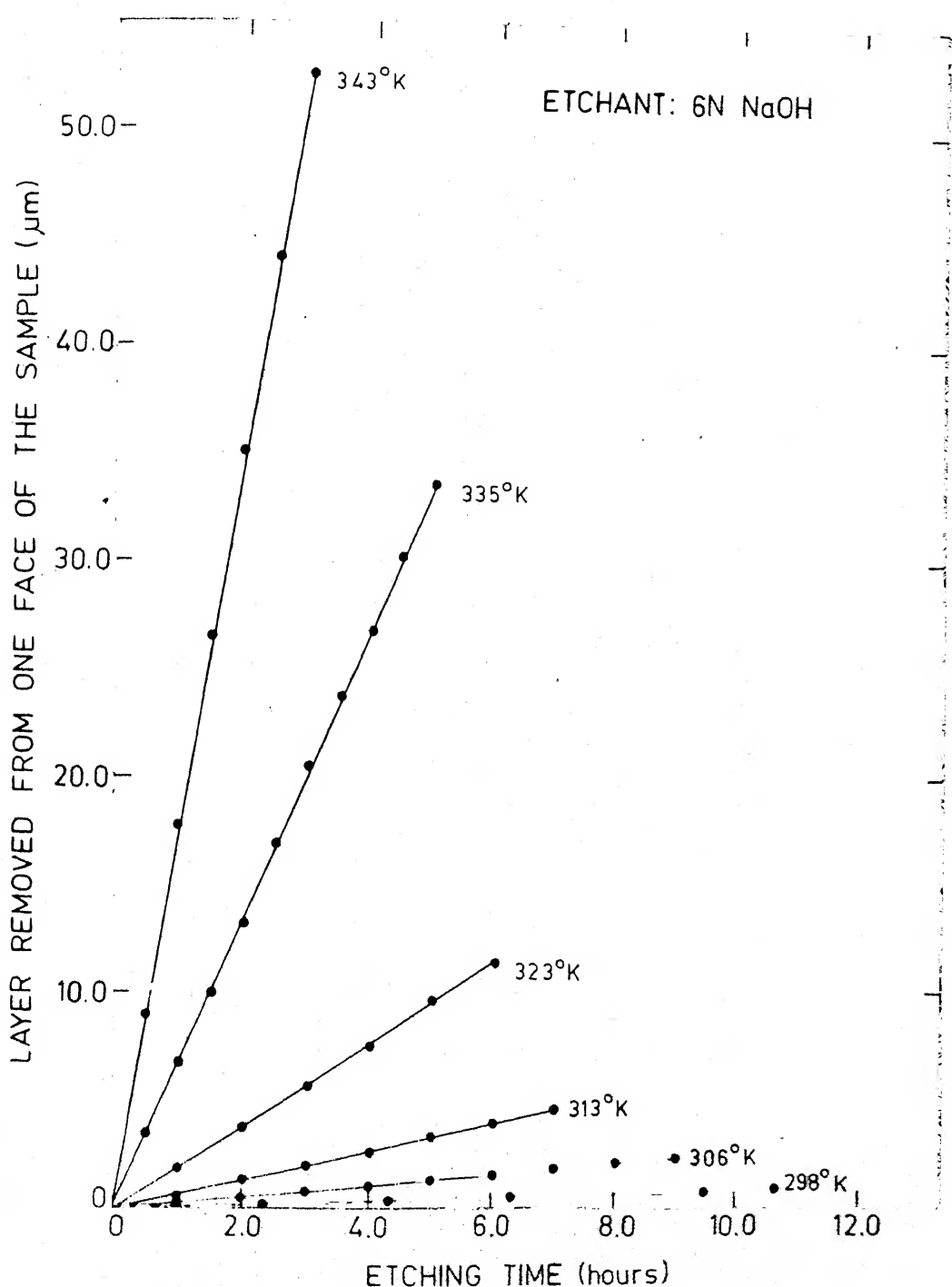
Fig. 3.5. Variation of the thickness of the removed layer as a function of the cumulative etching time at various temperatures.

determined from gravimetric method, are also listed in the
Table - 3.2.

The bulk-etch rates, determined from both methods,
at different temperatures agree well within the experimental
uncertainties.   The accuracy is better in the gravimetric
measurements.   However, the accuracy in the track-diameter
method can be improved by using better micrometer attachment
at high magnification of the microscope.

The temperature dependence of the bulk-etch rate
provides a simple method for determining the activation
energies for bulk-etching of the solid state nuclear track
detectors(SSNTDs).   Several workers [8-9] have tried to
correlate the variation of bulk-etch rate with the temperature
in analogy with a chemical reaction.   For a particular SSNTD
at a given concentration of a particular etchant, the bulk-
etch rate is given by

$$V_B = A \exp(-\frac{E_a}{kT}) \tag{3.2}$$

or
$$\log V_B = \log A - (\frac{E_a}{2.303k}) \frac{1}{T} \tag{3.3}$$

where A is a constant, E_a is the activation energy for bulk-
etching, k is the Boltzmann constant and T is the temperature
in absolute scale.   Thus a plot of $\log V_B$ against $(\frac{1}{T})$ gives
a measure of the activation energy (E_a) as follows:

$$\frac{\triangle (\log V_B)}{\triangle (\frac{1}{T})} = - \frac{E_a}{2.303 \, k}$$

or $\qquad E_a = 0.1986 \left| \dfrac{\Delta(\log V_B)}{\Delta \left(\frac{1}{T}\right)} \right|$ eV

$\qquad\qquad = 0.1986 \times$ (numerical value of slope) eV

The variation of $\log V_B$ as a function of $\left(\frac{1}{T}\right)$ is shown in Fig. 3.6. The continuous curve in the figure is the least square fit. Thus

The slope of the fitted straight line $= -12.32 \pm 0.01$

The activation energy of bulk-etching, $E_a = 2.446 \pm 0.002$ eV

The value of constant, $A = (5.25 \pm 0.35) \times 10^{38}$ μm/hr

These values are useful for calculating the bulk-etch rate at any temperature.

3.4   Rear-Etching Technique

In solid state nuclear track detectors (SSNTDs), the etched particle tracks have two energy dependent parameters for particles of equal mass and charge. The diameter of the etch pit is a function of the radiation damage density along the particle track which is proportional to the specific energy loss rate and hence to the particle energy. This method has been used to study alpha particles [11] and protons [12]. The energy resolution of about 200 keV for alpha particles at about 5.6 MeV and of about 30 keV for protons of energy 2 MeV have been obtained in these studies.
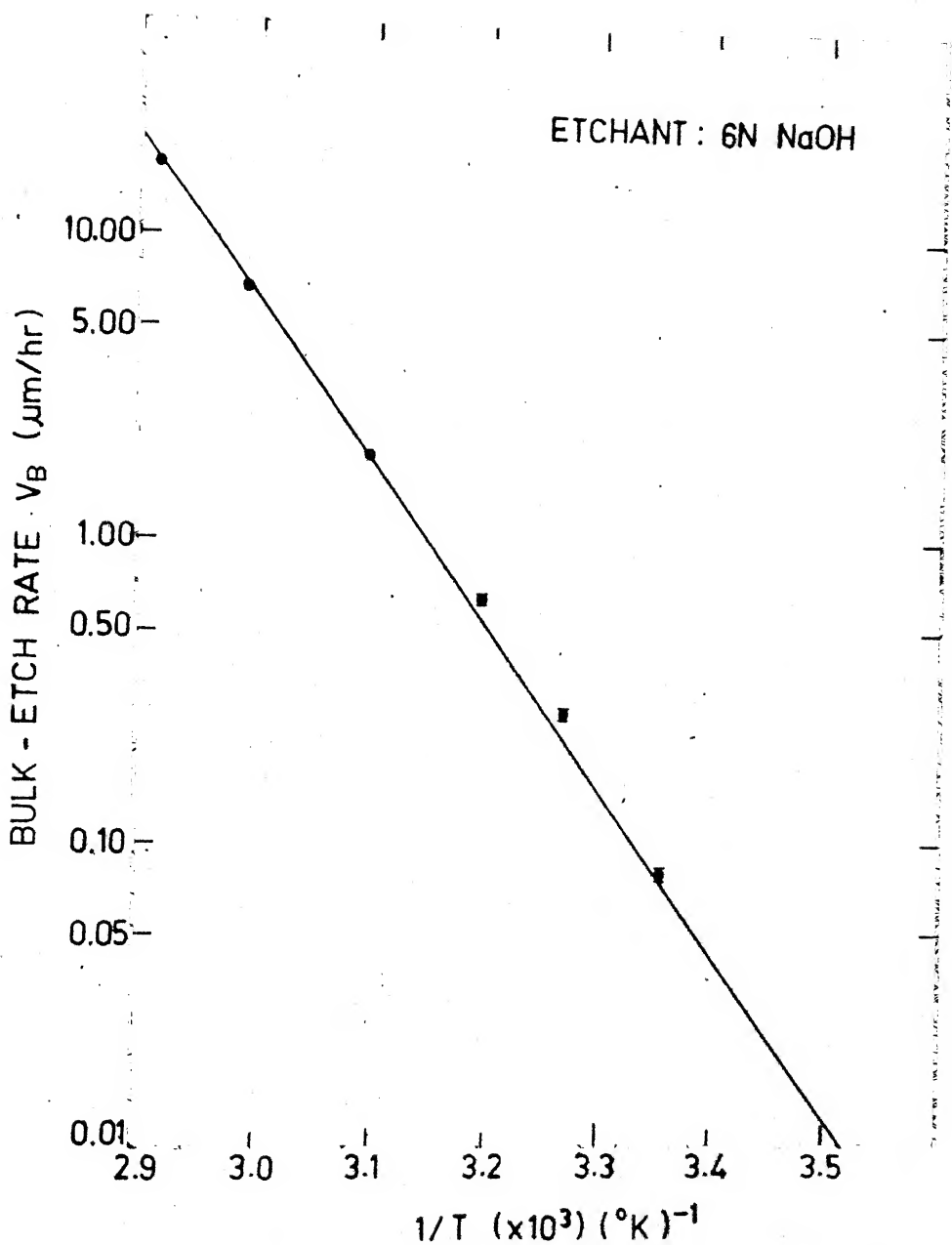
Fig. 3.6 Variation of bulk-etch rate as a function of temperature.

The second track parameter is the track-length which provides the particle range. The particle range directly depends on the energy of the particle. For heavy charged particles such as fission fragments, the track-length can be directly measured with oblique incidence of the particles. This method has long been used to study the heavy charged particles and fission fragments [13]. This method can not be used to study light-charged-particles such as alpha particles since the track-etching rates for these particles are very small resulting in etch pits instead of needle shaped tracks. Recently, a method has been suggested to measure the ranges of alpha particles [6] and hence the alpha particle energy. The principle involved is described below and has been applied to obtain ^{227}Ac alpha energy spectrum as well as to obtain log-range alpha-particle energy spectrum from spontaneous fission of ^{252}Cf.

The surface of the solid state nuclear track detector on which particle is incident is referred as the front surface. When etching of the irradiated sample of the detector is carried out from the opposite surface, it is called rear-etching technique, as illustrated in Fig. 3.7. A normally incident alpha particle enters at A, moves along a straight line path and stops at B inside the detector. The distance AB is thus the range of the particle in the detector material. The solid dots indicate the radiation damage
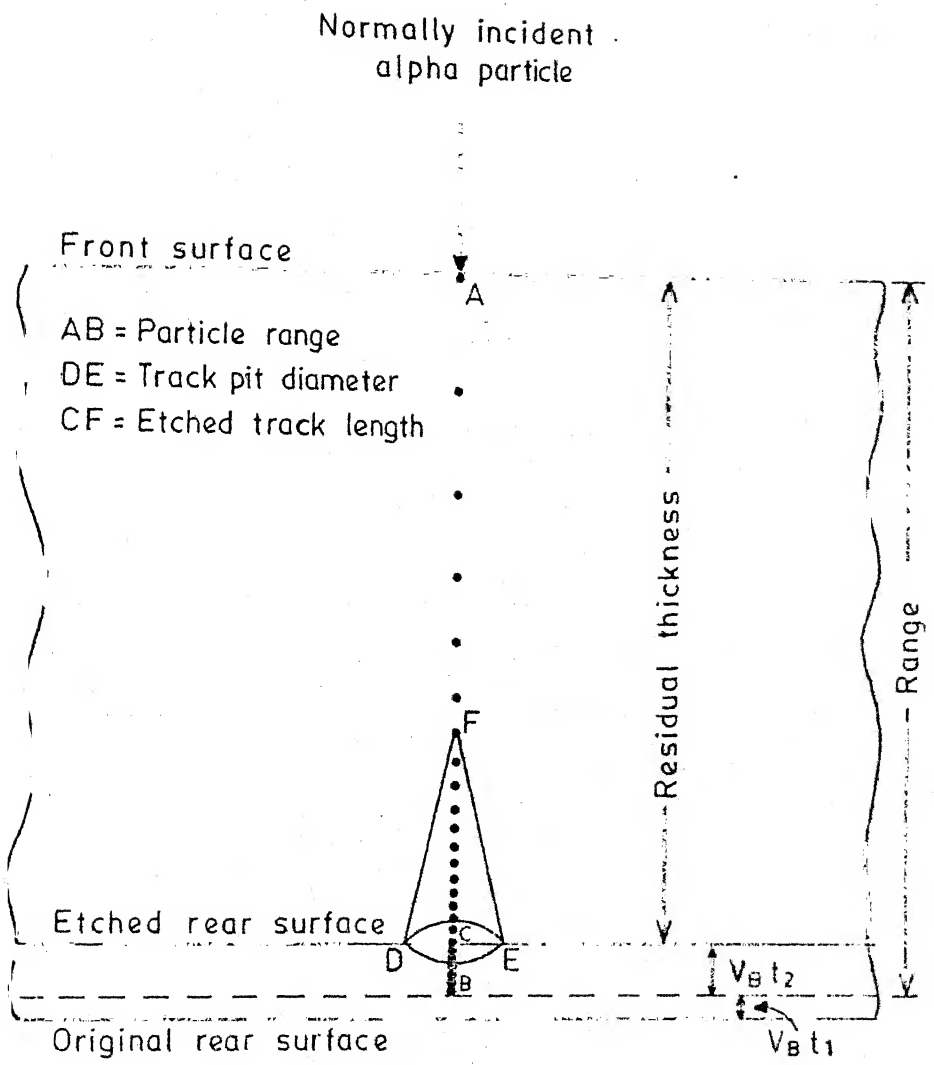
Fig. 3.7. Illustration of rear etching technique.

along the particle path. If V_B is the bulk-etch rate of the detector material, a layer of thickness $V_B t_1$ is removed from the rear in time t_1 by chemical etching and the thickness of the remaining detector material is the range of the particle as in the figure. Now on further etching for a time t_2, another layer of thickness $V_B t_2$ is removed from the rear of the detector sample. Thus

$$\text{Range} = \text{Residual thickness} + V_B t_2.$$

From track-diameter kinetics [7,14] for solid state nuclear track detectors having isotropic bulk-etch rate, the track pit radius is $V_B t_2$. Thus

$$\text{Range} = \text{Residual thickness} + \text{Track pit radius}$$

$$\ldots \ldots \quad (3.4)$$

The energy range, which can be covered by one etching process depends on the size of the range in which the linearity between the track pit radius and the residual thickness is preserved. We irradiated two samples of CN-85 (size: 3 cm x 3 cm) by ^{241}Am (E_α = 5.48 MeV) alpha source as described in the Section 3.2. The particles entered the detector foils vertically. The samples were etched from the rear by floating them on the surface of 6N NaOH solution maintained at $57 \pm 0.5^\circ$C for varying periods of time. After each time of etching, the average track-pit radius over the area of interest was

determined. The variation of track-pit radius as a function of the residual thickness of the sample is shown in Fig. 3.8. The curve shows linearity upto a track-pit radius of about 14 μm and hence the particles having range difference of about 14 μm may be evaluated in a single etching run. This suggests that a layer of about 14 μm can be removed from the rear in a single etching to determine the particle range accurately.

3.5 Application of the Rear-Etching Technique to the Determination of Alpha Energy Spectrum

A cellulose nitrate foil (Kodak CN-85) of 100 μm thickness was irradiated in a vacuum chamber with ^{227}Ac alpha source kept at a distance of 2.5 cms from the foil. The foil was protected from alpha particles with oblique incidence by using a collimator of 2 mm diameter. The collimator also served to confine the area of interest. After irradiation, the detector foil was etched from the rear by floating it in 6N NaOH solution maintained at 57±0.5°C to get 40.5±0.1 μm residual thickness. Then by counting track pits of different diameters, two well separated peaks in the counts versus range (residual thickness plus track pit radius) curve were obtained. Re-etching the foil from the rear to 33.0±0.1 μm residual thickness, two more peaks were obtained in the range spectrum. After etching down to
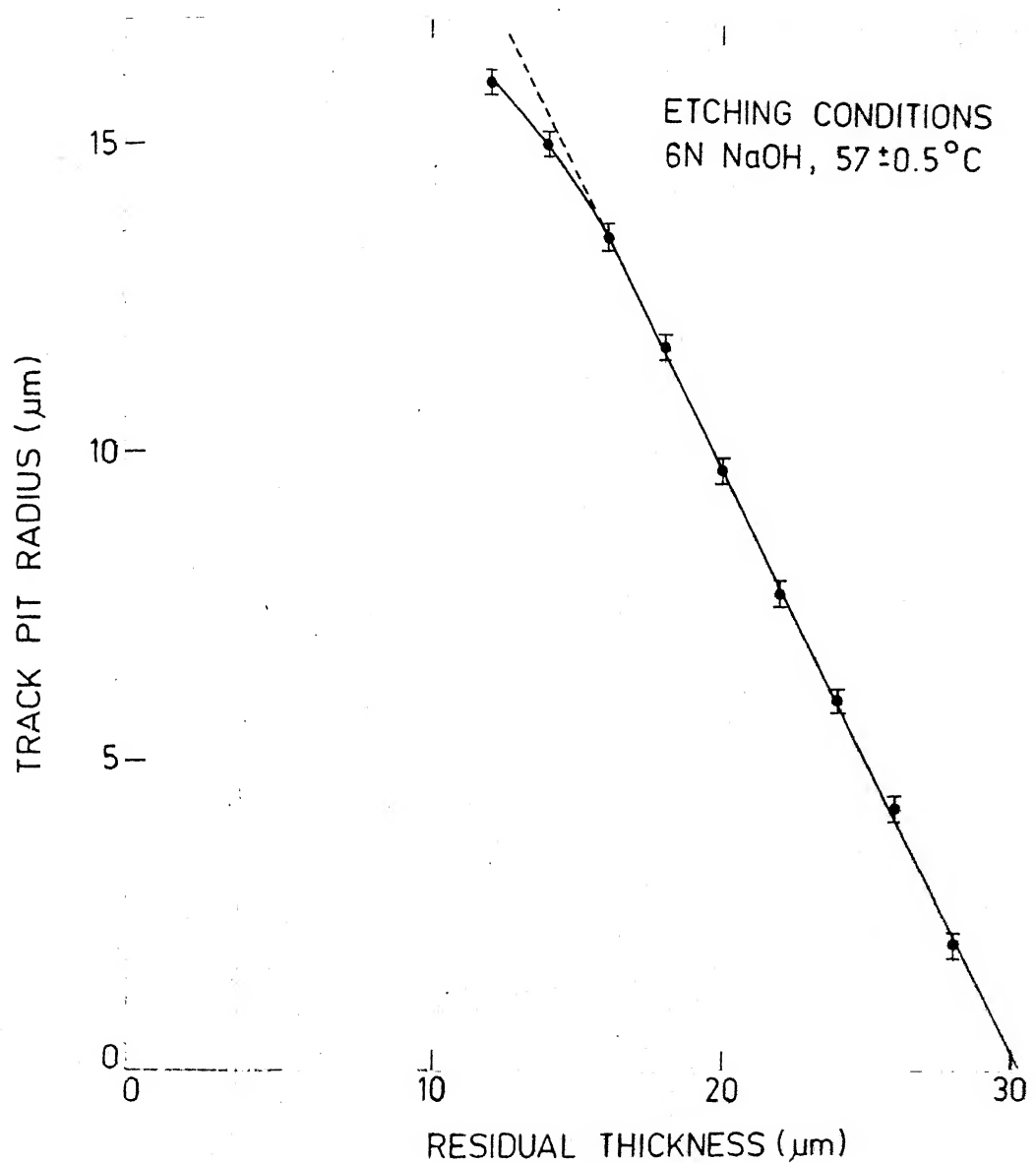
Fig. 3.8. Variation of track pit radius with the residual thickness

26.0±0.1 μm residual thickness the last peak was obtained.
Thus the complete range spectrum of alpha particles from
^{227}Ac was obtained in three phases of etching. In each phase
of etching, the counting of the track pits was restricted to
a maximum diameter of 17 μm to avoid multiple counting. The
multiple counting process is explained in the Section 3.6
below.

Since the CNTD detectors have isotropic bulk-etch
rate, the range of the normally incident alpha particles is
the sum of the residual thickness and the track pit radius
after rear-etching. Fig. 3.9 shows the range spectrum
obtained with ^{227}Ac alpha particle source. The peak energy
conversion was achieved using the range-energy relations [15]
as follows:

$$R(\beta) = (M/Z^2) B_\alpha(B) + MZ^{2/3} C_Z(X) \qquad (3.5)$$

where $\quad B_\alpha(\beta) = \sum_{i=0}^{i=4} a_i \beta^i; \quad C_Z(X) = \sum_{i=0}^{i=7} C_i X^i$

$$X = 137\beta/Z \; ; \quad \beta = v/c$$

where M is the mass, Z is the charge, v is the velocity of
the particle and c is the velocity of light. The values of
the coefficients a_i and C_i are listed in Tables- 3.3 and
3.4 respectively which are taken from reference [15]. The
peak energies thus obtained are given in Table - 3.5 along
with their values obtained with the solid state semiconductor
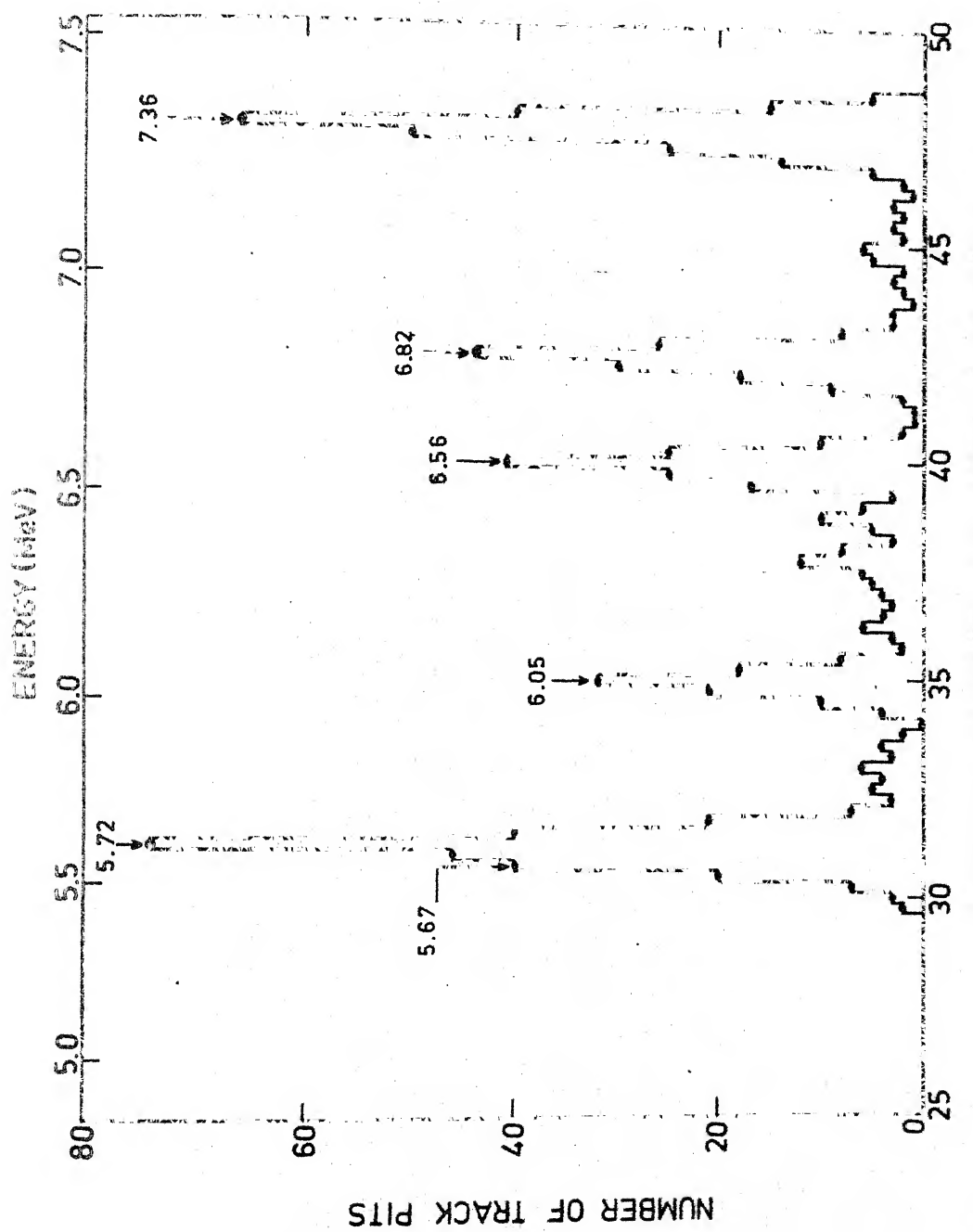
Fig. 3.9 Range and Energy spectrum of ^{227}Ac alpha particles.

Table - 3.3   Values of coefficients a_i for different velocity regions of alpha particles.

Velocity Regions	$i =$ 0	1	2	3	4
$v/c \leq 0.0466$	0	$+0.21194 \times 10^2$	-0.40663×10^4	$+0.30998 \times 10^6$	-0.12886×10^7
$0.0466 \leq v/c \leq 0.0751$	-0.23629×10^2	$+0.18170 \times 10^4$	-0.45198×10^5	$+0.54267 \times 10^6$	0
$v/c \geq 0.0751$	$+0.11162 \times 10^3$	-0.31736×10^4	$+0.18966 \times 10^5$	$+0.25383 \times 10^6$	0

Table - 3.4   Values of C_i coefficients for various X values.

Regions \ i =	0	1	2	3
$X \leq 0.09696$	$+0.13358 \times 10^{-4}$	$+0.77502 \times 10^{-1}$	$+0.18765 \times 10^{1}$	-0.11645×10^{2}
$0.09696 \leq X \leq 0.167325$	$+0.17031 \times 10^{1}$	-0.46673	$+0.85866 \times 10^{1}$	-0.63876×10^{2}
$0.167325 \leq X \leq 0.98947$	$+0.35752 \times 10^{2}$	$+0.54376 \times 10^{-1}$	$+0.24361$	-0.13257×10^{-1}
$0.98947 \leq X \leq 1.5235$	-0.12340	$+0.41447$	-0.12257	-0.13658×10^{-1}
$1.5235 \leq X \leq 2.3570$	$+0.69221 \times 10^{-1}$	$+0.61866 \times 10^{-3}$	$+0.14557$	-0.15669×10^{-1}
$X \geq 2.3570$	$+0.32250$	0	0	0

Table - 3.4 (Contd.)   Values of C_i coefficients for various X values.

Regions \ i =	4	5	6	7
$X \leq 0.09696$	-0.13055×10^{3}	$+0.37257 \times 10^{3}$	$+0.14332 \times 10^{5}$	-0.75066×10^{5}
$0.09696 \leq X \leq 0.167325$	$+0.22983 \times 10^{3}$	-0.32167×10^{3}	$+0.51794 \times 10^{2}$	0
$0.167325 \leq X \leq 0.98947$	-0.43963	-0.50421	-0.17394	0
$0.98947 \leq X \leq 1.5235$	$+0.35379 \times 10^{-1}$	-0.11334×10^{-1}	0	0
$1.5235 \leq X \leq 2.3570$	-0.14669×10^{-1}	-0.28143×10^{-2}	$+0.17831 \times 10^{-2}$	0
$X \geq 2.3570$	0	0	0	0

Table - 3.5   The peak energies and their resolutions.

Peak Energy with Surface Barrier Detector (MeV)	Peak Energy with CN-85 CNTD (MeV)	$FWHM_{(range)}$ (μm)	$FWHM_{(energy)}$ (keV)
5.72 $\pm$ 0.01	5.66 $\pm$ 0.03	0.63	74.1
6.05 $\pm$ 0.01	6.03 $\pm$ 0.02	0.65	72.0
6.56 $\pm$ 0.01	6.56 $\pm$ 0.01	0.68	69.7
6.82 $\pm$ 0.01	6.82 $\pm$ 0.01	0.70	69.4
7.36 $\pm$ 0.01	7.32 $\pm$ 0.02	0.75	69.8

detector. The two values match well.

The full width at half maximum of the range determination, $FWHM_{(range)}$, as a function of energy is shown in Fig. 3.10. As is seen from the figure, the $FWHM_{(range)}$ is directly influenced by the range-straggling which depends on the particle energy. By multiplying the $FWHM_{(range)}$ with the specific energy loss of the corresponding energy, the $FWHM_{(energy)}$ for different peak energies are evaluated and are also shown in Fig. 3.10. Since the range-straggling increases and the specific energy loss decreases with the particle energy, the latter tries to compensate for the influence of range-straggling. At and above $E_\alpha = 6.5$ MeV, the influence of range-straggling is fully compensated by the specific energy loss and hence the energy resolution becomes constant at 70 keV. It is by no means an optimum energy resolution which can be achieved with track detectors. The energy resolution can be improved by using higher magnification microscope with better resolution micrometer attachment. However, the energy resolution obtained is quite adequate for studying the energy spectrum of the long-range alpha-particles emitted in fission which is of main interest to us.

The rear-etching technique was also used to study the long-range alpha-particles emitted from spontaneous fission of ^{252}Cf and is described below.
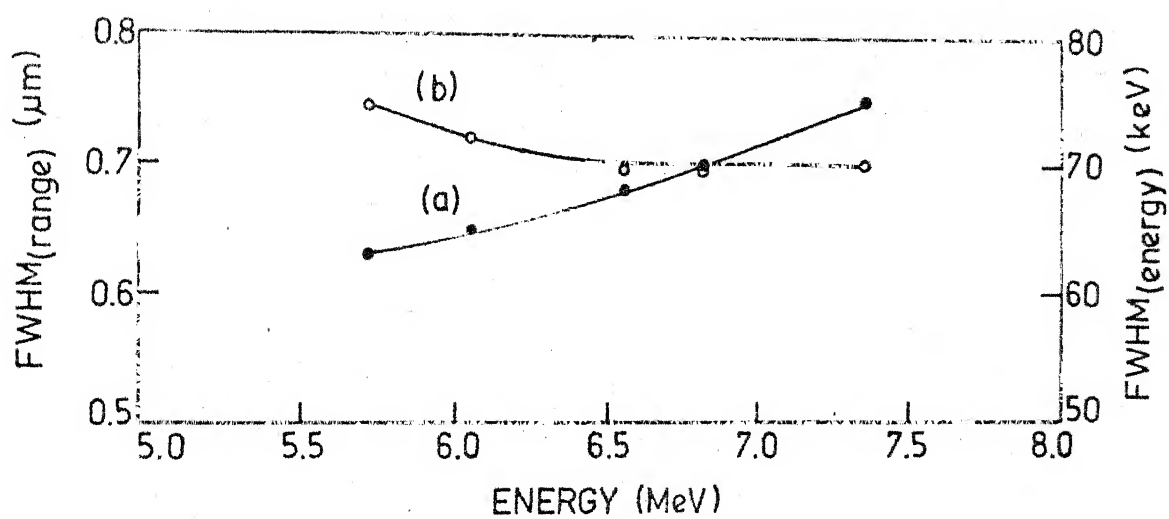
Fig. 3.10. Variation of full width at half maximum (FWHM) with alpha particle energy. (a) FWHM$_{(range)}$ curve and (b) FWHM$_{(energy)}$ curve.

3.6 Study of LRA Emission from ^{252}Cf Spontaneous Fission Using Rear-Etching Technique

To check, whether the rear-etching technique will work satisfactorily for studying long-range alpha-particles or not, a stack of five Kodak CN-85 foils each of 100 μm thickness was used to study the long-range alpha-particles (LRA) emitted from spontaneous fission of ^{252}Cf. An aluminium absorber (8 mg/cm^2 thick) was placed between the ^{252}Cf source and the stack of track detector foils. The thickness of the aluminium foil used was sufficient to absorb the natural alphas and the fission fragments from the source thus preventing them from reaching the detector foils. The detector foils subtended 2π-solid angle to the source. After twenty four hours of irradiation, each foil was etched from the rear by floating the foil in 6N NaOH solution maintained at $57\pm0.5^{\circ}$C. The etching and counting of each foil was completed in several steps. A layer of about 14 μm was removed from the rear of the foil in each step of etching.

The normally incident alpha particles produce circular track pits on rear-etching and can be used directly for range determination. The range determination from elliptical track pits is very complicated and therefore the circular track pits of normally incident alpha particles have been used to determine the range of long-range alpha-particles in the present measurements.

After each removal of 14 µm layer, the number of circular pits having 1 µm $\leq$ radius $\leq$ 14 µm and total track pits (circular plus elliptical) were determined. The counting was carried out at magnification of 1600 using an Ergaval microscope having micrometer attachment with it. The least count at this magnification was 1 µm. The maximum track pit radius limit was put to avoid multiple counting. Since beyond 14 µm track radius, the track pit radius is non-linear, the chances of counting the same track pit more than once pose a serious problem. By restricting the counting upto track pit radius of 14 µm, the above difficulty can be overcome.

Repeated etching and counting finally left each foil of thickness $\sim$ 16 µm. Final etching was then carried out from the front. The circular etch pits having 2 µm $\leq$ diameter $\leq$ 6 µm were then counted in each foil.

Completing etching and counting for each foil, the range spectrum was constructed. The range spectrum is then corrected for aluminium absorber by adding equivalent thickness of cellulose nitrate track detector ($\sim$ 40 µm) to the origin of the spectrum. The corrected range spectrum is shown in Fig. 3.11. The energy spectrum is shown in Fig. 3.12. The continuous curve in the figure is the least squares Gaussian fit to the experimental points. The average energy ($\bar{E}_\alpha = 15.52 \pm 0.15$ MeV) and the width

147
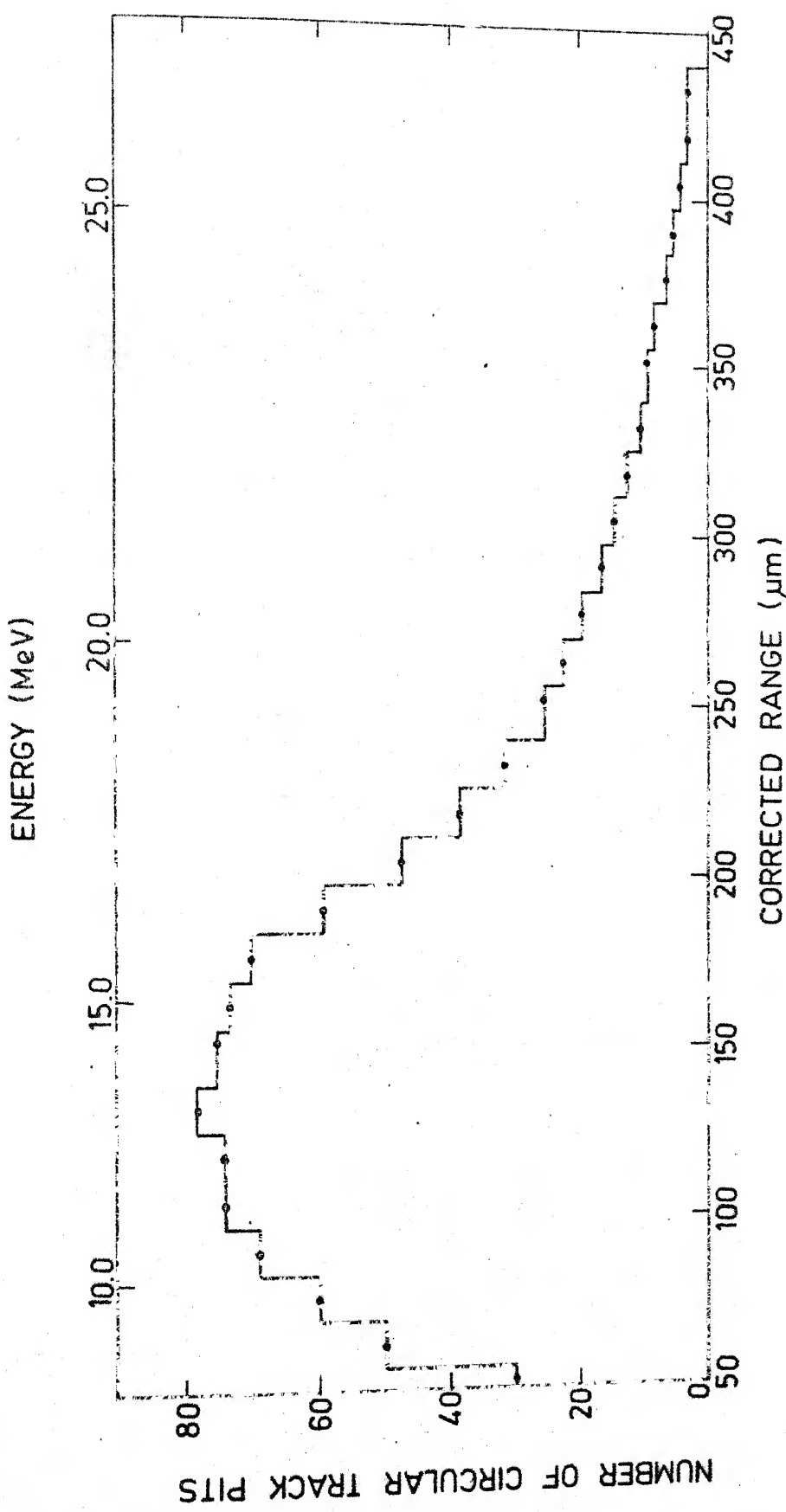
Fig. 3.11. Range spectrum of long range alpha particles emitted from ^{252}Cf spontaneous fission.
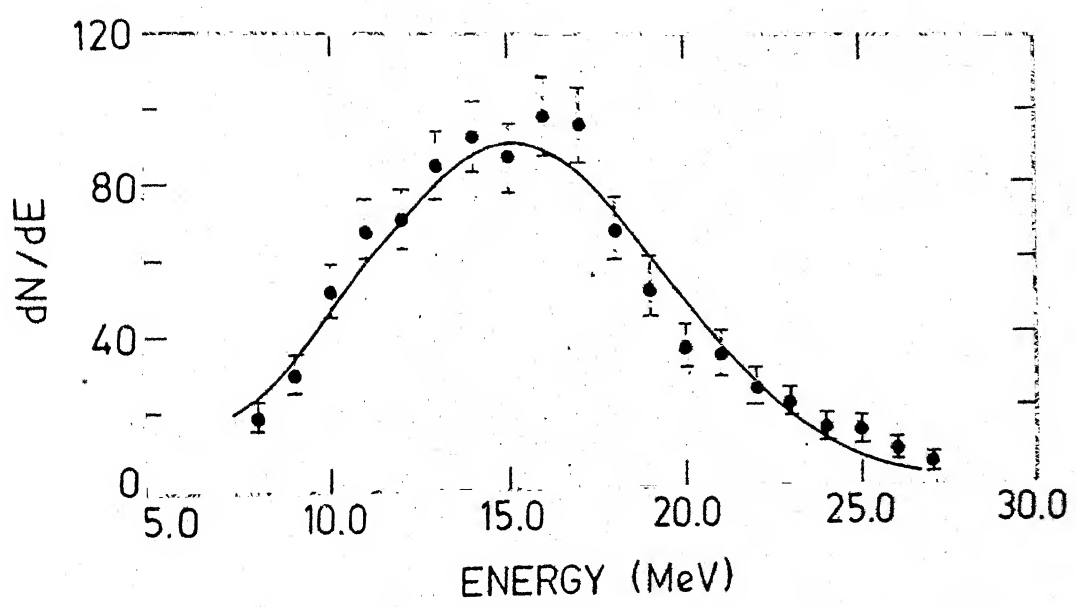
Fig. 3.12   LRA energy spectrum.

$(\sigma_{E_\alpha} = 4.48 \pm 0.05$ MeV) are determined from the Gaussian fit which are very close to their known values [16].

From the total revealed track pits in all the five foils, it has been estimated that one LRA particle is emitted for about 256 ± 19 fissions. The fission yield was separately determined using a solid state semiconductor detector. The above value is close to the accepted value (299 ± 18) of LRA probability in ^{252}Cf spontaneous fission.

The rear-etching technique was, later, used to study the fine variation in the LRA yield and energy distributions with neutron energy for ^{235}U fission in the neutron energy region from thermal to 500 keV. The details of these studies are given in the next Chapter.

REFERENCES

[1] D.A. Young, Nature, 182 (1958) 375.

[2] E.C.H. Silk and R.S. Barnes, Phil. Mag., 4 (1959) 970.

[3] P.B. Price and R.L. Fleischer, Ann. Rev. Nucl. Sci., 21 (1971) 295.

[4] R.L. Fleischer, P.B. Price and R.M. Walker, ''Nuclear Tracks in Solids'', University of California Press, Berkley, 1975.

[5] H.B. Lück, Nucl. Instr. and Meth. 114 (1974) 139.

[6] H.B. Lück, Nature, 249 (1974) 750.

[7] G. Somogyi and S.A. Szalay, Nucl. Instr. and Meth., 109 (1973) 211.

[8] G.E. Blanford, Jr., R.M. Walker and J.P. Wefel, Rad. Eff. 3 (1970) 267.

[9] W. Enge, K. Grabisch, L. Dallmeyer, K.-P. Bartholomä and R. Beanjean, Nucl. Instr. and Meth. 127 (1975) 125.

[10] W.T. Crawford, W. Desorbo, and J.S. Humphrey, Nature, 220 (1960) 1313.

[11] G. Somogyi, B. Schlenk, M. Vornagy, L. Mesko and A. Valek, Nucl. Instr. and Meth. 63 (1968) 189.

[12] H.B. Lück, Nucl. Instr. and Meth. 119 (1974) 403.

[13] K.K. Dwivedi and S. Mukherji, Nucl. Instr. and Meth. 161 (1979) 317.

[14] K.K. Dwivedi and S. Mukherji, Nucl. Instr. and Meth. 159 (1979) 433.

[15] J. Tripier, G. Remy, J. Ralarosy, M. Debeauvais, R. Stein and D. Huss, Nucl. Instr. and Meth. 115 (1974) 29.

[16] G.K. Mehta, J. Poitou, M. Ribrag and C. Signarbieux, Phys. Rev. C7 (1973) 373.

CHAPTER IV

STUDY OF LRA EMISSION IN P-WAVE NEUTRON INDUCED FISSION OF ^{235}U USING A CELLULOSE NITRATE TRACK DETECTOR

4.1 Introduction

There have been various conjectures about the extent to which the properties of the nucleus at the saddle point influence the various characteristics of the fission process such as the fission fragment angular distribution, mass distribution, kinetic energy distribution, prompt neutron emission, prompt gamma ray emission and long-range alpha-particle emission. Krishnarajulu et al. [1,2] carried out measurements on the long-range alpha-particle (LRA) accompanied fission of ^{235}U ($J^\pi = 7/2^-$) and ^{239}Pu ($J^\pi = 1/2^+$) at neutron energies in the range from thermal to 1 MeV. Their results showed a structure in the LRA yield at neutron energies around E_n = 200 keV. At neutron energies,

$E_n \geqslant 500$ keV, the LRA yield was observed to be equal to that of thermal neutrons. Sharma et al. [3] employed a semiconductor $\triangle$E-E detector telescope for particle identification (as described in the Chapter II) and determined the yields and energy distribution parameters (average energies and widths) for protons, tritons and alpha particles emitted from neutron induced fission of ^{235}U at neutron energies in the energy region from thermal to 700 keV. An increase of about 20-25 % was observed in the alpha particle yield at neutron energies in the neutron energy interval 120 keV$\leqslant E_n \leqslant 350$ keV as compared to that of thermal neutrons.

In the above mentioned studies [1-3], the measurements were carried out at few neutron energies using reasonably thick neutron targets. The observed yields are, therefore, expected to be an average over a wide neutron energy region. To see whether there is any fine structure in the LRA yield at neutron energies around $E_n = 200$ keV, further experiments are needed with better neutron energy resolution.

Radiation damage in the semiconductor detectors at high neutron flux makes the use of these detectors very uneconomic in the study of LRA accompanied fission of ^{235}U induced by neutrons. Since the solid state nuclear track detectors (SSNTDs) are insensitive to neutrons, the combination of a cellulose nitrate track detector (CNTD)

with rear-etching technique offers an ideal detector [4] for alpha particles in such studies.

The rear-etching technique was developed for alpha particle detection using a cellulose nitrate track detector (Kodak CA 80-15), which is described in the Chapter III.

Present measurements have been carried out on the LRA emission in neutron induced fission of ^{235}U at several neutron energies in the neutron energy region from thermal to 500 keV having small neutron energy spreads. An Argon gas filled thin ionization chamber was used for fission fragments detection along with the cellulose nitrate foils. for alpha particle detection in these measurements.

Section 4.2 describes the experimental setup used. The procedure of data analysis is given in the Section 4.3. The results are presented in the Section 4.4. The possible errors in these results are briefly described in the Section 4.5. The results are discussed in the Section 4.6 and the conclusions based on the present results are summarized at the end of the Chapter.

4.2 Experimental Setup and Procedure

The measurements were carried out with the 2 MV Van de Graaff accelerator at the Indian Institute of Technology, Kanpur. The details of the beam transport system, the BF3 neutron counter and the neutron target holder are given in

the Section 2.4.

Neutrons of energies; thermal, 125, 155, 185, 210, and 240 keV were produced by the ^{7}Li(p,n)^{7}Be reaction [5]. The neutron energy spread was calculated using energy loss and angular spread considerations and it was found to be about 10 keV at above mentioned neutron energies. The ^{235}U fissile target intercepted the neutron beam in a cone of angle 30°. The lithium targets of about 5 keV thickness to 2 MeV protons were prepared by vacuum evaporation of lithium metal onto thick copper backings. Thermal neutrons were obtained by interposing a 5 cm thick paraffin block between the neutron producing target and the fission chamber.

The T(p,n)^{3}He reaction [6] was used to produce neutrons of energies, 365 keV and 480 keV. The tritium targets used in these measurements were obtained from the Isotope Division, BARC, Bombay. The neutron energy spreads at these neutron energies were estimated to be about 40 keV. The method of energy spread calculation for tritium targets is described in the Section 2.4.

The fission target used was the same as for the measurements discussed in Chapter II. The target formed the Cathode and an aluminium foil (of thickness ~7 mg/cm^2) formed the collector of the ionization chamber. The thickness of the aluminium collector was such as to stop the natural alphas and fission fragments and allow only

long-range alpha-particles to pass through to get registered in the stack of five CNTD foils. Ionization chamber was filled with pure Argon gas. The schematic diagram of the fission chamber is shown in Fig. 4.1 along with the electronic circuit used to process the fission fragment pulses. The amplified pulses were fed into the single channel analyzer (SCA) as well as into the multi-channel analyzer. The discriminator on the single channel analyzer was set to cut off the natural alphas ($\sim$6 MeV). The SCA output was counted in a scaler which was used to monitor the fission count rate.

A stack of five CNTD foils was mounted on the back of the aluminium collector to detect the long-range alpha-particles. After filling Argon gas in the fission chamber, it was placed near the neutron producing target such that the fissile target subtended a cone of angle about 30°. The SCA, the multi-channel analyzer (MCA) and the neutron beam were started simultaneously. After irradiating the foils for few hours, the neutron beam, SCA and MCA were stopped at the same time. These foils were taken out of the chamber at the end of the run and were placed in a cold place to avoide any type of annealing of the alpha tracks.

A new set of CNTD foils was mounted for each neutron energy measurement. The total of eight different neutron energy runs were taken in this manner.
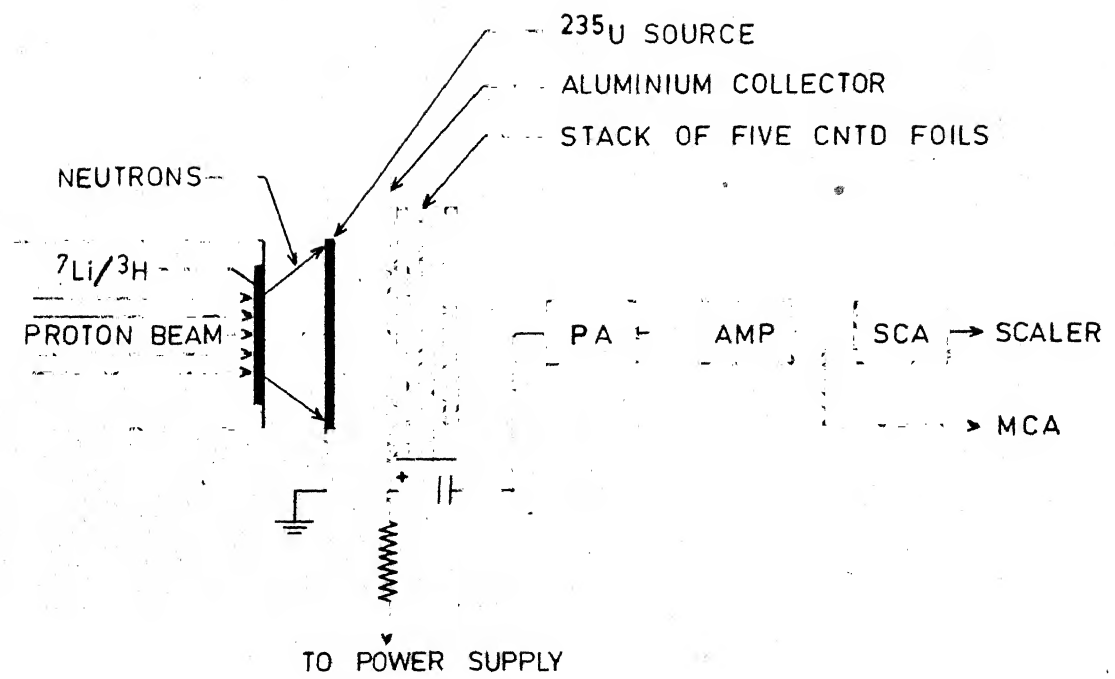
Fig. 4.1. Schematic diagram of the ionization chamber and electronics used

The proton current used was about 15 μA. About 10^6 total fission counts were recorded for each neutron energy run. The irradiated CNTD samples were then analysed in the following manner.

4.3 Data Analysis

A stack of five foils (each of thickness 100 μm) of cellulose nitrate track detector was irradiated in each neutron energy run. Each foil was etched from the rear in several steps, a layer of thickness about 14 ± 0.5 μm was removed in each step of etching. Etching was carried out by floating the foil in the 6N NaOH solution maintained at 57±0.5°C in a thermostatic water bath. In each step of etching, fresh solution of etchant was taken. As described in Section 3.4, the circular etch pits of radius ≤ 14 μm give directly the range of the normally incident alpha particles, the total number of circular etch pits having 1 μm ≤ etch pit radius ≤ 14 μm was determined after removing a layer of ∼14 μm. the average range of these alpha particles was estimated to be about (100(n-1) + Residual thickness of the foil + 7) μm, where n is the serial number of the foil numbered from the front. The foil was rear-etched again to remove another layer of thickness 14±0.5 μm. The total number of circular etch pits having 1 μm ≤ etch radius ≤ 14 μm was again determined and the corresponding average range, as

described above, was estimated. The measurements were made
with an Ergaval (VEB Carl Zeiss, Jena) microscope using a
magnification of 1600. At this magnification, the small
division of the eye piece micrometer was 1 micron. The lower
limit of the diameter was due to the limitation of the
magnification of the microscope while upper limit was based
on the linear increase of the etch pit radius. Beyond 14 μm,
the increase in the radius was not linear.

The rear-etching and counting were repeated until
the thickness of the remaining foil was about 16 μm. The
foil was then etched from the front for about one hour.
The total number of etch pits having 2 μm $\leqslant$ diameter $\leqslant$ 6 μm
was then determined. The average range of these alpha
particles is $(100(n-1)+8)$ μm. After completing the etching
and the counting for each foil, the range spectra for all the
runs were constructed. These range spectra were then converted
into the energy spectra. The procedure of range-energy
conversion is described in the Chapter III (Sections 2.5 and
2.6).

Since alpha particles were incident at various angles
on the surface of the CNTD foil, there were circular as well
as elliptical etch pits on etching of each foil. The total
etch pits (circular + elliptical etch pits) were counted in
each foil at the end of its final etching. The total number
of etch pits revealed in the five foils corresponding to

each neutron energy run was used to determine the long-range
alpha-particle yield at various incident neutron energies.

4.4 Results

The energy spectra of long-range alpha-particles
(LRA) for thermal run and for various fast neutron energy
runs are shown in Fig. 4.2. The continuous curves in the
figure are the least-squares fits of the energy spectra to
the Gaussian shapes.

The most probable energy ($\bar{E}_\alpha$) and the width (σ_{E_α}),
for various incident neutron energies, were obtained from
the least-squares Gaussian fits. These values are listed in
the Table - 4.1 and are shown in the Fig. 4.3. The values
of $\bar{E}_\alpha$ and σ_{E_α} showed some fluctuations.

The LRA yields at various neutron energies are also
listed in the Table - 4.1 after normalizing the observed
yield for the thermal neutron induced fission to the known
[7] absolute value of 2×10^{-3} per fission. These values are
shown in Fig. 4.4. The yields are obtained from the total
revealed etch pits in the five foils corresponding to each
neutron energy run. The LRA yield at neutron energies,
$E_n \geq 120$ keV, is observed to be higher as compared to the
yield for thermal neutron fission. The yield at neutron
energies, 150 keV $\leq E_n \leq$ 250 keV, is about 50 % higher as
compared to that of thermal neutrons. The yield at neutron
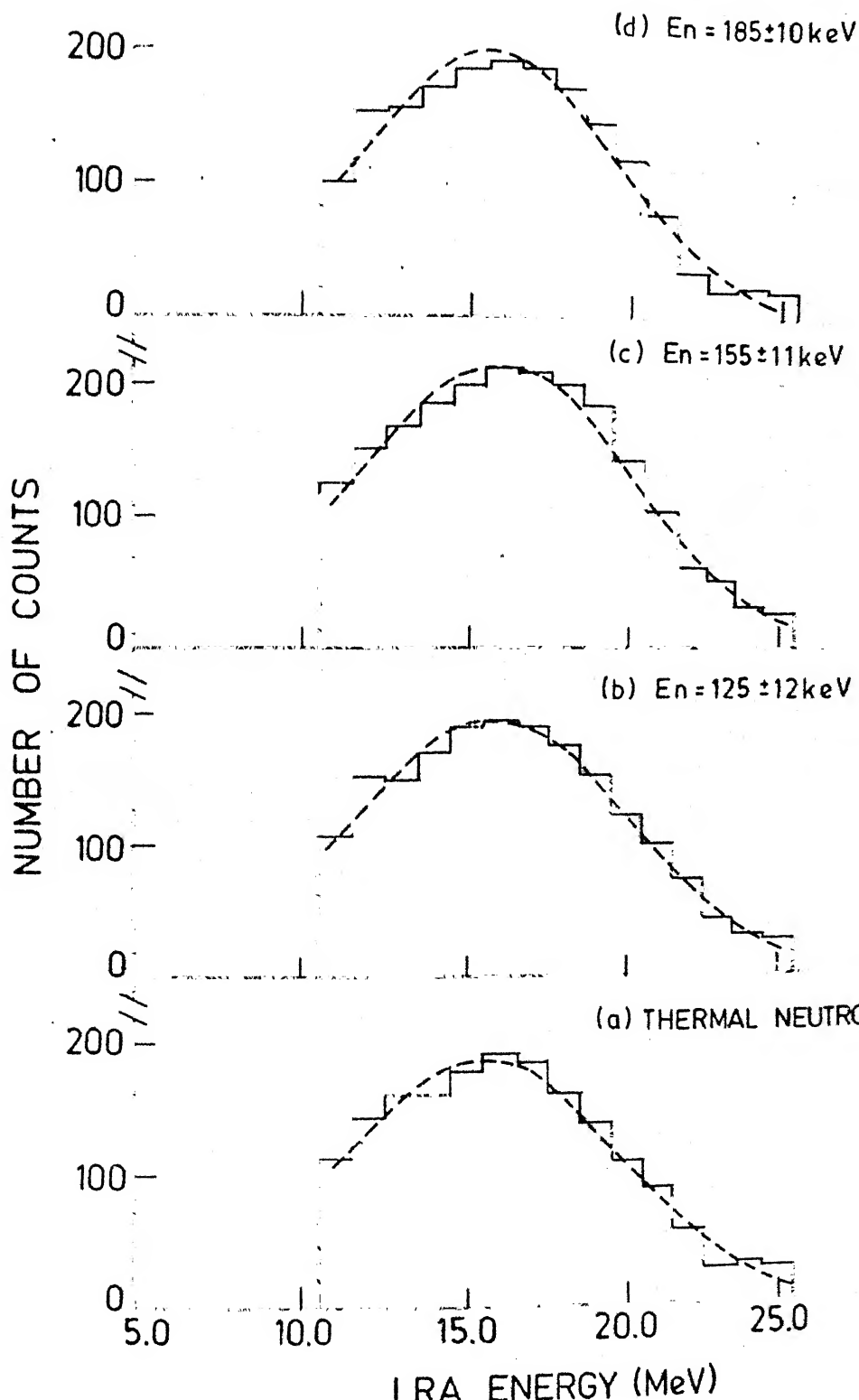
Fig. 4.2. The LRA energy spectra for various incident neutron energies.
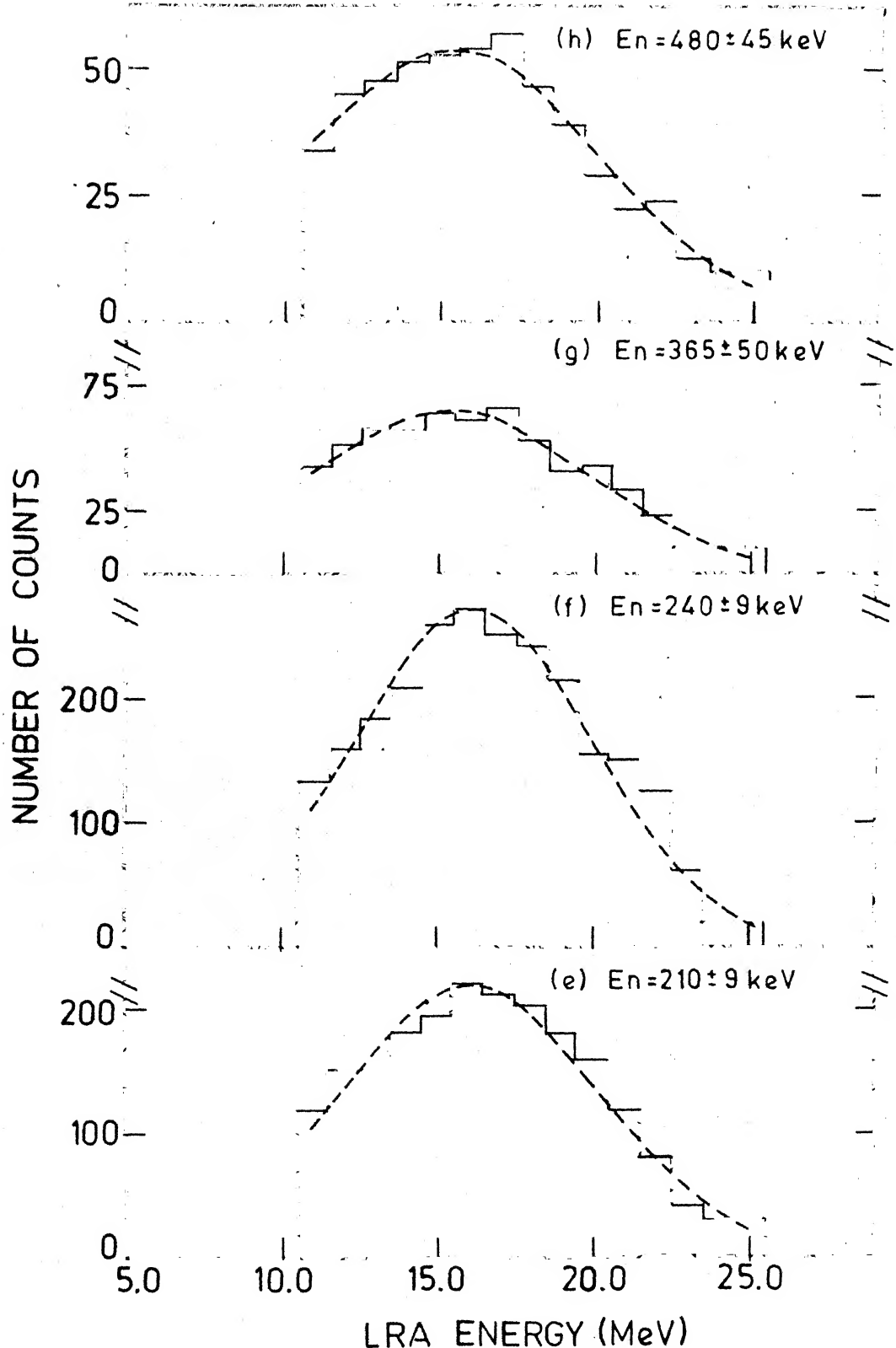
Fig. 4.2. (contd.) The LRA energy spectra for various incide
neutron energies.

Table - 4.1   LRA yield, most probable energy ($\bar{E}_\alpha$) and standard deviation (σ_{E_α}) for various neutron energies.

Neutron energy (keV)	LRA yield ($\times 10^{-3}$)	LRA most probable energy (MeV)	Width (MeV)
THERMAL	2.00 ± 0.048	15.42 ± 0.12	4.28 ± 0.03
125 ± 12	2.48 ± 0.046	15.77 ± 0.10	4.37 ± 0.03
155 ± 11	2.96 ± 0.044	15.78 ± 0.10	4.25 ± 0.025
185 ± 10	2.96 ± 0.046	15.50 ± 0.09	3.88 ± 0.023
210 ± 9	3.04 ± 0.044	16.05 ± 0.093	4.18 ± 0.024
240 ± 9	2.82 ± 0.042	16.12 ± 0.08	3.86 ± 0.02
365 ± 50	2.58 ± 0.080	15.21 ± 0.18	4.52 ± 0.054
480 ± 45	2.22 ± 0.060	15.23 ± 0.19	4.81 ± 0.061
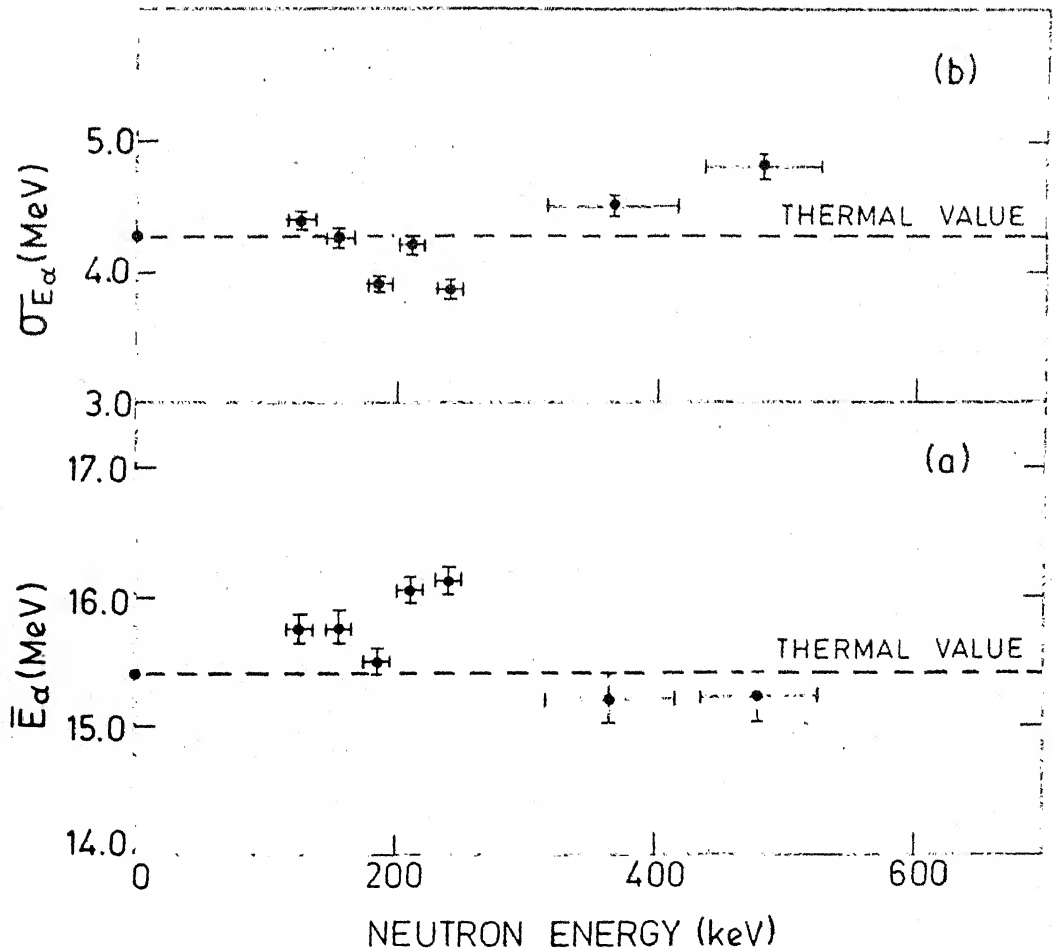
Fig. 4.3. Variation of (a) the most probable LRA energy ($\overline{E}\alpha$) and (b) standard deviation (σ_{E_α}) with incident neutron energy.
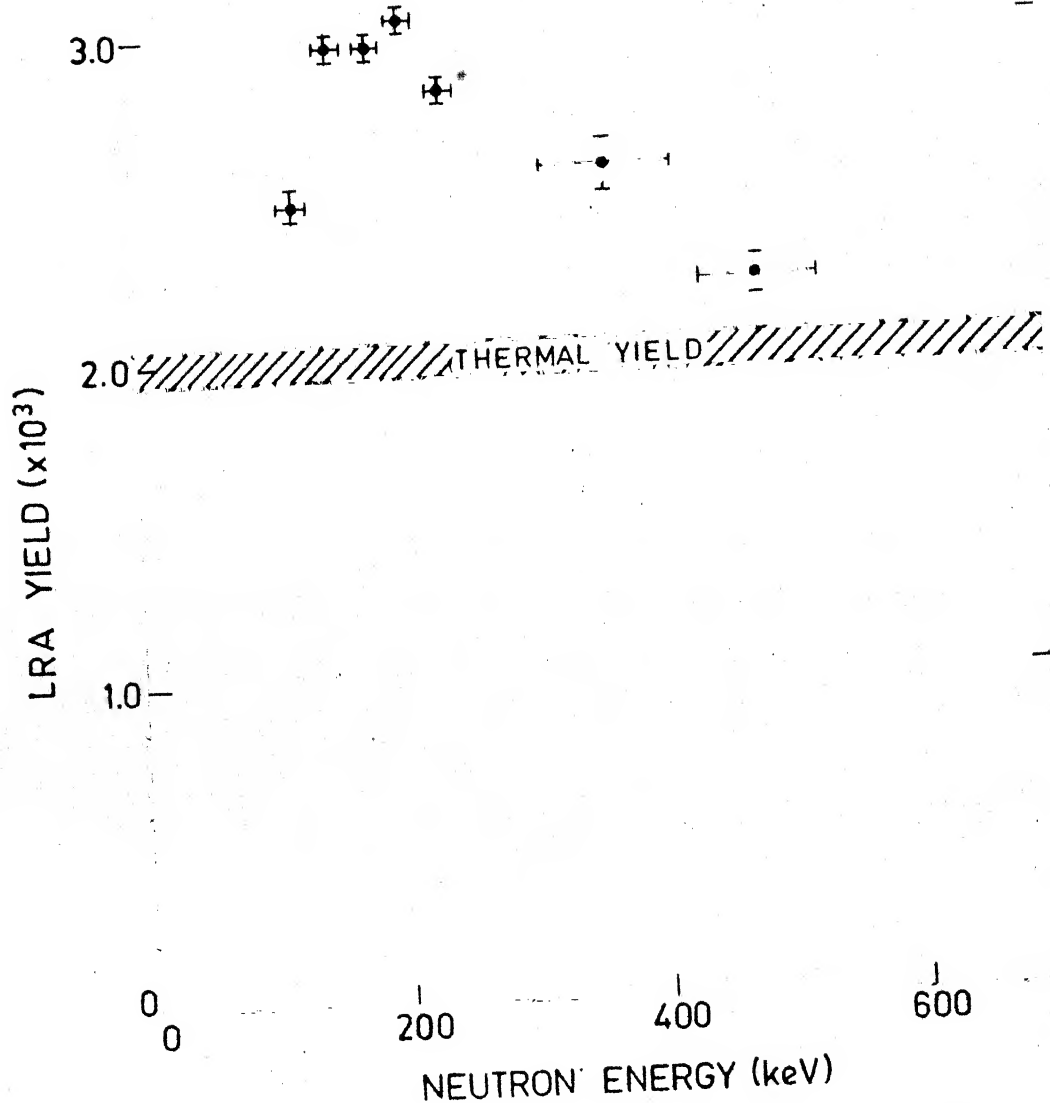
Fig. 4.4. Variation of LRA yield with incident neutron energy.

energies above 250 keV decreases and tends towards its thermal value.

4.5 Errors

(a) Error due to counting

The error was estimated by irradiating a cellulose nitrate track detector foil (size: 3 cm x 3 cm) with alpha particle source of known activity (^{241}Am; E_α = 5.48 MeV) for a definite interval of time. After etching the foil for about two hours in NaOH(6N) solution at $57\pm0.5^\circ$C, counting of the total etch pits was carried out three times. The reproduction of the total number of etch pits was observed to be limited by about 3 % due to the counting mistakes. The etching was carried out from the front of the foil by floating the foil in the solution. Thus due to the reproducibility of the counts, the error in the LRA yields is about 3 % .

(b) Statistical errors

The statistical errors in the LRA yields lie between 1.5 % to 2.5 % in the present measurements.

(c) Contribution due to the contamination of thermal neutrons in the keV neutron energy runs

Apart from errors due to counting and statistics, there was some contribution in the LRA yield due to the

contamination of thermal neutrons in the keV neutron flux.
Measurements (as described in the Section 2.9) indicated
that the ratio of thermal neutron flux to keV flux is about
10^{-4} in the present geometry. There are about 4 % of the
total fission events produced due to these contaminations
which produce an overall discrepencies of about 1 % - 1.5 %
in the LRA yield at various neutron energies in the present
measurements. This is within the experimental error.

4.6 Discussions

It is seen from the Fig. 4.3 that there is no
significant change in the values of most probable LRA
energy $(\bar{E}_\alpha)$ and the standard deviation (σ_{E_α}) in the fast
neutron induced fission as compared to their values in the
thermal neutron induced fission. These results in conjunction
with previous work [1-3] may prove to be useful in establishing
that the excitation energy dependence of the LRA energy
distribution is very weak. This also indicates that the
changes in scission configuration do not get reflected in the
energy spectra of different light-charged-particles.

Fig. 4.4 shows the variation of LRA yield with the
incident neutron energy. It is seen from the figure that
the yield increases with the incident neutron energy above
120 keV. At neutron energies in the range from 150 keV to
250 keV, the yield shows an increase of about 50 % as

compared to the yield for thermal neutron fission. At higher neutron energies (above 250 keV), the yield shows a decrease trend. It decreases slowly towards the thermal value.

In the earlier measurements [1,3] also, the yield of alpha particles at neutron energies around E_n = 200 keV showed an increase of about 20 % as compared to that of the thermal neutron induced fission. In these measurements, the thick neutron targets were used and therefore the neutron energy spreads were much larger as compared to the energy spreads in the present measurements, the yields were the averaged values over the large neutron energy window. Krishnarajulu et al. [1] also observed the LRA yield at neutron energies in the interval from 600 keV to 1020 keV and found that the yield becomes equal to that of thermal neutrons in this energy region. The yields at higher neutron energies (E_n > 1 MeV) were also observed [8] and it was found that the yield is the same as that of thermal neutrons.

Since the change in the excitation energy of the compound nucleus at 200 keV neutron energy is not very large as compared to that of thermal neutrons, the increase in the LRA yield at neutron energies around E_n = 200 keV can not be associated with the excitation energy of the fissioning nucleus. Moreover, the LRA yield decreases with the incident neutron energy at neutron energies above E_n = 250 keV and

upto about 500 keV. Beyond 600 keV neutron energy, the LRA yield [1,8] was observed to be the same as the thermal value. These studies [1,8] emphasized that the LRA yield dependence on the excitation energy of the compound nucleus is very weak.

In the thermal neutron induced fission ($\ell = 0$, s-wave fission) of $^{235}U(7/2^-)$, the states accessible to the fissioning nucleus at the saddle point are the negative parity states, namely 3^- and 4^-. In the fast neutron induced fission of ^{235}U, the higher partial waves such as p, d, f...... etc. also contribute to the fission cross section along with the s-wave and therefore the states of both parities (negative and positive) are accessible to the fissioning nucleus at higher incident neutron energies. The contributions of different partial waves to the total fission cross section depend upon the incident neutron energy and the different at different incident neutron energies. At neutron energies in the interval from 120 keV to 350 keV, the contribution of p-wave fission to the total fission cross section is about 60 % [9,10] and hence the most accessible states to the fissioning nucleus at the saddle point are the positive parity states, nemely 2^+, 3^+, 4^+ and 5^+. Since the positive parity states lie about 0.6 MeV lower than the negative parity states, the extra available energy at the saddle point in the p-wave fission can go into the degrees of freedom such as the deformation, fragment kinetic energy, fragment excitation

energy or into the light-charged-particle emission. The increase in the neutron yield at these energies [11] indicated that the extra available energy may go into the fragment excitation energy. The increase in the LRA yield in the above mentioned interval indicates that the extra available energy in the p-wave fission may also go into the long-range alpha-particle emission and hence the variation may be associated with the increase in the relative number of fission proceeding via the even parity states populated by p-wave interaction in this energy interval. At 500 keV, the p-wave fission contribution is about 35 % of the total fission cross section while the d-wave contribution is the same as that of s-wave fission. The contribution of higher partial waves is less than 10 % of the total fission cross section. These contributions compensate each other in the LRA yield such that the yield approaches to that of thermal neutrons.

The most probable energy and the standard deviation of long-range alpha-particles emitted in neutron induced fission of ^{235}U do not change with the incident neutron energy in the energy interval studied. This indicates that the excitation energy dependence of the LRA energy distribution is very weak and hence the stretching of the fissioning nucleus at the scission point remains the same no matter what its excitation energy is and which state of the

transition nucleus contributes more. On the other hand, the transition state of the fissioning nucleus at the saddle point seems to play a major role in deciding the long-range alpha-particle emission probability in the fission process.

REFERENCES

[1] B. Krishnarajulu, G.K. Mehta, R.K. Choudhury,
     D.M. Nadkarni and S.S. Kapoor, Pramäna. 8 (1977) 315.

[2] B. Krishnarajulu, S. Sen and G.K. Mehta, J. Phys. G :
     Nucl. Phys., 5 (1979) 319.

[3] S.C.L. Sharma, G.K. Mehta, R.K. Choudhury,
     D.M. Nadkarni and S.S. Kapoor, Accepted for Publication
     in Nucl. Phys.

[4] S.C.L. Sharma and G.K. Mehta, Accepted for Publication
     in Nucl. Instr. and Meth. (In Press).

[5] J.H. Gibbons and H.W. Newson, Fast Neutron Physics
     (J.B. Marion and J.L. Fowler, eds.) Vol. I (1960) 133.

[6] M. Coppola and H.N. Knitter, Kern. Isotop. Chemie, 10
     (1967) 459.

[7] R.A. Nobles, Phys. Rev. 126 (1962) 1508.

[8] D.M. Nadkarni and S.S. Kapoor, Proc. Nucl. Phys. Solid
     State Physics Symp. (India) 13B (1970) 73.

[9] E.R. Rae, B. Margolis and E.S. Troubetskoy, Phys. Rev.
     112 (1958) 492.

[10] J.G. Cuninghame, G.P. Kitt and E.R. Rae, Nucl. Phys.
     27 (1961) 154.

[11] J.W. Boldeman, W.K. Bertram and E.L. Walsh, Nucl.
     Phys. A265 (1976) 337.

CHAPTER V

SUMMARY

Present measurements were aimed to study the emission of different light-charged-particles from keV neutron induced fission of ^{235}U. Employing a semiconductor ΔE-E detector telescope, the yields and energy distribution parameters (the most probable energies and widths) of protons, tritons and alpha particles emitted from neutron induced fission of ^{235}U in coincidence with fission fragment were determined at neutron energies; thermal, 120 keV, 180 keV, 230 keV and 550 keV in the first part of the work. The second part of the present work was to study the finer details of the observed variation of the LRA yield with the incident neutron energy around E_n = 200 keV. A rear-etching technique was developed using a cellulose nitrate track detector and used for these measurements.

The triton yield relative to alpha particle yield for thermal neutron induced fission is observed to be about 6.8 percent which agrees well with the previous reported values while the proton yield relative to alpha particle yield is found to be about 9.3 percent in the present measurements which is significantly larger than the earlier reported values of about 2 percent. This difference in the relative yield of protons is understood to arise due to the experimental geometry used for detection of the fission fragments and the light-charged-particles. The fission fragments, emitted at angles close to 90° with respect to the mean direction of the light-charged-particle detection in the $\triangle E$-E detectors, have a lower efficiency of detection in the ionization chamber due to the fact that at these large angles the fragments get stopped in the thick source foil used in the present experiment.

The calculations on the detection efficiency of the fission fragments in the ionization chamber indicated that the efficiency for the equatorial emission of the light-charged-particles is only 20 %. This reduction of the events corresponding to the equatorial emission of light-charged-particles results in a relatively greater weightage to the polar particles. Since the polar alpha particles constitute a very small fraction ($\lesssim 2\%$) of the equatorial alpha particles, the greater weightage of polar events does

not cause any appreciable change in the observed energy spectra of alpha particles. Since the ratio of the proton yield to alpha particle yield in polar emission is about 20 times more than that for equatorial emission, the observed proton yield is significantly enhanced. The earlier measurements on proton yield correspond to only equatorial emission, whereas the present measurement includes both type of events. Since the triton to alpha particle yield ratio is same in both type of events, the polar tritons form a very small fraction ($\lesssim 2\%$) of the equatorial tritons and therefore, the observed energy spectra of tritons do not change appreciably due to the greater weightage of polar events.

The LRA yield increases with the incident neutron energy above 120 keV. At neutron energies lying between 150 keV and 250 keV, the yield becomes about 50 % higher as compared to that of thermal neutrons. At higher neutron energies (above E_n = 250 keV), the LRA yield decreases slowly with the incident neutron energy and at neutron energies of 500 keV and above the yield becomes the same as that of thermal neutron fission.

The large increase in the LRA yield at neutron energies in the region from 120 keV to 350 keV can be understood in terms of the increase in the p-wave contribution in fission cross section which is about 60 % of the total fission cross section in this energy interval. The

states accessible to the fissioning nucleus in the s-wave neutron fission of ^{235}U are negative parity states namely the 3^- and 4^- states while the states accessible to the fissioning nucleus in the p-wave neutron fission are the positive parity states namely 2^+, 3^+, 4^+ and 5^+. Since the positive parity states at the saddle point lie lower than the negative parity states, the extra energy thus made available may go to enhance the LRA emission probability in the p-wave neutron fission. At neutron energies of 500 keV and above, the higher order partial waves also make significant contribution to the fission process and thus one expects to get effects which are average of both parity states and thus the LRA yield becomes equal to that of thermal neutrons.

The triton yield increases gradually with the incident neutron energy such that the yield at E_n = 550 keV becomes about 3.5 times that of thermal neutron induced fission. The proton yield also increases with incident neutron energy but this increase is quite fast as compared to that of triton yield. At 550 keV neutron energy, the proton yield becomes about ten times that of the thermal neutrons. The variations in the yields of tritons and protons with incident neutron energy are altogether different in nature as compared to that of alpha particles. Since the present results have a mixture of the polar and

equatorial type of events, the increase in the yields of tritons and protons may be due to the increase in either the polar or the equatorial or both type of events. Further experiments are necessary to study the effect of the incident neutron energy on the yields of different light-charged-particles in polar and equatorial type of events separately.

The most probable energies and the standard deviations (widths) of protons, tritons and alpha particles do not show any significant dependence on the incident neutron energy. This indicates that the excitation energy dependence of the energy spectra of different light-charged-particles such as protons, tritons and alpha particles is very weak. This implies that the stretching of the fissioning nucleus at the scission point is not sensitive to the excitation energy and to the state of the transition nucleus at the saddle point.